



SAPIENZA
UNIVERSITÀ DI ROMA

Development of intra-operative β^- probe for cancer surgery

Scuola di Dottorato in Scienze Astronomiche,
Chimiche, Fisiche e Matematiche "Vito Volterra"

Dottorato di Ricerca in Fisica – XXVII Ciclo

Candidate

Francesco Collamati

ID number 1179818

Thesis Advisor

Prof. Riccardo Faccini

Co-Advisor

Dr. Elena Solfaroli Camillocci

A thesis submitted in partial fulfillment of the requirements
for the degree of Doctor of Philosophy in Physics

October 7th, 2014

Thesis not yet defended

Francesco Collamati. *Development of intra-operative β^- probe for cancer surgery.*

Ph.D. thesis. Sapienza – University of Rome

© 2014

EMAIL: francesco.collamati@roma1.infn.it

*Dedicato a mio Nonno
che ha sempre creduto
in me
nella "Fisica Italiana"
e nella chirurgia radioguidata*

Contents

Introduction	1
1 Radioguided Surgery	3
1.1 The importance of full tumor resection	3
1.1.1 Non nuclear tools	4
1.1.2 R.G.S. with Gamma	7
1.2 Limits of existing techniques	11
1.3 Possible developments	12
1.3.1 β^+	12
1.3.2 β^-	13
2 The FLUKA Monte Carlo code	19
2.1 Physics in FLUKA	20
2.1.1 Electrons and Positrons	21
2.1.2 Photons	21
2.1.3 Cut-Off Energy	22
2.2 Geometry in FLUKA	22
2.2.1 Voxel Geomertry - CT import	23
2.3 Input file structure in FLUKA	24
2.4 Output in FLUKA	24
3 Design and tests of the probe	27
3.1 Detector choice and characterization	27
3.1.1 Light Attenuation Length	29
3.1.2 α -Quenching factor	31
3.1.3 Photon sensitivity	34
3.1.4 Simulation	36
3.2 First probe prototypes	37
3.2.1 Probe1 testing	38
3.2.2 Comparison between data and simulation	41
3.3 Probes optimization and development	42
3.3.1 Spectrophotomery	43
3.3.2 Active area optimization	44
3.3.3 Shielding optimization	46

4	Medical Applications	49
4.1	Brain Surgery	49
4.1.1	Human brain structure and cerebral tumors	49
4.1.2	Radio Guided Surgery applicability on Cerebral Tumors	58
4.2	Neuroendocrine Tumors surgery	68
4.2.1	Neuroendocrine Tumors: origin and therapy	68
4.2.2	Feasibility study of β^- -RGS in Neuroendocrine Tumors	69
5	Evaluation of Probe Performances	81
5.1	Developments in FLUKA	81
5.1.1	PET import	81
5.1.2	Scoring routines	85
5.2	Expected signal rates in Brain Surgery applications	86
5.2.1	Simulation of the setup	86
5.2.2	Results	88
	Conclusioni	93
	Ringraziamenti	95
	Bibliography	99

Introduction

Since the inception of the modern era, with the lengthening of life expectancy, cancer has represented one of the most common causes of death worldwide, but also a most striking challenge to modern medicine.

Throughout the centuries, together with the deepening of our understanding in biology and human anatomy, numerous steps have been made in the comprehension of this complex and vast pathology. As a result, more and more effective diagnostic methods and treatment techniques have been developed.

Particularly in the last decades, new discoveries in chemistry and nuclear physics brought to groundbreaking advances in this field.

The detection in the blood of so called “tumoral markers”, or today’s imaging techniques (CT, NMR, SPECT, PET) paved the way to early and precise diagnosis of tumors, while chemotherapy and radiotherapy provided treatment options of fundamental importance.

Despite all this progresses, still today this battle is far from being won.

Hence, being surgery the principal treatment used for cancer, several techniques and technologies are being developed in order to improve its effectiveness, mainly by enhancing the completeness of the tumor resection.

In particular, in this Thesis, Radio Guided Surgery (RGS) is discussed. In this approach, a certain amount of a radiopharmaceutical, which is preferentially absorbed by the tumor, is administered to the patient before the surgical intervention. By means of a dedicated detector, capable of revealing the particles emitted by the radiopharmaceutical, the surgeon can scan the tumor site looking for residuals of the lesion after the removal of the bulk neoplastic mass.

Despite being this technique today fairly widespread, its applicability is restricted by a number of serious limitations.

In order to overcome such limitations, in this Thesis a novel approach is proposed, exploiting β^- radiation in place of β^+ and *gamma*, the ones used today.

In Chapter 1 an overview of the existing techniques of support to surgery is given, highlighting each one's strengths and weaknesses. Possible further developments are then discussed, focusing on β^- -RGS.

In Chapter 2, the FLUKA Monte Carlo code is presented, which was used throughout the whole Thesis to integrate and understand experimental measurements and clinical data.

In Chapter 3 the development of the probe to be used for β^- -RGS is discussed, starting with laboratory measurements and ending with the presentation and testing of the first probe prototypes.

In Chapter 4 the possible medical applications for such a technique are discussed, in particular regarding brain surgery and Neuroendocrine Tumors, presenting the results of two statistical studies carried out on DICOM images of patient affected by these diseases.

In Chapter 5, further studies exploiting both data and simulations are presented in order to evaluate the performance of the probe prototypes in real clinical scenarios, and an evaluation of the radio exposition of the medical personnel during a RGS procedure is obtained by means of a Monte Carlo simulation.

Chapter 1

Radioguided Surgery

Notwithstanding the number of other techniques and instruments that have been developed in the last decades in the field of cancer treatment, from radiotherapy to chemotherapy, surgery remains to date the most frequent option undertaken in case of tumor.

1.1 The importance of full tumor resection

Excluding all the cases in which a surgical intervention is not feasible (i.e. for tumor dissemination in various organs), the first goal of a cancer treatment is plainly the complete and precise resection of the lesion. In fact, there is a strict correlation between patient survival and disease free time (D.F.T.) and the resection completeness. However, this mere concept becomes much less simple when applied to the real case of a surgical procedure.

Centuries of discoveries in nuclear physics have provided highly advanced imaging techniques, allowing precise individuation of lesions from outside the patient before the intervention. For example, a lung tumor is usually clearly showed by a CT scan, while NMR provides sharp images of brain or liver cancers. Positron Emission Tomography is able to give functional imaging as well, giving informations about metabolism of both healthy and diseased tissue. These techniques are usually able to provide a spatial resolution of the order of few millimeters (in case of CT and NMR, several mm in case of PET), as evident from Fig. 1.1.

However, this remarkable amount of information available before surgery in some way cease to be much useful during the operation itself. In fact, an area that showed in the PET a particularly high metabolic activity, thus suggesting the presence of a lesion or for example a diseased lymph node, may be too poorly identified by the imaging to make it easy to the surgeon to find during surgery. Similarly, a brain lesion clearly delineated by NMR can be difficult to localize after craniotomy, and its borders difficult to discriminate due to possible little visual difference between normal and tumoral tissue.

The translation of pre-operative imaging informations in the surgical field is a critical point to optimize both the use of these valuable data and the effectiveness of the intervention. Hence, such a crucial topic has been addressed with several

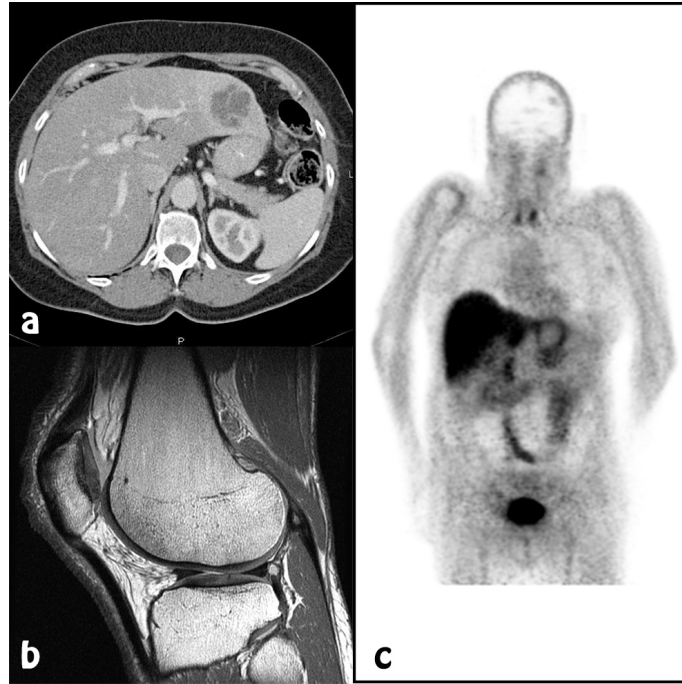


Figure 1.1. Examples of CT (a), NMR (b) and PET (c) scan images.

instruments and techniques.

1.1.1 Non nuclear tools

One of the fields in which the extent of the tumor resection is somehow even more important is neurosurgery. In fact, when dealing with brain cancer, it becomes fundamental to achieve as complete as possible a resection of the lesion, in order to minimize the risk of recurrences and secondary tumors, which originate from residual damaged cells. On the other hand, it is crucial for brain surgery to be conservative, aiming to spare healthy tissue in such a delicate organ [1, 2, 3].

For such reasons, several researches have been enterprised in the field of neurosurgery since the beginning of the XX century, when *Stereotactic Surgery* was first proposed. In this technique, once the patient's head is fixed in a certain position by means of mechanical supports, a set of three coordinates (e.g. cartesian) is used to locate important structures within the skull. In such a way, the physician could move its instruments in this reference system with respect to the RX image.

This original idea has been then developed in the following decades, leveraging on progresses in both imaging and technology, and today brain surgery is commonly carried out via a *neuro navigation system*. Such an apparatus is composed by a set of position detectors creating a frame of reference in which the patient's head and the surgeon's tools are positioned. During the operation, the physician is able to see in real time on a devoted screen (Fig. 1.2) the position of his instruments with respect to pre operative imaging (e.g. NMR).

In order not to spoil the millimetric resolution of NMR, a precise alignment between pre operative image and patient position is required, and this is achieved



Figure 1.2. Neuro navigation system for brain surgery.

by means of several position detectors located on the patient's head to be used as calibration. However, the real limit to precision and reliability of this instrument comes from a pure medical phenomenon.

In fact, being the brain not a rigid tissue, after craniotomy a shift of the order of few centimeters of the whole mass is observed, due to changes in intracranial pressure [4]. Moreover, once the bulk tumoral zone is removed, the tissue tends to readjust in a different configuration. The uncertainties introduced are large enough to make the neuro navigator an instrument useful mainly for a first surgical approach (choice of the craniotomy location), but of limited usefulness for lesion individuation and borders identification.

To minimize the loss of information due to changes between the pre-operative imaging and the surgical procedure, *intraoperative Nuclear Magnetic Resonance* (iNMR) has been proposed. In this technique, a NMR is performed directly during the operation, giving the surgeon a real time image of the brain. However, this requires dedicated (and expensive) operating rooms (Fig. 1.3), entirely free of magnetic materials and NMR equipped, and longer anesthesia due to the different duration of the intervention (a NMR is a quite long procedure, requiring normally about 20 – 30 minutes). Despite proved efficacy in enhancing the resection completeness ([5]), for these reasons this is not a real viable way.

Another way to help the surgeon to identify tumoral tissue during the intervention, disregarding pre operative images, is to inject the patient with a sort of "*cancer-cell probe*", that is a molecule that somehow bounds to the neoplastic ones, and the detection of which is possible by some means.

A first example of this approach is *Fluorescence-Guided Surgery* (F.G.S.). In this technique, a vector molecule is needed. For example, it has been demonstrated



Figure 1.3. An operating room equipped with iNMR.

([6]) that most ovarian cancer cells express lots of receptors for a molecule called *folate* (better known as vitamin B9 or folic acid). Cancer cells need this to grow and divide. It is then possible to attach to this molecule a fluorescent label (called *fluorescein iso-thiocyanate*): the detection of fluorescence light is then indicator of the presence of folate, and therefore of tumor cells (Fig. 1.4). In neurosurgery, the *5-ALA* technique, based on this same principle, has demonstrated to be effective in enhancing the completeness of the tumor resection [7].

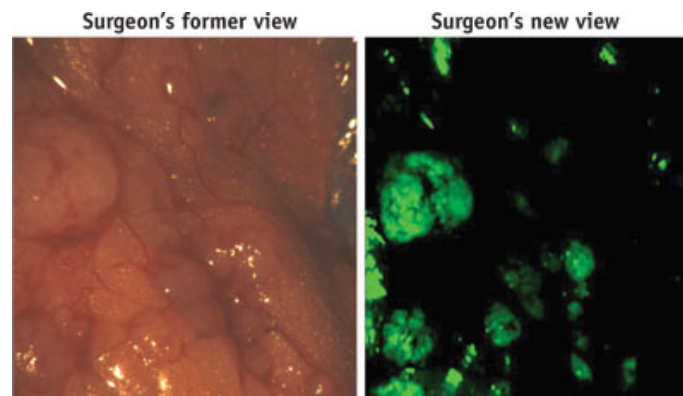


Figure 1.4. Example of Fluorescence Guided Surgery.

1.1.2 R.G.S. with Gamma

Another technique that shares somehow the same principle as F.G.S. is *Radio Guided Surgery* (R.G.S.) with Gamma emitters. Also in this case in fact the idea is to mark the tumor with a molecule. Here, though, the molecule is labelled with a radioactive isotope that undergoes gamma decay: the detection of the emitted photons is then clue of the presence of the molecule, and hence of the tumor. In Radio Guided Surgery there are several approaches regarding the way to carry the tracker compound to the tumor.

First steps in this techniques were moved in the field of *Sentinel Lymph Node Localization*. There are essentially two paths by which cancer cells can spread across the body: blood and lymphatic vessels. While blood stream is practically impossible to control, lymph provides in some way a preferential lane to check for the tumor diffusion. In fact, the slower circulation (about 1 – 10 cm/min) and the presence of lymph nodes makes it possible to check if the tumor is spreading in a certain direction. These small oval-shaped organs, sized 1 – 20 mm, are distributed widely throughout the body and act as filters or traps for foreign particles, playing a fundamental role in our immune system. In a certain sense they are midpoint of the lymphatic system, and thus good indicator of a possible neoplastic diffusion in the considered zone.

The hypothetical first lymph node or group of nodes draining a cancer is referred to as *sentinel* (Fig. 1.5), exactly upon the assumption that in case of dissemination this is the target organ primarily reached by metastasizing cancer cells from the tumor. It is thus fundamental to inspect this node for the staging of the cancer, subjecting it to biopsy and histologic analysis.

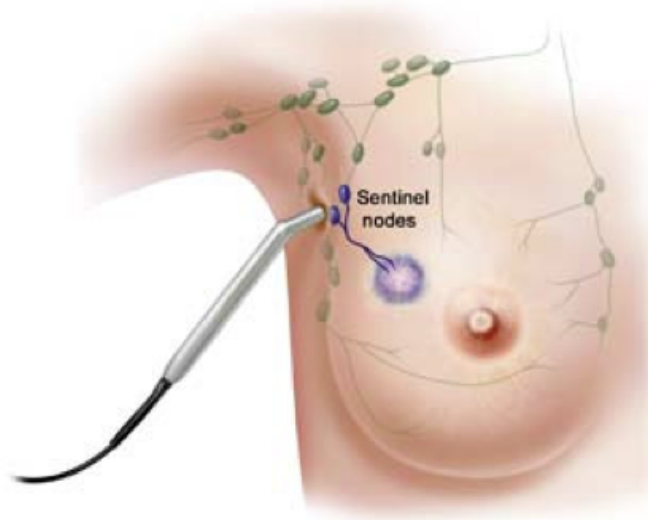


Figure 1.5. The concept of Sentinel Lymph Node.

However, it is often difficult given a certain tumor to identify its sentinel lymph node, being adjacent lymphatic vessels numerous and the path of the cells hard to forecast.

Thus, several attempts to provide the surgeon with manners to identify the

right node were made in the last decades, starting from the injection, few minutes before the operation, of a stained substance in proximity to the tumor. The color is then absorbed by lymphatic vessels, and hence by the node, that gains a blue hue. However, this technique presented a quite high percentage of failure, and was early abandoned in favor of different kind of labeling methods.

Today for sentinel lymph node localization (S.L.N.L.), there is consensus on using technetium-99-labeled colloids with well defined properties in terms of particle size. A *colloid* is a particle mixture halfway between solution and dispersion, in which microscopic (about 100 nm) particles are dispersed in a continuous phase. The trapping of the radio colloid in the nodes is due to the physiologic function of macrophages therein; the tracer is hence injected either interstitially, subcutaneously or intradermally, but always locally close to the tumor. The physician uses then a particle detector (named *gamma probe*) to search for activity *hot spots* in order to identify the sentinel lymph node.

Despite being the most common one, S.L.N.L. is just one of the today's applications of Radio Guided Surgery. In Table 1.1 different clinical cases in which RGS has been applied are reported.

Clinical application	Kind of RGS applied
Breast cancer	SNB, RIGS, ROLL, RIME, FDGDS
Skin cancer	SNB, FDGDS
Gastrointestinal neoplasm	SNB, RIGS, FDGDS
Head and neck neoplasm	SNB, RGS, RIGS, FDGDS
Gynecological neoplasm	SNB, RIGS, FDGDS
Urological neoplasm	SNB, RIGS, FDGDS
Chest neoplasm	SNB, RGS, RIGS, FDGDS
Neuroendocrine tumors	RGS
Adrenocortical carcinoma	FDGDS
Sarcoma	SNB
Brain tumor	RGS
Bone neoplasm	RGS
Linfoma	RGS

Table 1.1. Clinical applications of Radio Guided Surgery with γ probe: RGS, radioguided surgery; RIGS, radioimmunoguided surgery; SNB, sentinel node biopsy; ROLL, radioguided occult lesion localization; RIME, radioguided intraoperative margins evaluation; FDGDS, ^{18}F -FDG directed surgery.

Nonsentinel lymph node applications of RGS can be roughly divided in 2 main categories, according to the kind of radiopharmaceutical. Some are based on radiopharmaceuticals that do not have any tumor-seeking property, but are nonspecific particulate agents that do not appreciably move from the site of injection, that is local with respect to the tumor. It is a mechanism similar to that of S.L.N.L., but with the size of the molecules changing on the basis of the needed retention time of the colloid within the cancer. On the other hand, there exist radiopharmaceuticals that accumulate preferentially at tumor sites, and are thus administrated systemically.

A first and probably most common example of this kind of radiopharmaceutical is FDG (*fluorodeoxyglucose*), which is nothing but a glucose molecule in which a Fluor atom can be easily substituted with a radioactive one. Cancer cells are constantly reproducing, thus needing lot of energy, delivered in the form of glucose molecules. A certain amount of FDG administered intravenously to the patient will therefore be preferentially absorbed by tumoral cells, making this molecule an efficient carrier towards the cancer. This simple "metabolic" way of reaching target cells, which is at the base of common PET exams, however, is not the only possibility.

Some tumors in fact express receptors for particular molecules. Somatostatin, for example, is an hormone that regulates the endocrine system, and it is possible to artificially produce so called *analogues* molecules: synthetic compounds that share with the original one several properties, included the ability to bind. These analogues are hence used as radiopharmaceutical for those tumors that express this kind of receptor, as will be detailed in sec. 1.3.2.1.

When referring to a radiopharmaceutical, one should consider it as a two part system: the *carrier* molecule (discussed above) and the *radioactive nuclide*, which is responsible of the particle emitted and thus to detect. Today, radiopharmaceuticals labeled with technetium-99 are used in more than 85% of studies in a general nuclear medicine department [8]. The popularity of this radionuclide is due mainly to its emission, that consists of a pure photon without β contamination. As will be pointed out in sec 3.1.3, photons are penetrating particles, which interact weakly with the traversed tissue, thus transferring low quantities of energy. On the other hand, β particles, being electrically charged, interact much more within the tissue, with consequent higher dose released and lower penetration range. Another favorable characteristic of ^{99m}Tc is its half life of the order of 6 h, that reduces the environmental contamination after the procedure.

Table 1.2 shows different radiopharmaceuticals commonly used in clinical practice, indicating both the carrier molecule and the radioactive nuclide: as evicted from the table, their principal use today are two: diagnostic and therapeutic.

Radionuclide	Emitted particles	$T_{1/2}$	Radipharmaceuticals	Use
^{99m}Tc	γ	6.01 h	^{99m}Tc -MDP ^{99m}Tc -MIBI	Diagnostic
^{18}F	β^+	110 min	^{18}F -FDG	Diagnostic
^{111}In	γ	67.4 h	^{111}In -Octreotide	Diagnostic
^{86}Y	β^+	14.7 h	^{86}Y -DOTATOC	Diagnostic
^{68}Ga	β^+	68 min	^{68}Ga -DOTATOC	Diagnostic
^{90}Y	β^-	64.1 h	^{90}Y -DOTATOC	Therapy
^{177}Lu	β^- , γ	6.73 d	^{177}Lu -DOTATATE	Therapy
^{131}I	β^- , γ	8.1 d	^{131}I -MIBG	Therapy

Table 1.2. Most common radionuclides and radiopharmaceuticals used for diagnostic and therapeutic purposes.

In the former case, in addition to SLNL, they are used for example for imaging techniques, like the aforementioned PET, or SPECT, in which the patient is systemically injected with a small dose (about 200 MBq) and then placed within a specific

detector able to reconstruct from the revealed particles tomographic images of the tracker distribution, gaining important informations for example about metabolic activity inside the body. In the latter case, as explained in sec. 1.3.2.1, a higher dose of radiopharmaceutical is administered intravenously to the patient, with the goal to reach cancer cells and to damage them via radioactive short range decay. In this case, the dose (about 2 GBq) is determined from a tradeoff between the desired damage to diseased cells and toxicity to healthy ones, especially the red marrow.

In radioguided surgery all these radiopharmaceuticals are possible candidates to use, and the choice relies upon the organ to be considered and the clinical need of such a technique.

A case in which RGS brought a relevant improvement in clinical practice is breast cancer surgery. It is proved that the early detection of breast malignancies decreases mortality and morbidity of breast cancer patients [9]. These early-detected tumors are generally small and non-palpable, and it is thus often difficult for the surgeon to find them intraoperatively even if the mass was clearly delineated by the ultrasound.

In this context the ROLL (*Radio-guided Occult Lesion Localization*) technique has been proposed [10]. In this method, the physician injects inside the tumor, under ultrasound or stereotactic guidance, a small dose of a compound similar to the one used for SNLN, labelled with ^{99}Tc . In such a way he can use a gamma probe during the intervention to locate and excise the non palpable lesion. This technique, first proposed in 1999, is nowadays wide common in hospitals, and has been proven to improve patients outcome, cost effectiveness (due to secondary operations avoided), patient comfort and cosmetic result [9], especially considering the very low cost in terms of absorbed dose to the patient (about 0.5 mGy [8]) and the personnel. Its translation to other kind of tumors is currently under investigation, with promising results [11].

Despite being SNLN and ROLL the most common and of greater impact utilizations of RGS, several other applications have been investigated in the last decades, as shown in Tab. 1.1. Apart from SNB and ROLL, all the other entries therein rely on the use of systemically injected radiopharmaceuticals with high affinity with the tumor. Is this a quite widespread technique for example for Neuroendocrine tumors [12] and parathyroid adenomas [13].

All the RGS applications seen so far rely on a specific probe able to detect photons of energy of about 100 – 1000 keV. The rapid diffusion experienced by RGS in the last decades resulted in a proliferation of commercially available instruments for this purpose (Fig. 1.6).

These probes are usually composed by an active area (scintillator or semiconductor detector), surrounded by few millimeters of shielding material, in order to retain directionality. The instrument is then connected either via cable or wireless to an electronic apparatus for signal elaboration, that gives informations to the surgeon usually by means of a small display and/or a color/sound code to evaluate the activity measured. A review of available probes can be found in [14].



Figure 1.6. A commercially available gamma probe for RGS

1.2 Limits of existing techniques

Despite having favored remarkable improvements in the effectiveness of surgical interventions, all the techniques examined so far present several serious limitations.

In sec. 1.1.1 we saw why neuro navigator systems and iNMR, although being valuable tools, are not a complete response to the surgeon needs.

Regarding FGS, the first limitation is represented by the small number of vector molecules available, that cause the field of applicability of this technique to be quite narrow, being the affinity with tumor cells dependent also on their histotype. This means that each tumor needs its molecule, even if differentiating one another only for their histological characteristics. Secondly, being the fluorescence light emitted usually in the near infrared region of the electromagnetic spectrum, these procedures are quite unhandy to do, due to the necessity to use a system of filters and microscopes and to constantly shift between normal light mode and fluorescence mode (which often requires to switch off environment lights).

Coming to RGS, while ROLL and SNLN procedures have found their reason for being in the equilibrium between pros and cons, all the other techniques relying on systemic injection of gamma emitting radiopharmaceuticals encounter profound drawbacks limiting their effectiveness and applicability.

First of all, to detect photons, that are quite weakly interacting particles, thick detectors are needed. Moreover, the importance of signal directionality and background protection calls for a shielding that rises the transverse section of the probe up to centimeters, making it not so handy to use in a narrow and complex operating field.

Secondly, a systemic administration of the radio tracker results in a relatively high radioactivity concentration in normal tissue surrounding the tumor, depending on the affinity of the used molecule. Moreover, the period of radioactivity retention in the tumor of the radiopharmaceuticals is highly variable, with the consequence of

affecting the Target to Background Ratio at different times post injection, calling for a case-by-case choice of the optimal administration time in order to maximize it [8].

Lastly, a non trivial radiation dosimetry must be taken into account, due to the administered dose (in the order of a full diagnostic one) and to the highly penetrating nature of photons, thus implying not negligible exposition for the medical personnel.

1.3 Possible developments

Considering RGS, it is quite evident that the majority of its aforementioned drawbacks are due to the use of photons as decay particles. This is why it is possible to consider further developments of this same idea, by changing the emitting isotope.

1.3.1 β^+

The first possibility is to use as radioactive atom one of those decaying via the emission of positrons (β^+ particles). The possible advantages of such a method are manifold.

First, several β^+ emitting isotopes are already commonly used in nuclear medicine. The most common one is the aforesaid ^{18}F , which is everyday used in ^{18}F -FDG PET exams. Other examples of positron emitting radionuclides are ^{11}C , ^{68}Ga and ^{86}Y . This is an important point, because it represents a well established know-how from which to start, even from a regulatory and legislative point of view (new drugs must pass through a long lasting protocol of testing and validation prior to be usable).

The second main advantage of this approach is related to the interactions of positrons in matter. In fact, being charged particles, positrons interact much more than photons. As a consequence, their range is reduced to few millimeters for positrons of about 1 MeV, after which, due to their nature of antiparticles, they annihilate encountering electrons in the traversed tissue, producing a couple of back-to-back photons of 511 keV in energy. The low penetration range results in the double advantage of a limited path within the body, assuring better spatial resolution than photons, and the need for thinner sensitive detectors, allowing theoretically smaller probes.

On the basis of these arguments, in 1994 a β^+ probe was first proposed by Daghighian et al. [15]. This prototype was composed by two separate detectors: one plastic scintillator for positron detection and a gamma counter. The β^+ yield was hence obtained by subtracting the activity measured by the latter one to the one measured by the former, in order to neglect the fraction of photons detected by the positron detector.

This two-fold approach is quite common among β^+ probes, being the photon contamination an important factor to account for. In some cases this developed in a sort of double-mode probe, in which the two separate detectors could also be operated independently, resulting in both a positron (by means of the aforesaid mechanism of photon signal subtraction) and gamma probe at the same time.

A more advanced kind of β^+ probe was proposed in 2005 by Yamamoto et al. [16], using as radio tracker ^{18}F -FDG. This prototype uses a phoswich detector composed of a plastic scintillator and a bismuth germinate (BGO). A positron is detected by the plastic scintillator and emits annihilation photons. The BGO nearby detects one of the annihilation photons while a photo-multiplier tube detects scintillation

photons from both scintillators. The decay time differences of these two scintillators are used to distinguish whether the event is a true event where a positron and a following annihilation photon are detected simultaneously, or a background event due to annihilation photons produced elsewhere in the body.

Only in 2007 a first application of β^+ -RGS to cerebral surgery was proposed. Bonzom et al. proposed a positron probe designed to be integrated in the instruments commonly used by neurosurgeons during the intervention. [17] The probe consisted in a series of optic fibers to detect β particles, each of which has a counterpart of a similar fiber that is though slightly shielded in order to stop positrons and act as detector of the photon contamination to be subtracted (Fig. 1.7).

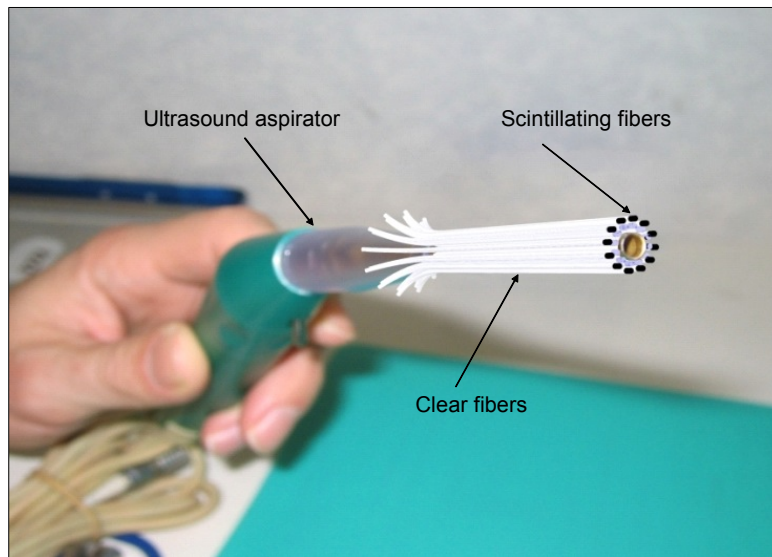


Figure 1.7. Representation of the prototype of β^+ probe proposed by Bonzom et al., here applied over the ultrasonic aspirator commonly used by neurosurgeons.

This probe was hereafter subjected to further studies [18], demonstrating on phantoms of 5 mm of diameter and 20 mg mass soaked in ^{18}F a TBR > 3.1 with an acquisition time of 4 s, which despite being a promising result is far from being a satisfactory value for brain surgery.

Summarizing, the use of β^+ emitters addresses some of the main limitations of γ -RGS, such as the long penetration of gamma radiation and the consequent loss of spatial resolution. However, several drawbacks are still present in this method, mainly due to pure physical reasons, like the annihilation photon background, that make them impossible to eliminate.

1.3.2 β^-

A third approach in Radio Guided Surgery, aiming at overcoming all the limits discussed so far, would straightforwardly be represented by the use of β^- radiation.

However, the history and development of this method has evolved through a particularly peculiar and non linear path. Despite being in fact the only approach

to be practically unused today, it was actually the first one to be conceived at the very beginning of Radio Guided Surgery.

In 1949 Selverstone proposed to use ^{32}P as a radio tracker [19], which is a pure β^- emitter ($Q_{val} = 1711$ keV, $t_{\frac{1}{2}} = 14$ d), for patients with glioma undergoing surgery. At the time there was no concept of radiopharmaceutical, and the targeting of the tumor relied on several miscellaneous discoveries achieved in that decades. It was well established that the phosphate ion (HPO_4) is the major intracellular anion of the body, thus suggesting a more rapid turnover of the substance in the inorganic fraction of a rapidly metabolizing tumor than in the relatively static normal brain tissue. At the same time, it was noted that normal brain shows a low turnover of ^{32}P compared with other organs. Moreover, in 1942 it was demonstrated that blood-brain barrier has greater effect in the case of negatively charged particles: if a local defect on the barrier exists in the tumor, this could imply an enhanced differential uptake between glioma and normal brain.

Given these considerations, Selverstone injected 33 patients at least 24 h before surgery with radioactive phosphate ion. The physician could than explore the surgical field looking for activity hotspots via a particular detector, that was actually a Geiger-Muller tube, sized $\sim 3 - 5$ cm in diameter, filled with an argon-ether mixture (Fig. 1.8).

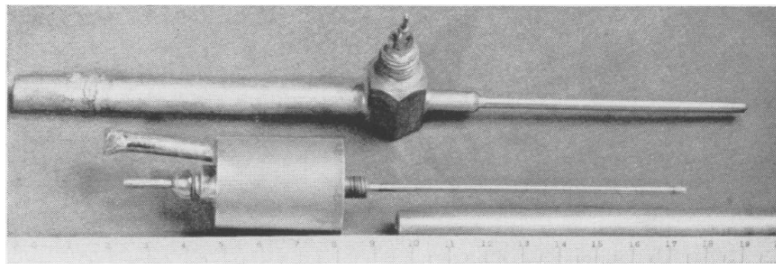


Figure 1.8. First prototype of Radio Guided Surgery *probe* proposed by Selverstone in 1949.

In this trial, the probe was able to localize 23 cerebral tumors out of 33 patients, facilitating in 12 of them the total resection of the lesion. In 4 cases the tumor was not localized due to false negatives ascribed to the impossibility to position correctly the probe over infiltrated gliomas.

When considering the importance of this very first approach to RGS, there are some aspects that have to be considered. First and foremost, this was the early endeavor in a new and unexplored field, the one of nuclear aid and support to surgery, in an era that was in numerous aspects remarkably far from ours.

Medical knowledge about interactions of radioactive isotopes injected in the body was for example still scarce: there was no mature consciousness about late effects of absorbed doses, and radiation protection was at its initial stages. In this context, the choice of ^{32}P is in retrospect arguable: injecting a patient with an isotope that decays with a $t_{\frac{1}{2}} = 14$ d means that the person is going to be “radio-active” for several weeks later. Also, the absence of proper radiopharmaceuticals made this technique’s field of application noticeably confined to selected single cases.

As far as the detector is concerned, the possibilities were considerably narrowed by lack of knowledge in both nuclear physics and engineering. The use of a Geiger-Muller counter, despite being the only practicable way at that moment, led to various shortcomings. Shape and dimensions of sensitive area, and thus of the whole probe, are in fact constrained by the need of a gas filled zone and electric apparatuses. Moreover, due to their functioning mechanism (gas ionization and recombination) Geiger-Muller counters are characterized by high dead-time. Lastly, operating with gases is often considered dangerous, especially in a delicate environment such as an operating room, due to the risk of explosion.

In spite of all these arguments, the one from Selverstone represents a seminal work in Radio Guided Surgery, worthy of having focused a problem, suggested a method and put the bases for the development of such an important technique so widespread today.

Now, is a matter of fact that in the last half century both Medicine and Nuclear Physics experienced a period of copious and substantial discoveries, giving the opportunity to overcome all the drawbacks in β^- -RGS outlined so far.

In this Thesis work I investigated how a novel Radio Guided Surgery technique with the use of β^- emitters is today feasible and convenient with respect to the already existing techniques.

1.3.2.1 Ligand molecule choice

As pointed out in sec. 1.1.2, a crucial role in Radio Guided Surgery is played by the radiopharmaceutical, which is composed by two separate parts: the ligand molecule and the radio isotope, being probably the former the most important one.

It is in fact on the *carrier* that depends primarily the efficacy of this technique, and it is thus fundamental to choose a molecule with high affinity for tumor cells.

Actually, this field has already been widely explored in the context of *Molecular Radio Therapy* (MRT). While conventional Radio Therapy aims at destroying malignant cells bombarding them with projectile particles (e.g. X-rays), in MRT vector molecules are used to carry the emitting isotopes within the tumor, striking them from inside.

For example, in *Peptide Receptor Radionuclide Therapy* (PRRT), somatostatin analogues are radio-labelled to reach tumors expressing receptors for this hormone. This technique, first proposed at the end of the nineties, has demonstrated to be effective in case of unresectable or metastatic tumors, and is today used for both curative and palliative treatments [20].

A certain number of these compounds have hence been synthesized (DOTATOC, DOTATATE), sharing similar characteristic and behavior, and several couplings with different radio isotopes are today used. This number of radiopharmaceuticals commonly available and already tested for several kind of tumors offer a wide set of molecules to consider for Radio Guided Surgery applications.

1.3.2.2 Ideal isotope characteristics

As far as the radioactive atom is concerned, the principal characteristics to consider are commonly 3: the half life, the kind of decay and the energy of the emitted particle.

First, an ideal candidate for β^- -RGS should undergo pure β^- decay. A γ contamination would in fact increase the dose transferred to the tissue without any gain in the signal, that would instead be spoiled by interfering (and highly penetrating) particles, coming even from healthy organs across the body.

Secondly, the emitted electron should have an kinetic energy of about 1 MeV. In fact, this value corresponds to a range of about 5 mm (Fig. 1.9); a lower energy particle would not be able to reach the detector being stopped by the traversed media (healthy tissue, biological liquids, probe covering), while a higher energy one would travel through few centimeters of matter, leading to a higher contribution from zones adjoining to that of interest.

Lastly, regarding the isotope half life, two aspects should be considered. On one hand, the half life should be long enough for the radiopharmaceutical to be comfortably managed, from its production to its administration. On the other hand, $t_{1/2}$ should be short enough not to constitute a hazard regarding patient, personnel and environmental radiation protection after the treatment. To sum up, an half life of the order of 2 d could meet both of these requirements.

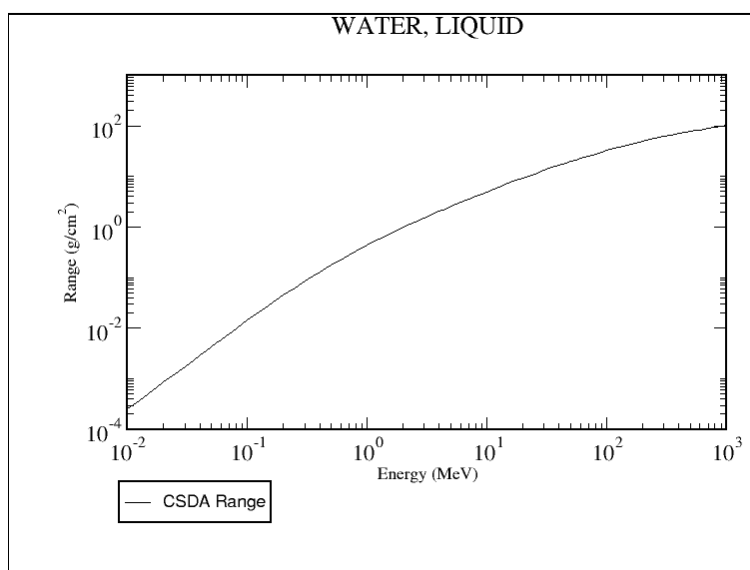


Figure 1.9. Range in water for electrons.

One of the most used compounds in PRRT is ^{90}Y -DOTATOC (*DOTA-D-Phe1-Tyr3-octreotide*). This is a somatostatin analogue, and receptors for this hormone have been identified in different kinds of tumors, such as neuroendocrine tumors, tumors of the central nervous system, breast, lung and lymphatic tissue [21].

^{90}Y is a pure β^- emitting isotope, which decays in ^{90}Zr with an half life of 64 h. The produced electron has in more than 99.989% of times a maximum kinetic energy

of 2.280 MeV. The complete decay scheme is showed in Fig. 1.10.

The actual absence of gamma emission is considered as a drawback in PRRT, being it a valuable tool for dosimetry and uptake validation during the treatment by means of SPECT imaging, that in case of pure β^- decay is relegated to BrehmsStrahlung radiation, which is far more scarce.

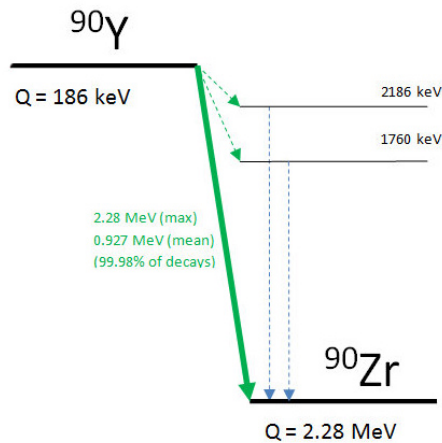


Figure 1.10. ^{90}Y decay scheme.

For these reasons (proved uptake, decay type half life and energy) ^{90}Y -DOTATOC represent a good candidate as radiopharmaceutical for Radio Guided Surgery with β^- emission.

1.3.2.3 Ideal detector characteristics

The last player needed for RGS is the *probe*. In sec. 1.3.2 we discussed why gas detectors are not suitable for these applications (size, structure and safety). One possibility would be represented by Silicon Detectors, which could provide good detection efficiency of such electrons. However, for mechanical reasons they are not easy do adapt to particular sizes and geometries (e.g. rounded ones), and the needed electronics can be difficult to fit within a small device. A further possibility is represented by the use of scintillators, that can be shaped and sized in desired ways, require simple electronics, and which low cost is compatible with a disposable probe.

Chapter 2

The FLUKA Monte Carlo code

Monte Carlo (MC) calculations are a standard tool in several areas of research, and particularly in physics. This name is used to refer to any technique in which complex models are evaluated by generating successive random samples and interpreting statistically the global result after numerous iterations. This technique dates back to the 40s, having being developed in the framework of the Manhattan Project, and owes its name to the famous casino in Monaco [22].

Even if born in the frame of gamble, MC is now used in a variety of contexts, including for instance economics: it is fact today at the base of risk measurements computation, portfolios sensitivity evaluation and so on.

In particle physics, the main application of this method is to simulate particle transport and interactions in media. From the knowledge of the physics of the elementary collision processes (which accuracy strongly influences the one of the entire technique), MC simulations actually create and track a high number of primary particles, as well as the secondaries created in interactions.

A certain amount of information (depending of the desired depth of the study undertaken) is then stored and analyzed.

The main advantage of this approach is that it permits to study various different configurations (for example geometries or primary particles) before (or even without) doing specific measurements.

The other use of simulation is to support experimental data comprehension, by helping to recognize unexpected structures and phenomena.

In parallel, MC techniques find wide applications even in medicine, and in particular in nuclear medicine. Each radiotherapeutic treatment is in fact preceded by MC simulations aimed at verifying the exact localization of energy deposition within the body.

In this Thesis work I used MC simulations to study the response to different kinds of signal of various prototypes of probe, thus testing and optimizing its design, and to evaluate radio protection issues due to the injected activity.

FLUKA (*FLUktuierende KAskade*) is a general purpose tool for calculations of

particle transport and interactions with matter, developed within a collaboration between INFN (*Istituto Nazionale di Fisica Nucleare*) and CERN (*European Council for Nuclear Research*) [23].

Its original application was accelerator shielding, but its development in the past years led it to be a common tool for numerous applications, from ion beam and electron acceleration to calorimetry, activation and dosimetry studies, being able to simulate about 60 different particles with energies ranging from the keV up to thousands of TeV.

The history of FLUKA began in 1962, when Prof. Johannes Ranft at CERN wrote the first high-energy Monte Carlo transport code. Starting from those early pioneer attempts, it is possible to distinguish three different generations of FLUKA codes along the years, which can be roughly identified as the FLUKA of the 70s (main authors J. Ranft and J. Routti), the FLUKA of the 80s (P. Aarnio, A. Fassò, H.J. Moring, J. Ranft, G.R. Stevenson), and the FLUKA of today developed under the INFN CERN Collaboration Agreement (A. Fassò, A. Ferrari, J. Ranft and P.R. Sala).

Even if every new generation of the code originates from the previous one, each new version represented not only an improvement of the existing program, but rather a quantum jump in the code physics, design and goals. In this sense, the name FLUKA has been preserved as a reminder of this historical development, even if the present code has pretty much nothing to do with the versions which were released before 1990.

FLUKA is developed using the FORTRAN 77 language. A graphical user interface named *Flair* (FLUKA Advanced Interface) has been developed using Python [24]. For most applications, no programming is required from the user, even if a number of Fortran-77 routines are available in case of special requirements.

Efficiency is achieved by relying heavily on table look-up sampling and a systematic use of double precision has a great impact on overall accuracy. To obtain a reasonable flexibility while minimising the need for user-written code, the program has been provided with a large number of options available to the user, and has been completely restructured introducing dynamical dimensioning.

2.1 Physics in FLUKA

The strength of FLUKA is in its physical models: microscopic models are adopted whenever possible, consistency among all the reaction steps and/or reaction types is ensured, conservation laws are enforced at each step, and crosschecks between results and experimental data are done at single interaction level. As a result, final predictions are obtained with a minimal set of free parameters fixed for all energy, target and projectile combinations. Therefore results in complex cases, as well as properties and scaling laws, arise naturally from the underlying physical models, predictivity is provided where no experimental data are directly available, and correlations within interactions and among eventual shower components are preserved.

The transport of electrons and photons in FLUKA (EMF, for Electro Magnetic

FLUKA) handles all interactions and scattering processes, including photon nuclear interactions.

The electromagnetic sector is fully coupled to the hadronic one, for instance photons from nuclear deexcitation are directly transported by EMF, and photonuclear interactions are treated in the same framework as hadronic interactions.

For each kind of particle, a set of relative effects are taken into account regarding transport and interactions with matter.

2.1.1 Electrons and Positrons

Since the origins, the algorithm used by FLUKA for charged particles includes:

- A complete multiple-Coulomb scattering treatment giving the correct lateral displacement even near a boundary;
- the Landau-Pomeranchuk-Migdal suppression effect;
- ter-Mikaelyan polarisation effect in the soft part of the bremsstrahlung spectrum;
- positron annihilation in flight and at rest;
- electrohadron production via virtual photon spectrum and Vector Meson Dominance Model;
- the bremsstrahlung differential cross sections of Seltzer and Berger have been extended to include the finite value at tip energy, and the angular distribution of bremsstrahlung photons is sampled accurately;
- the variations with energy of the discrete event cross sections and of the continuous energy loss in each transport step are taken into account exactly;
- differences between electron and positron are taken into account concerning both Bremsstrahlung and Stopping-Power;
- delta-ray production via Bhabha and Moller scattering.

2.1.2 Photons

Photons interactions are taken into account as carefully as charged particles ones. In each interaction, FLUKA is able to describe:

- pair production with actual angular distribution of electrons and positrons;
- photoelectric effect with actual photoelectron angular distribution, detailed interaction on six K and L single sub-shells, optional emission of fluorescence photons and approximate treatment of Auger electrons;
- Rayleigh scattering;
- photon polarization taken into account for Compton, Rayleigh and Photoelectric effects;

- Compton scattering, considering both binding effects and orbital motion of all electronics shells of all elements (particularly important for low energy photons).

2.1.3 Cut-Off Energy

An important aspect in Monte Carlo simulations is the correct tuning of cut-off energies for both transported and produced particles. In FLUKA several sets of these parameters are available via optional card DEFAULTS (e.g. for hadrontherapy or dosimetry applications), which takes a default value even if not declared. However, it is often convenient to override some of the default cut-offs according to particular needs in term of performance of accuracy.

Transport cut-offs, or thresholds, are set with command PART-THRes for hadrons and muons, with EMFCUT for electrons, positrons and photons, and with LOW-BIAS for low-energy neutrons. Despite the similar functionality of the three commands, there are important differences in their syntax and in the way the threshold is implemented for the three families of particles.

PART-THRes can assign different transport thresholds to different particles, but the thresholds are the same in all materials and regions. When the hadron or muon energy becomes lower than the relevant threshold, the particle is not stopped but ranged out in a simplified way.

EMFCUT can assign instead transport thresholds on a region basis for electrons positrons and photons: on the other hand no ranging out is performed, due to the difficulty to clearly define electron ranges.

LOW-BIAS is used to sets the transport threshold for low-energy neutrons, also on a region basis, but as a group number rather than an energy.

Two input commands can set particle production cut-offs, respectively for heavy particles and for electrons, positrons and photons. Thresholds for delta ray production by charged hadrons and muons are assigned, on a material basis, by means of option DELTARAY. Energy transfers to electrons lower than the threshold are handled in the continuous slowing down approximation. Production of bremsstrahlung by electrons and of Moller/Bhabha secondary electrons is simulated explicitly above thresholds set on a material basis with option EMFCUT.

2.2 Geometry in FLUKA

FLUKA is able to manage very complex geometries via an improved version of the Combinatorial Geometry package. There are two fundamental concepts in CG: bodies and regions.

Originally, bodies were defined as convex solid bodies (finite portions of space completely delimited by surfaces). In FLUKA, the definition has been now extended to include infinite cylinders (circular and elliptical) and planes (half-spaces).

Regions are defined as combinations of bodies obtained by boolean operations: Union, Subtraction and Intersection. Each region is not necessarily simply connected (it can be made of two or more non contiguous parts), but must be of homogeneous material composition.

Being not possible for the ray tracing routines to track particles across the outermost boundary, all the regions must be contained within a surrounding *blackhole* (an infinitely absorbing material), so that all escaping particles are absorbed. It is suggested to make the external blackhole region rather big, in order not to interfere with possible further modifications of the problem layout.

Really important, and not so easy condition to respect, is that each point of space MUST belong to one and only one region.

This combinatorial approach paves the way to complex geometries and powerful capabilities, based on Voxel Geometry.

2.2.1 Voxel Geomertry - CT import

In FLUKA it is possible to describe a complex geometry in terms of *voxels*, that are tiny parallelepipeds forming a 3-dimensional grid.

In principle this can be done with any geometry, but it is especially useful when translating a CT scan of a human body into a phantom. In this context, the word "organ" is used to indicate a contiguous group of voxels (or even more than one group) made of the same material. The code handles each organ as a Combinatorial Geometry region, possibly in addition to other conventional "non-voxel" regions defined by the user, and assigns automatically to each organ a new region number.

To this aim, FLUKA is able to receive in input directly the *DICOM* files of the scan. The conversion between Hounsfield unit (HU, the unit used in CT to parametrize the stopping power of a certain tissue, i.e. the grade of gray in a image) and the material is performed by means of two text files. A first one is a table that assigns to each HU value a tissue density, while a second file assigns to each HU interval a material. This is a significantly nontrivial conversion, due to very large variations between patients and body zones. Different of these files are thus available, in relation to the imported ones (head, body, etc.).

The result of such importation process are showed in Fig. 2.1.

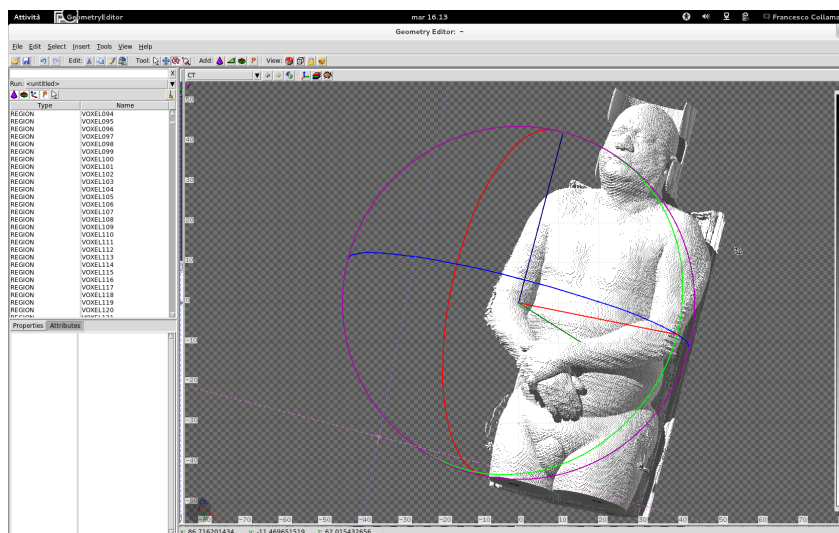


Figure 2.1. Result of the importation of CT dicom files in FLUKA. On the left several voxel volumes automatically created by FLUKA are listed.

2.3 Input file structure in FLUKA

The input file of a FLUKA simulation consist in an ASCII file with extension `.inp`. In this file a series of instructions (named *cards*) are written in each line, following this order:

- Title and comments;
- Description of the problem geometry;
- Definition of the materials;
- Material assignment;
- Definition of the particle source;
- Definition of requested detectors that the user wants to calculate various physical quantities such as dose, fluence, etc.;
- Definition of biasing schemes;
- Definition of problem settings such as energy cut-offs, step size, etc.;
- Initialization of the random number sequence;
- Starting signal and number of requested histories.

FLUKA provides a BEAM card by which it is possible to choose the particle kind, its energy or momentum (with the eventual spread), its starting position and direction. For more complex sources a devoted *user routine* must be used.

2.4 Output in FLUKA

Every FLUKA simulation automatically produces three text output files, named as the `.inp` file, with the extensions `.out`, `.log` and `.err`.

These last two files contain useful informations in case of errors during the simulation helping to solve them.

The FLUKA standard output file (`.out`) instead contains plenty of information about the executed run:

- A header with the FLUKA version and the time when the output was printed;
- A straight echo of the input cards and the geometry input, useful to quickly check if all the cards are correctly read and interpreted;
- Informations about basic nuclear data files and physical models used in the simulation process;
- Material parameters related to multiple scattering;
- Memory allocation information;

- Table of correspondence between materials used in the run and materials in the low-energy neutron cross section library;
- Information on the low-energy neutron cross section
- Material-dependent parameters: ionization energy losses, δ -rays and Bremsstrahlung threshold, transport thresholds;
- List of FLUKA particles
- Interpreted input summary
- Scoring summary: list of each estimators requested;
- Materials scattering length;
- Energy balance: percentage of the initial energy deposited and/or lost on each region of the simulation.

Beside the .out file, a number of scoring possibilities are available by means of SCORE cards. Via this cards FLUKA can score particle fluences, current, track length, energy spectra, Z spectra, energy deposition, dose deposition etc.

The possible detectors are:

- USRTRACK and USRCOLL: score average $d\phi/dE$ (differential fluence) of a given type or family of particles in a given region.
- USRBDX: score average $d^2\phi/dEd\Sigma$ (double-differential fluence or current) of a given type or family of particles on a given surface.
- USRBIN scores the spatial distribution of energy deposited, or total fluence (or star density, or momentum transfer) in a regular mesh (cylindrical or Cartesian) described by the user. Usually the results from USRBIN are normalised per unit volume and per unit primary weight.
- USRYIELD scores a double differential yield of particles escaping from a surface. The distribution can be with respect to energy and angle, or other specific quantities.

Chapter 3

Design and tests of the probe

Among the possible implementation of the β^- probe described in Sec 1.3.2.3, the use of scintillators is the one that best matches the showed requirements.

When considering scintillating detectors, there are commonly two different approaches to follow. In case high light yields are required, for example if searching for small signals, inorganic scintillators are used due to their elevated light production. However, when the circumstance requires larger size detectors and fast time response organic scintillator are preferred, due to their lower cost and short decay time of the scintillation light. Moreover, their low Z makes them usually poorly sensitive to photons.

The studied situation lies somehow in the middle of these two scenarios: aiming at producing an effective probe for β^- radioguided surgery, indeed, several requirements need to be fulfilled.

First, the detector must be able to entirely contain electrons of few MeV, being as much as possible transparent to photons, that, as pointed out in Sec. 1.3.2.2, constitute a background in this scenario. On the other hand, the probe must be highly sensitive to even small electron signals, in order to allow both low doses injected to the patient and fast enough response to be used as a live-scan tool during the surgical procedure. Moreover, the entire detecting system should result in a handy tool for the surgeon, thus putting strong constraints on the size of the entire apparatus.

In this Thesis, a possible solution to this interweave of requirements is studied.

3.1 Detector choice and characterization

Aiming at closing the gap between inorganic and organic scintillators, in this Thesis I studied the properties of *para-terphenyl*, or p-terphenyl, an organic material commonly used as a dopant for organic scintillators, as the main component of a scintillator for radiation detection.

P-terphenyl (1,4-diphenylbenzene) is an aromatic hydrocarbon isomer, formed by three benzene rings in ortho position. Pure terphenyl is a white crystalline solid, insoluble in water. Though polychlorinated terphenyls were used as heat storage and transfer agents, *p-terphenyl* is currently under investigation as a material to be used in opto-electronic devices, such as organic LED devices (OLEDs) and is



Figure 3.1. Picture of one of the p -terphenyl samples used for our measurements. The sample shown is 5 mm thick.

currently used in laser dyes and sunscreen lotions.

In particle physics it has been used as a wavelength shifter, exploiting its sensitivity to VUV radiation, to read out scintillation light from liquid Xenon. p -terphenyl has also been used as a doping component for liquid scintillators [25, 26].

In this work I investigated the scintillation properties of poly-crystalline p -terphenyl samples doped by 0.1% in mass of diphenylbutadiene, with respect to organic scintillators.

The more peculiar characteristic of p -terphenyl is that crystals have a Light Yield that strongly depends on the doping: it can thus be significantly increased at the cost of shortening the light attenuation length λ . Usually, this is not convenient, resulting in a remarkable loss of the greater light emitted during the transport. However, in our application this is not a problem.

In fact, aiming at conceiving a small probe for the detection of electrons of few MeV we are compelled to use small crystals, of the order of few millimeters. Moreover, a short λ could even be useful to enhance the spatial resolution of the probe (see Sec. 3.3.3).

Thus, a Light Attenuation Length of the same order of magnitude of the detector size is not a big issue if the gain in light production is convenient [27].

The absolute measurement of the LY of a scintillator depends on the shape and polishing of the sample, on the wrapping and optical coupling to the photodetector, and on the photodetector response. For this reason I measured the light output with respect to the scintillator thickness by using samples of p -terphenyl with 32 mm diameter and 3, 4, and 5 mm high cylinders. One sample is shown in Fig. 3.1. We also combined p -terphenyl samples base-to-base with BC 630 optical grease to increase the total thickness, T , traversed by scintillation light.

In order to study the performances of p -terphenyl as a detector for α particles, electrons and photons, we exposed the samples to a ^{241}Am α source and a ^{137}Cs electron and γ source.

To collect scintillation light, the samples were optically coupled to a Hamamatsu H10580 Photomultiplier (PMT), with spectral sensitivity peaked at 420 nm. The

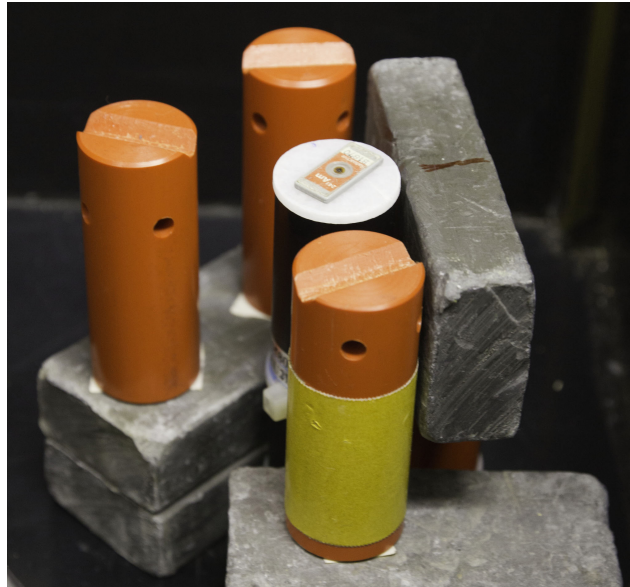


Figure 3.2. Experimental setup used for the measurements with the *p*-terphenyl and various radioactive sources: the black cylinder is the PMT. The whole apparatus was housed inside a black box to shield from environmental light.

typical Quantum Efficiency for this PMT is 25%. We collected the PMT charge with VME standard electronics, using a CAEN V791 QDC to integrate the charge pulses, triggering through NIM standard discriminators and coincidences. We coupled one base of each sample to the PMT with optical grease, while covering the other surfaces with a 15 μm -thick layer of aluminized mylar to increase light collection efficiency. If not otherwise specified, the source was placed in contact with the mylar foil covering the scintillator in order to reduce the material traversed by the radiation. The setup is showed in Fig. 3.2.

3.1.1 Light Attenuation Length

The first investigated property of *p*-terphenyl is the Light Attenuation Length (λ) since it affects all other measurements. The light yield should represent the number of emitted photons per unit of released energy, but the quantity of practical interest for scintillation detectors is the number of photons (L) reaching the photo-detector.

Such number depends on the distance l , travelled by the light from the position of the energy release to the photo-detector, and on the scintillator λ :

$$L = LY \cdot e^{(-l/\lambda)}.$$

An independent measurement of LY thus requires the use of radiation with a penetration range shorter than λ , otherwise the measured quantity would be equal to the convolution between the penetration path distribution and the λ . We therefore exposed our samples, of different thickness T , to non-penetrating α particles from a ^{241}Am , that produces two indistinguishable α lines with mean energy $E_\alpha = 5.48 \text{ MeV}$.

The energy spectra for α particles in the p -terphenyl samples, in units of PMT integrated charge, have been fit with a *Crystal Ball* function, defined as a gaussian function with width σ and mean μ , for $(x - \mu) \geq -a\sigma$, and a power law $A(B - x)^n$ for $(x - \mu) < -a\sigma$, as shown in Fig. 3.3. The dependence of the measured mean released energy (μ) on the sample thickness T (Fig.3.4) was fit with an exponential function, and the resulting effective light attenuation length is:

$$\lambda_m = 4.28 \pm 0.06 \text{ mm.} \quad (3.1)$$

The uncertainty includes the systematic contribution, estimated by adding in quadrature a constant contribution chosen in order to enforce the χ^2 of the fit to equalize the number of degrees of freedom.

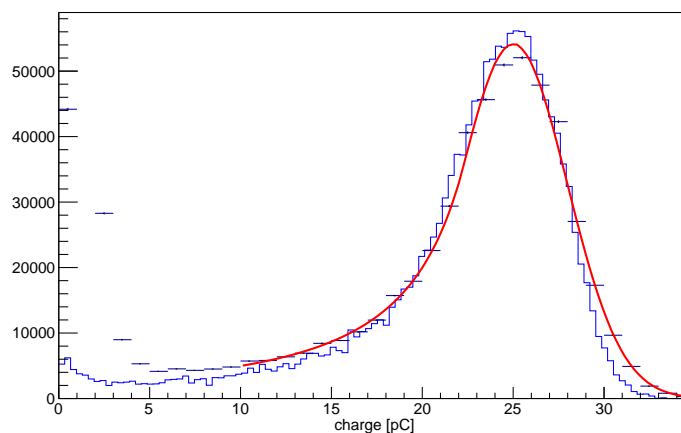


Figure 3.3. Signal spectrum, in units of PMT charge, for the 8 mm p -terphenyl sample exposed to the ^{241}Am α source (dots). The MC spectrum, calibrated and normalized to data, is superimposed (solid line histogram). The superimposed fit is described in the text.

Due to their short range (few tens of microns for 5 MeV in organic scintillators), α particles release all their energy close to the surface of the samples. Scintillation light will then traverse the whole sample thickness before reaching the PMT, plus an additional length due to optical photon angular spread. The measured attenuation length is therefore shorter than the true one.

In order to account for this effect, a devoted simulation with FLUKA was used, as described in Sec. 3.1.4. Detectors of several thicknesses were exposed to the Sr source assuming $\lambda = 5$ mm and executing the same analysis done on data. The dependence of the LY on the thickness is exponential (as in the measurements) but with an effective attenuation length of 4.5 mm.

From this observation we introduced a geometrical correction factor to translate the measured light yield $LY_m(T)$ into the true one:

$$LY_t(T) = LY_m(T) \exp^{T/T_{geom}},$$

and estimated $T_{geom} = 45$ mm. We applied this correction in the measurement of λ , obtaining for the light attenuation length:

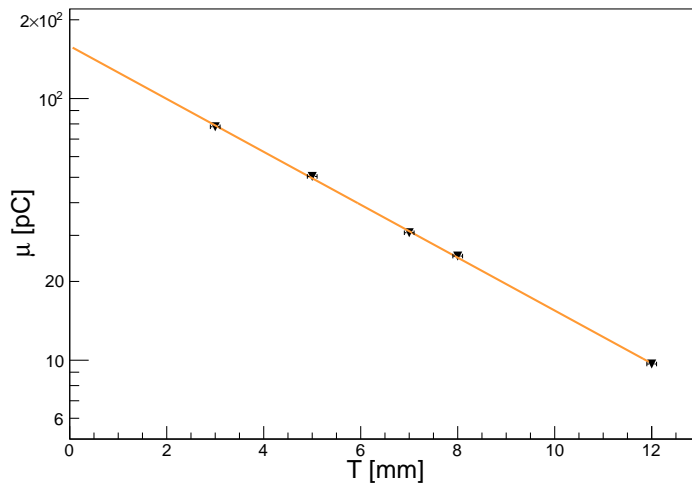


Figure 3.4. Dependence of the mean signal from a ^{241}Am α source on *p*-terphenyl samples as a function of their thickness. The superimposed exponential fit is described in the text.

$$\lambda = 4.73 \pm 0.06 \text{ mm.} \quad (3.2)$$

3.1.2 α -Quenching factor

The differences between α particles and electrons are not only in the penetration range, but also in the emitted light, due to the quenching factor for the formers. To evaluate this effect we used a source of ^{137}Cs , that decays via β^- emission in $^{137}\text{Ba}^*$. Yet, this isotope also emits electrons from internal capture of the 662 keV deexcitation photons from $^{137}\text{Ba}^*$. These electrons have energies of 624 keV (with a 7.8% probability) and 656 keV (with a 1.4% probability) [28]. Photons of 662 keV are hence also produced, but the low Z value of *p*-terphenyl implies a very low detection efficiency. This aspect will be detailed in Sec. 3.1.3. The complete decay scheme is showed in Fig. 3.5.

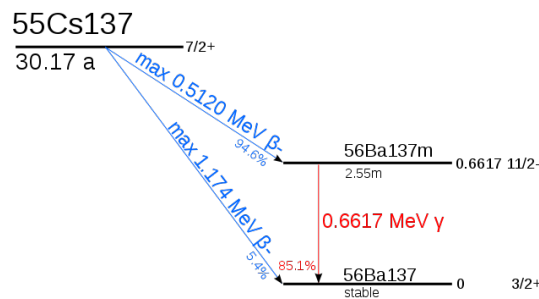


Figure 3.5. Decay scheme of ^{55}Cs .

I acquired energy spectra with the three *p*-terphenyl samples and their combinations. Fig. 3.6 shows a typical charge spectrum with the fit to a gaussian signal, and an exponential function that well reproduces empirically the background due to photons. The μ and σ parameters of the gaussian function are referred to as mean signal and standard deviation, respectively. Fig. 3.7 shows the electron detected

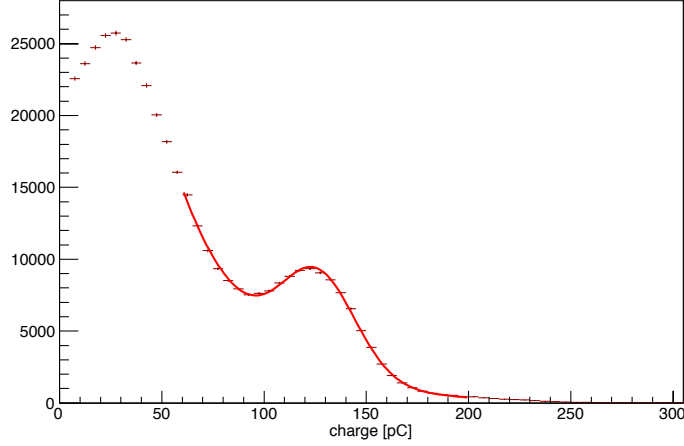


Figure 3.6. Charge spectrum in the 4 mm *p*-terphenyl samples irradiated by ^{137}Cs . The superimposed fit is described in the text.

signal as a function of the thickness, T , for the analyzed samples.

By fitting the distribution of the mean electron signals, μ , as a function of the thickness, T , with an exponential function ($y = LY_e \cdot e^{-x/\lambda_e}$), the Light Attenuation Length was found for the above-mentioned electron energy spectrum to be

$$\lambda_e = 3.89 \pm 0.15 \text{ mm.} \quad (3.3)$$

Quantitatively, the ratio between the effective attenuation length estimated with electrons and the effective attenuation length estimated with α particles is $R_\lambda = 0.82 \pm 0.04$ in data. The lower value of λ_e is due to the electrons inducing scintillation along their path, since their range is ~ 2.5 mm. In the two cases (α and β particles) the scintillation light propagation is different, so the comparison should take this into account.

Comparing the measured signals from electrons and α particles we can extract the α quenching. Accounting for the difference in energy between the electron ($E_e = 629$ keV weighted average energy) and the α lines ($E_\alpha = 5480$ keV on average), the quenching factor Q_α can be estimated as:

$$Q_\alpha = R_{HV} \cdot \frac{LY_\alpha E_e}{LY_e E_\alpha}, \quad (3.4)$$

with $LY_e = 398 \pm 22$ pC obtained from an exponential fit to Fig. 3.7, $LY_\alpha = 160 \pm 4$ pC from the exponential fit to Fig. 3.4, both in units of absolute PMT collected charge. R_{HV} accounts for the different PMT High Voltage (HV) bias used with α particles ($V_\alpha = 1100$ V) and electron source ($V_e = 1300$ V).

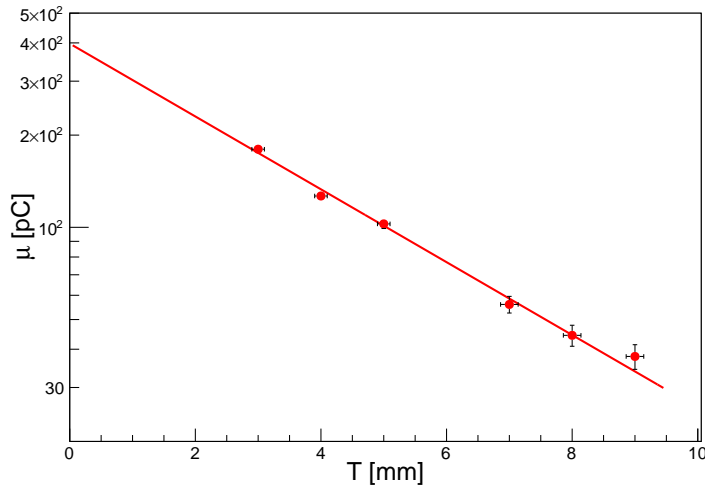


Figure 3.7. Dependence of the mean electron signal on the *p*-terphenyl sample thickness.

To estimate the R_{HV} correction, we measured the PMT gain curve as a function of the PMT High Voltage using a $3 \times 3 \times 5 \text{ cm}^3$ LYSO scintillating crystal coupled to the PMT. We used a ^{137}Cs γ source to excite the scintillation emission from the LYSO. We used the photo-peak from 662 keV photons, visible because of the LYSO high Z , as a reference light source for the photoelectron emission by the PMT photocathode, to measure the charge collected at the PMT anode as a function of the HV. With this setup, and changing the PMT HV bias only, we measured the photo-peak position, q , and its width, $\sigma(q)$, and estimated the PMT gain as

$$G = \frac{\sigma^2(q)}{eq}, \quad (3.5)$$

being e the electron electric charge.

Fig.3.8 shows the measured PMT gain as a function of the HV, and the power law curve ($G = p_0 \cdot V^{p_1}$) used to fit the data distribution. The correction factor is estimated to be $R_{HV} = 2.26 \pm 0.04$. Thus the α quenching factor is

$$Q_\alpha = (10.7 \pm 0.6)\%. \quad (3.6)$$

The Birks' law is an experimental formula that gives the light yield per path length as a function of the energy loss per path length for a particle traversing a scintillator. The relation is:

$$\frac{dL}{dx} = L_0 \frac{\frac{dE}{dx}}{1 + k_B \frac{dE}{dx}}, \quad (3.7)$$

where L_0 and k_B are constants depending on the material [29].

The found α quenching factor corresponds to a k_B factor of 8.3 mg cm^{-2} calculated with a specific energy loss $dE/dx = 0.9 \text{ mg cm}^{-2} \text{ MeV}^{-1}$. This value is in the range of the values obtained for various organic scintillators ([30] and references therein).

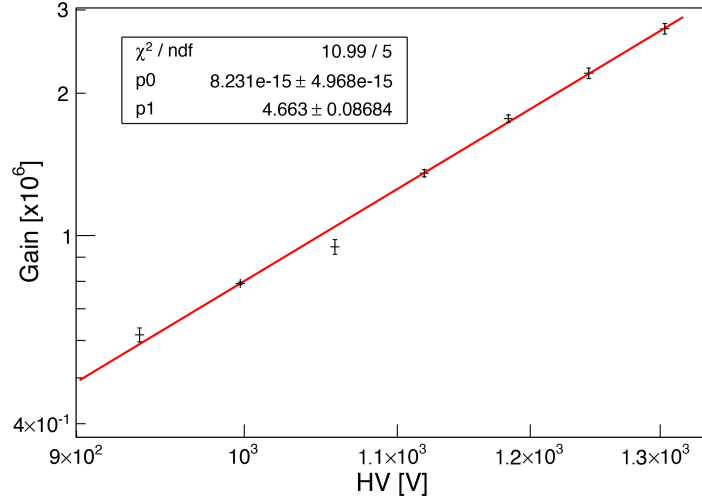


Figure 3.8. Measured PMT gain as a function of the bias HV, on log-log scale. The superimposed fit is described in the text.

It should be noted that a variation in the dopant concentration will modify the quenching mechanisms occurring in the scintillator and thus the measured quenching factor. On the other hand, a different estimation of the specific energy loss of the α particle, depending on the medium density, would result in a different evaluation of the kB factor from the same experimental data.

3.1.3 Photon sensitivity

One of the key-features of the probe to be effective in the Radio Guided Surgery context is its sensitivity to the signal. As stated in Sec. 1.3.2, the idea of using β^- tracers arises from the goal of having a highly specific signal to detect. To this aim, a low sensitivity to every form of pollution must be reached, for example from Bremsstrahlung photons, or photons produced in the decay of a non pure beta emitter isotope. In this perspective, the small photon cross section of *p*-terphenyl, due to its low Z , makes it an ideal candidate material.

In order to quantify the suppression factor of photon detection with respect to electrons, we used the decay properties of ^{137}Cs . As detailed in Sec. 3.1.2, a 662 keV photon is produced in $F_\gamma = 78\%$ of the cases and an almost monochromatic electron from internal capture in $F_e = 8.7\%$ of the cases (the two lines at 624 and 656 keV). While the electron lines appear as a single gaussian distribution in our detector, photons' energy spectrum is continuously decreasing with the increasing energy release. In order to distinguish the photon spectrum in the ^{137}Cs emission, we acquired data interposing a 2 mm aluminum layer between the source and the 3 mm *p*-terphenyl scintillator sample. This layer absorbs the electron component of the ^{137}Cs emission with no appreciable effect on the photon energy spectrum. This effect was validated by means of a devoted simulation, in which the detector is exposed to the ^{90}Sr with and without the interposition of the absorber layer (Fig. 3.10, left). The obtained results showed no significant changes in the photon

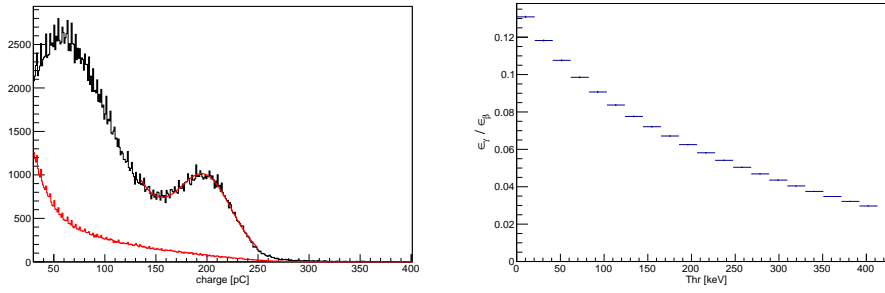


Figure 3.9. Left: ^{137}Cs spectra acquired with (red histogram) and without (black histogram) an aluminum layer in front of the 3 mm p -terhenyl scintillator. The fit superimposed to the latter spectrum allowed us to quantify the internal capture electron component. Right: estimated ratio between the efficiency to detect a 662 keV photon and electron as a function of the threshold.

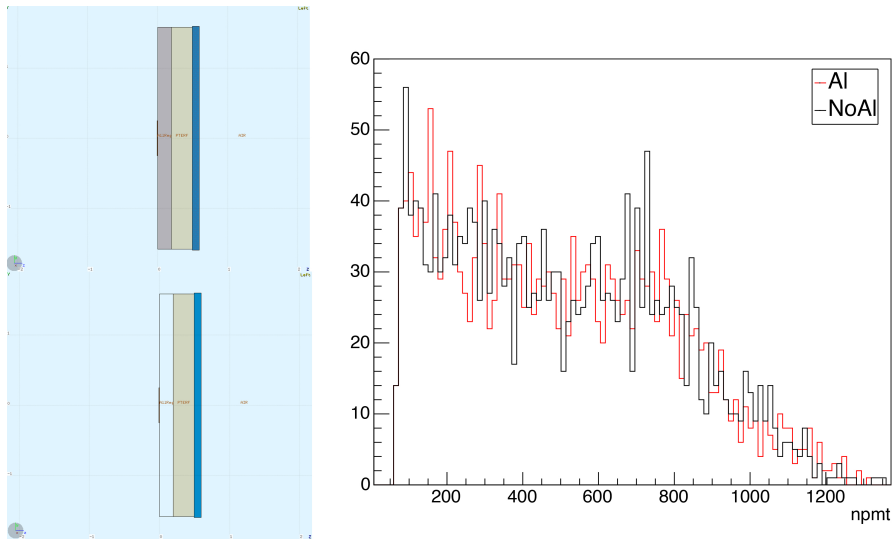


Figure 3.10. Left: setup used for the simulation of the effect of a 2 mm layer of Al interposed between the scintillator and the ^{90}Sr source. Right: obtained spectra for photons with the Al layer (red) and without it (black), in units of number of optical photons arrived at the PMT, as described in 3.2.2.

spectrum detected (Fig. 3.10, right).

The spectra obtained with and without the aluminum layer are shown in Fig. 3.9. The relative efficiency to detect 662 keV photon with respect to a 629 keV electron detection efficiency, R_γ , was estimated with the following technique: the number of observed internal conversion electrons (N_e) was extracted from a gaussian fit to the energy spectrum obtained without the aluminum shield; the number of photons which deposited an energy above a given threshold (E_{thr} , calibrated using the electron spectrum) was estimated by counting the selected events in the spectrum obtained with the aluminum layer ($N_\gamma(E_{thr})$).

R_γ as a function of the threshold was estimated as

$$R_\gamma(E_{thr}) = \frac{N_\gamma(E_{thr})}{N_e} \frac{t_e F_e}{t_\gamma F_\gamma} / C_{geom}, \quad (3.8)$$

with t_γ and t_e the elapsed times during the two acquisitions, F_γ and F_e the fractions of photons and electrons emitted by the ^{137}Cs source as described above, and $C_{geom} = 83\%$ is the correction to the geometrical acceptance due to the aluminum layer interposition, estimated by simulation.

The results are shown in Fig. 3.9 (right): the γ suppression factor, R_γ , ranges between 11% for a 50 keV threshold and 3% for a 300 keV threshold.

3.1.4 Simulation

To support the observations and allow the optimization of the probe, I performed a simulation with FLUKA Monte Carlo software release 2011.2 [23].

Usually, even when simulating scintillators, the production and transport of optical photons is not included. This is done mainly for time consumption reasons: these are in fact cpu-expensive processes to simulate, due to the huge number of scintillation photons generated after energy deposition (of the order of 10 k photons per MeV).

Secondly, accurate results are quickly obtainable by simulating the exact setup without scintillation, and then applying an offline smearing to the energy spectra according to the expected optical resolution.

However, in my simulation I included the full detector geometry and the detailed optical simulation. This last point was made necessary by the short attenuation length of light propagation in *p-terphenyl* (see Sec. 3.1.1), that is accurately simulated by FLUKA and clearly required for the considered study.

The simulations included in this chapter were made with the following parameters:

- energy of the optical photon, $E_{op} = 2.96$ eV;
- attenuation length, λ ;
- fraction of energy deposited in the case of α particles, f_α , which includes the quenching factor, Q_α (Sec. 3.1.2);
- fraction of electron energy deposited in the *p-terphenyl* that is converted into optical photons, f_e .

Fraction of α deposited energy f_α

The f_α parameter in the simulation has been chosen in order to reproduce the experimental energy spectrum obtained exposing the samples to α sources (see 3.1).

The optimal measurement-simulation match, albeit not completely reproducing the low-energy tail, was found for $f_\alpha = 0.01$, and the agreement is shown in Fig. 3.3.

This estimated fraction includes the quenching of the α particles, Q_α as estimated in Sec. 3.1.2.

Fraction of electron deposited energy f_e

We extracted the fraction of electron energy deposited in the *p*-terphenyl that is converted into optical photons using the f_α parameter and the measured Q_α quenching factor: $f_e = f_\alpha/Q_\alpha = 0.1$.

This means that when a 1 MeV electron is absorbed by the *p*-terphenyl, 100 keV of energy are converted into scintillation light.

Light attenuation length

As explained in Sec. 3.1.1, the scintillation light path from α particles includes the scintillator sample thickness T and an additional contribution due to the angular spread of optical photons. The light attenuation length in the MC was set to the measured value $\lambda = 4.73$ mm.

3.2 First probe prototypes

After characterizing of *p*-terphenyl as scintillator, the first prototypes of probe were created, using polycrystalline para-terphenyl doped by 0.1% in mass of diphenylbutadiene.

According to a trade-off between all the above mentioned requirements and the availability of components for such a preliminary study, three prototypes, different in size, geometry and electronics were produced.

3.2.0.1 Probe1

In this prototype (Fig. 3.12, a), the sensitive area is a cylinder of 2.1 mm of diameter and 1.73 mm in height. The *p*-terphenyl is then surrounded by a 7 mm thick layer of black *Polyvinyl chloride* (PVC) to gain lateral shielding, while the front face of the detector is covered by a layer of 400 μm of PVC.

The device is encapsulated inside an easy-to-handle aluminum body, as protection against mechanical stress.

The scintillation light is collected by an optical fiber (1 mm of diameter, \sim 60 cm of length) placed in the center of the bottom face, that carries it to a PMT (Hamamatsu H10721-210). The signal is then read out by a portable custom electronics with wireless connection to a PC or tablet.

The whole apparatus is reported in Fig. 3.11.

3.2.0.2 Probe4

This prototype (Fig. 3.12, b) is essentially similar to the previous one, differing from it only by size. The sensitive area cylinder is in fact of 5.1 mm of diameter and 3 mm in height, while the lateral shielding of PVC is of 3 mm.

The front face is covered by a 10 μm layer of Aluminum.

In this case, the scintillation light is collected by 4 optical fibers of the same size of those in Probe1, and the same electronics is used.



Figure 3.11. Picture of *Probe1* prototype, as described in 3.2.0.1, with the reading apparatus.

3.2.0.3 ProbeSiPm

This prototype (Fig. 3.12, c) is composed by a scintillator cylinder of 10 mm in diameter, 3 mm in height, surrounded by a 5.4 mm layer of PVC.

The front face is covered by a 10 μm layer of Aluminum.

In this prototype, the scintillation light is collected by a *SiPm* detector (*B. Series 10035* by Sensl) directly coupled to the back of the scintillator, with an active area of 1×1 mm.

The signal is then processed by a custom front end electronics based on Arduino system, contained in a aluminum box acting as Faraday cage to screen from possible interferences.

All the three probe prototypes are compatible with a standard sterile covering of sub-millimetric film for surgical environment to be applied during the procedure, and the low biases used (5 V for the PMT, 27 V for SiPm) make the device easily portable.

3.2.1 Probe1 testing

To test functioning and performances of the first probe prototype, a devoted apparatus was conceived. A system of 4 phantoms, simulating cancerous residuals with different topologies, was developed by practicing holes in a Plexiglas plate.

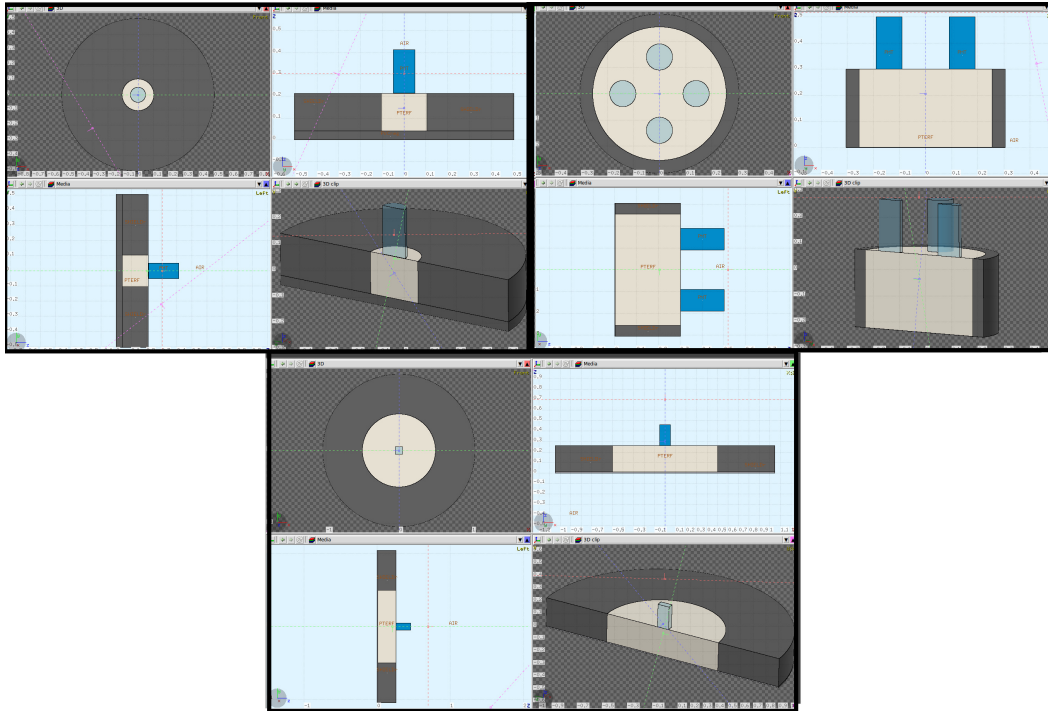


Figure 3.12. The three first prototypes of probes reconstructed in FLUKA. From the top left: Probe1, Probe4, ProbeSiPm. The gray area represents the p-terphenyl, the black is the PVC while the blue is both the optical fiber and the SiPm.

The 0.1 mL volume phantom, referred to as “Residual”, has dimensions compatible with residuals well identified by the Nuclear Magnetic Resonance.

To check the effect of the phantom depth on the probe response and resolution in distinguishing the residual edge, the other three cylindrical phantoms have the same activity concentration, footprint (13 mm^2) but different heights: 1, 2, and 3 mm, referred to as "H1", "H2", "H3" respectively.

The phantoms were filled with ^{90}Y diluted in a physiological saline solution. Thanks to its half life (64 h) a wide range of activity was explored, from 22 to 5 kBq/mL, to be compared with the 20 kBq/mL value estimated by analyzing PET DICOM images administering 3 MBq/kg of ^{68}Ga -DOTATOC to patients affected by meningioma.

The probe performances were therefore studied close and below the activity range commonly used for diagnostic investigation.

A first study consisted in a “blind scan” over the phantoms automatically performed by means of a rotating plate without any human intervention. Even by limiting the acquisition time to 1 s per steps the test demonstrated that all the residuals would be identifiable in absence of background from nearby organs, as seen in Fig. 3.13.

The signal from the tumor residuals was studied at maximum and minimum

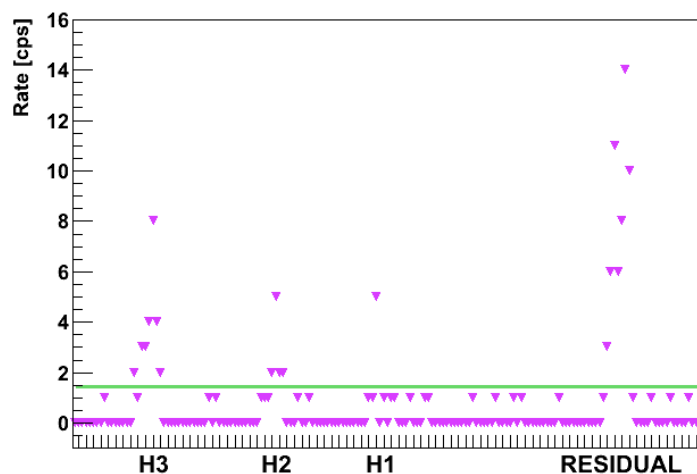


Figure 3.13. Results of a blind automated scan over the different phantoms with an acquisition time of 1 s: in absence of background all the residuals are well identified by the probe.

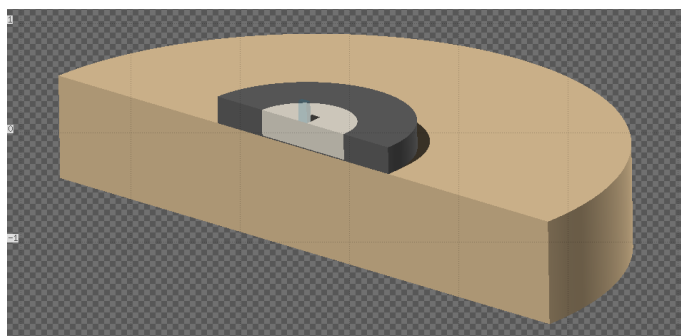


Figure 3.14. Setup of the simulation used to estimate the background from healthy tissue. The brown area under the probe (here Probe SiPm) is muscular tissue with an activity concentration as described in 3.2.1.

activity values, 22 and 5 kBq/mL, and the observed rates are reported in Tab. 3.1.

To take into account the background contribution coming from the uptake of nearby healthy tissue, a FLUKA simulation was used. In this simulation, performed using the parameters obtained in 3.1.4, I tested the response of the probe over a large (some cm in diameter and height, Fig. 3.14) source of ^{90}Y at an activity concentration compatible with the one extracted from DICOM PET files for healthy tissue adjacent to lesions (usually with a 10 : 1 ratio). The procedure used to compare experimental data and simulation will be described in 3.2.2.

From the signal and background rates, taking into account the Poisson fluctuations of the measured counts, we computed the false-positive (FP) and the false-negative (FN) rates for a given time interval measurement with the probe. We estimated (see Tab. 3.1) the time needed to achieve $\text{FP} \approx 1\%$ and $\text{FN} < 5\%$ and found it to be 1 s for 22 kBq/mL activity and up to 10 s in the case of activity as

low as 5 kBq/mL.

Keeping in mind that this techniques is at its earliest stages, and that the doses to be administered will have to be chosen after an accurate evaluation of risks and benefits, it is evident that being a first test of the first probe these are encouraging results, even if large room for improvement remains.

Phantom	Diameter (mm)	Height (mm)	Volume (ml)	T (s)		Rate (cps)	
				@ 22 kBq/ml	@ 5 kBq/ml	@ 22 kBq/ml	@ 5 kBq/ml
Residual	6	3.5	0.10	31.6	1	6.6	2
H1	4	1	0.01	12.4	2	2.6	>10
H2	4	2	0.02	17.7	1	3.7	4
H3	4	3	0.04	20.1	1	4.2	4

Table 3.1. Results of the test on the first probe prototype. The probe was tested on phantoms sized as possible tumor residuals of interest, filled with ^{90}Y in saline solution to simulate the situation after bulk meningioma removal. The rates measured with two different ^{90}Y activity concentrations (22 and 5 kBq/mL) are reported (Rate). The minimal acquisition time (T) needed to detect tumor residuals with a false-negative probability $<5\%$ and a false-positive probability 1% was estimated extrapolating the laboratory test results to a real case by means of a detailed simulation

Lastly, the effect of an off-axis measurement has been verified by moving the probe away from the phantom centre.

The test showed that the rate is reduced by a factor 2 when moving the probe 0.5 mm far from the phantom edge (Fig. 3.15). This allows to conclude that the probe distinguishes the residual edge.

This test also demonstrated the lateral shielding effectiveness of this prototype making the probe insensitive to electrons coming from the sides, hence increasing the tumor-spotting capability. The optimization of such lateral shielding will be discussed in 3.3.2.1.

3.2.2 Comparison between data and simulation

In order to compare the results from the FLUKA simulation with the experimental data, a calibration is needed.

In fact, when taking into account scintillation, simulated energy spectra in the detector are given as histogram of the number of optical photons reaching the PMT surface ($npmt$). Thus, all spectra shapes and rate calculations are related to this quantity: rates are infact obtained by integrating the number of entries above a certain threshold expressed in $npmt$ unit.

On the other hand, experimental data are usually provided in mV unit. However, the theoretical conversion between these two units is practically impossible to do, being the number of optical photons read dependent on a number of very uncertain parameters (light yield, quantum efficiency of the PMT, etc.).

For this reason, an appropriate setup was designed and built in both the laboratory and the simulation to measure the conversion factor under our experimental conditions, being this a conversion that strongly depends on the readout system.

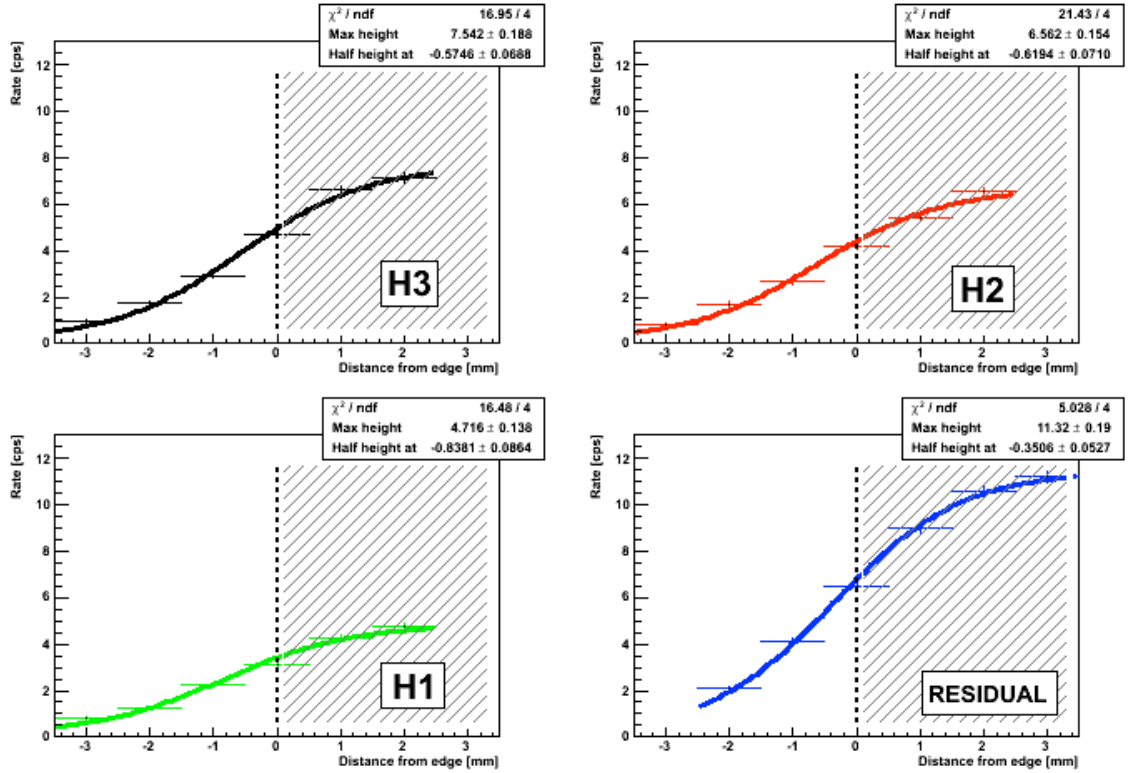


Figure 3.15. Rates obtained by moving the probe laterally with respect to the phantom center for each phantom fitted with a sigmoid curve.

The three probe prototypes were placed over a ^{90}Sr source of known activity, and the counting rates were measured varying the threshold used for integration. In parallel, the same setup was simulated in FLUKA, exposing the probes to a point like source of the same type (isotope and activity).

A scan in threshold was then performed in the simulation output, aiming at reproducing the measured rate. The results, in term of ratio between “software threshold” and “hardware threshold” are shown in Fig. 3.16. From the fits to these values, the following conversion factor for each probe were obtained:

$$\text{Probe1} : \frac{THR_{SW}}{THR_{HW}} = 2.7;$$

$$\text{Probe4} : \frac{THR_{SW}}{THR_{HW}} = 1.52;$$

$$\text{ProbeSiPm} : \frac{THR_{SW}}{THR_{HW}} = 6.8.$$

3.3 Probes optimization and development

In Sec. 3.2 the first prototypes of probes were described. Starting from them, further developments and optimizations are achievable to improve the performance

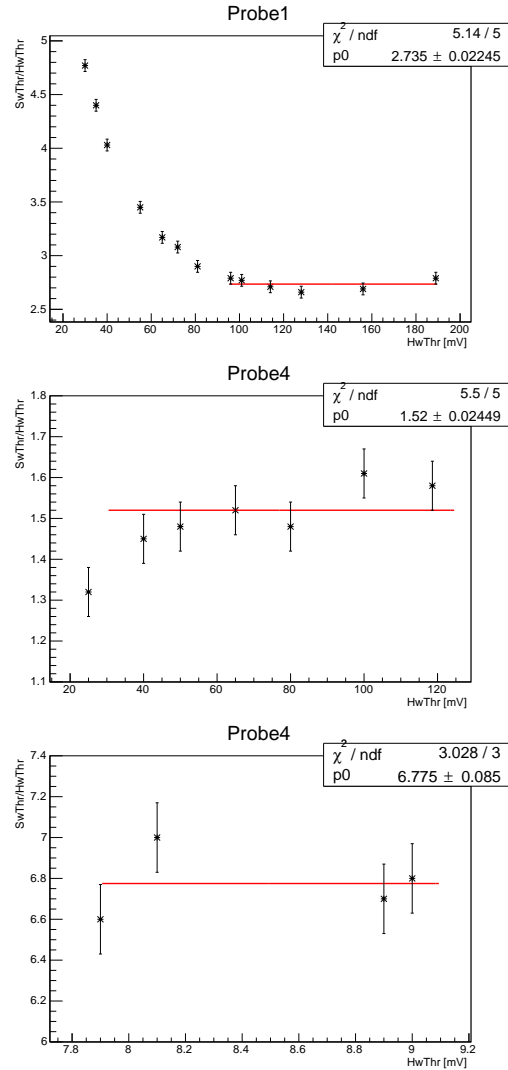


Figure 3.16. Extraction of the conversion factor between “software threshold” and “hardware threshold”, as explained in 3.2.2, for *Probe1* (top), *Probe4* (center) and *ProbeSiPm* (bottom). In the first two cases the fit was performed only over a certain hardware threshold below which the electronic noise is dominant. A flat trend was assumed, and the errors have been calculated by forcing the χ^2 to be equal to the *ndf*.

of the detector, regarding the characteristics of the active material (chemical and mechanical), the shielding and the readout system.

3.3.1 Spectrophotometry

As seen in Sec. 3.1, one of the key feature of p-terphenyl is its large light production.

Basing greatly on this characteristic the effectiveness of the detector, it is crucial to optimize all the steps between the production of scintillation light and its detection. For this purpose, a spectrophotometric study was carried out on a sample of p-terphenyl of the same type of those used for the first prototypes to verify that the Photo Multiplier Tube is appropriate for the frequencies emitted by the crystal.

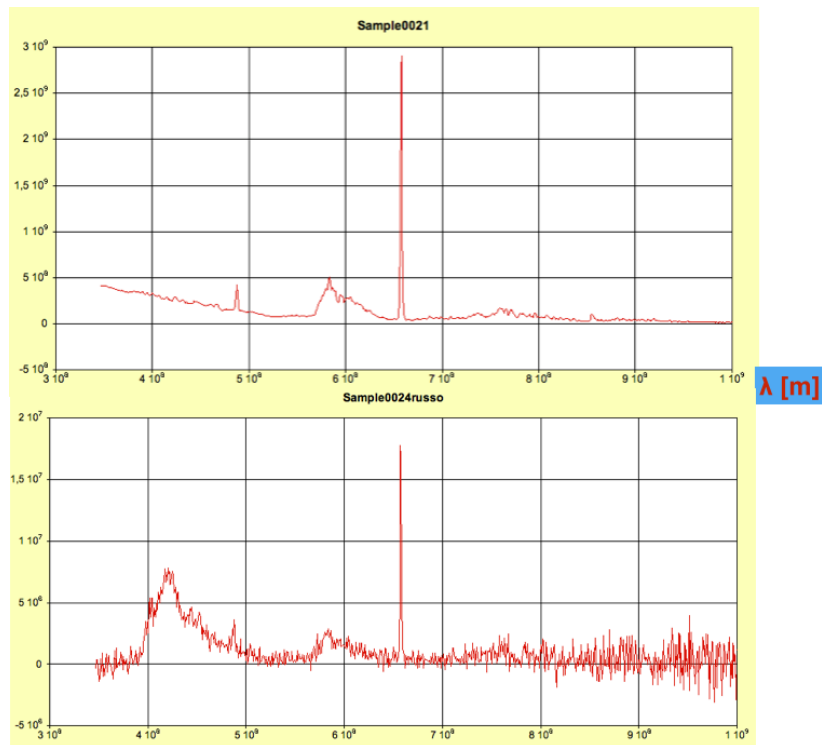


Figure 3.17. Spectrum of light transmitted through the p-terphenyl sample (bottom), and in absence of the sample (top). It is clearly showed that the emitted light populates the zone around 450 nm.

The study made use of a Photonic Multichannel Analyzer (mod. PMA-12 C10027-02 from Hamamatsu) and a Deuterium UV Lamp.

The light emitted from the lamp was carried by an optical fiber to the front face of the investigated sample, housed in a devoted support. Another optical fiber, placed on the opposite side of the sample carries the transmitted light to the Spectrophometer.

The obtained spectrum is showed in Fig. 3.17, together with the one in absence of the sample, to show the spectral components of the used UV lights.

The study showed that the emitted light is in the range of 400 – 450 nm, i.e. the edge of visible light, which is a zone commonly well covered by standard PMT, and also by the one used in the first prototypes.

It has to be noted that this emitted spectrum is due to the doping with diphenylbutadiene, being the pure p-terphenyl supposed to scintillate in the near UV region.

In conclusion, this study confirms that the kind of *p-terphenyl* and the PMT used for these prototypes are an effective match.

3.3.2 Active area optimization

In Sec. 3.1.1 was pointed out how the light yield of p-terphenyl is enhanced at the cost of shortening the light attenuation length λ , that in the case of our samples was found to be 4.73 ± 0.06 mm (eq. 3.2).

This peculiar characteristic of the sensitive material puts some unusual constraints on the optimal detector size. In fact, if normally an increase in the size of the detector would result in a augmented signal, being the only limitation factor the detector size itself, in this case a tradeoff between produced and lost light, due to λ , arises.

3.3.2.1 Size scan simulation

The aforementioned characteristics of p-terphenyl call for a careful optimization of the size of the sensitive area. For these reason, a study was carried out by means of a simulation of a number of different geometrical configurations.

Starting from a detector sized as the one in *ProbeSiPm* (see. Sec 3.2.0.3), both the p-terphenyl radius and height were ranged, the former between the values 1, 2.5, 4, 6 and 8 mm, and the latter between 2, 4, 5, 6 and 8 mm. A total number of 25 different configurations were hence obtained.

Each probe was simulated in the already used hypothetical setup of ^{90}Y source, with an high activity area (“residual”, $r = 3$ mm, $h = 5$ mm) surrounded by a low activity one (“background”, $r = 2$ cm, $h = 1$ cm), being the ratio between activities 10:1.

For each configuration, both the rate from the background and from the residual were evaluated, by means of the conversion factor between hardware threshold and simulation described in 3.2.2. The results are summarized in Fig. 3.18, in which the S+B rate (“background”+“residual”) is plotted versus the “background” rate.

Given the linear shape of the plot, the “best” configuration has to be considered the last in the top right, which corresponds to the best compromise between the two contributions.

The upper plot in Fig. 3.18, grouping the configurations according to detector height shows no significative prevalence between them regarding the top right configurations.

However, the bottom plot therein, collecting the points according to the radius of the detector, shows clearly that the best performance is obtained for a detector radius of 2.5 mm.

Regarding the detector height, this study suggests that there is no great difference between different configuration, at least in this range of values.

On the other hand, coming to the detector radius, this study leads to a result that is at the same time intuitive and non-trivial: the best radius is the one comparable with the one of the “residual” to be detected (3 mm in this case).

Despite being a comprehensible indication, it is a quiet tricky one in the context of a probe for Radio Guided Surgery, in which the size of the object to detect is not known a-priori, and there is instead great variability in it.

This study then enforces the idea to develop a “multi-probe system”, composed by for example two different probes: a larger one to detect wider tumors, and a smaller one to detect residuals.

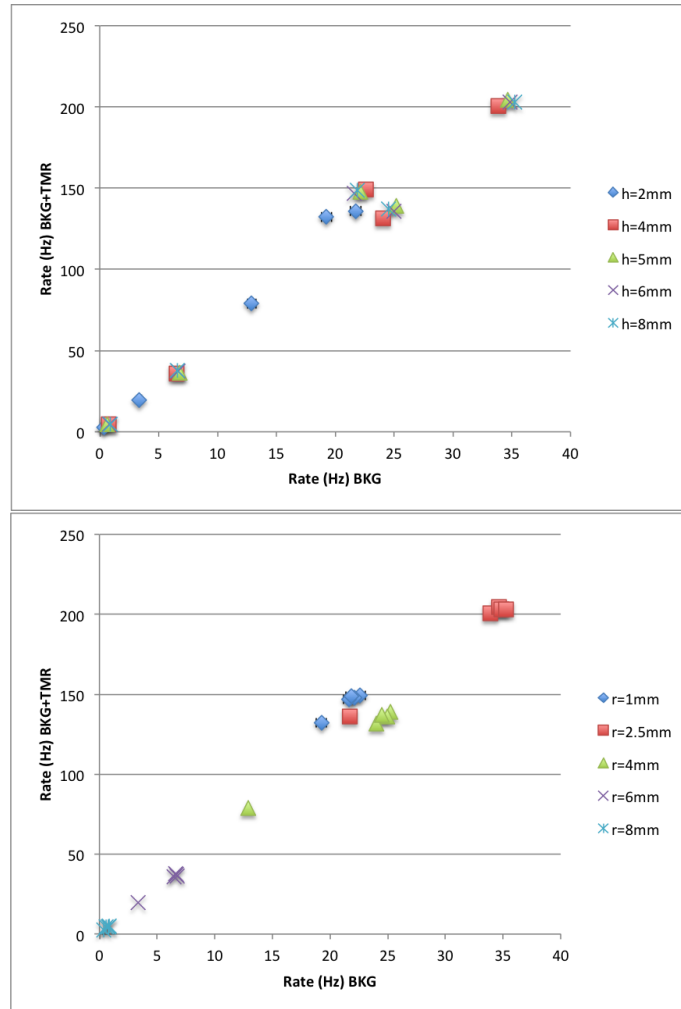


Figure 3.18. Results of the optimization study for the sensitive area, as described in Sec. 3.3.2.1.

3.3.3 Shielding optimization

The other component of the probe strongly influencing both performance and dimensions is the shielding, that constitutes also the housing for the detector, as seen in Sec 3.2.

In these first prototypes of probes, there are two sort of shielding: a frontal one and a lateral one.

Regarding the front shielding, the question is almost straightforward: the thinner is the shielding, the higher is the sensitivity, and thus the rate. The only constraints are put by simple mechanical arguments (malleability and resistance of the material) and physical reasons (opacity to ambient and contamination light). The actual frontal shielding for the examined first prototypes described in Sec. 3.2 already reflect the optimal point in this balance.

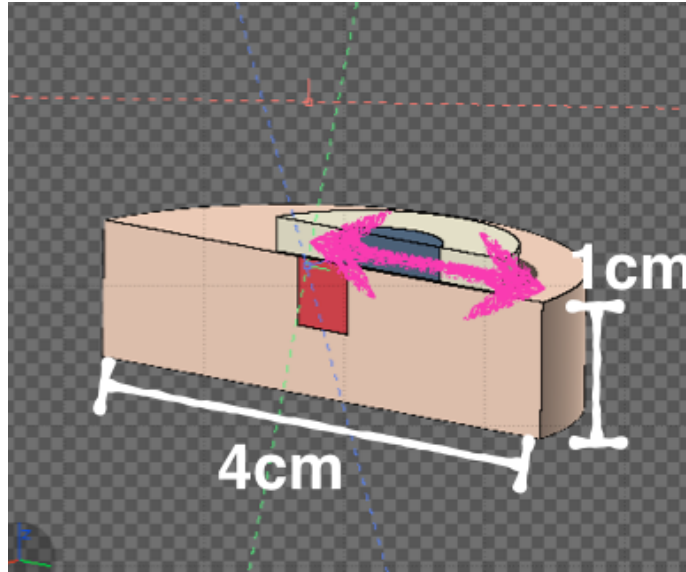


Figure 3.19. Simulation of the movement of the probe upon the source, as described in Sec. 3.3.3.

Regarding lateral shielding, on the other hand, the optimization is much less straightforward, and requires a tailored study.

For this purpose, a setup similar to the one described in 3.3.2.1 was simulated. The source is composed by a “residual” cylinder ($r = 3$ mm, $h = 3.5$ mm) nested within a “background” zone ($r = 2$ cm, $h = 1$ cm), being the ratio between the ^{90}Y activities of the two zones 10:1.

A number of different probe configurations were exposed to such a source, starting from the three prototypes presented in Sec. 3.2 and varying the thickness of the shielding (0.5, 1, 2, 3, 4, 7 mm).

In such a setup, the principal effect of the lateral shielding is against the side contribution to the signal, thus directly influencing the spatial resolution of the probe. To evaluate it, the movement of the probe over the source was simulated, starting from a centered configuration and moving laterally until a distance of 15 mm between the axis of the residual and that of the probe (see Fig. 3.19).

For each point in the scanning and each probe configuration the rate was evaluated by means of the procedure described in Sec. 3.2.2. The results, normalized to the case without shielding, are showed in Fig. 3.20 (a, b, c).

Fig. 3.20 (d) shows the spatial resolution, obtained as the σ from a Gaussian fit to the spectra (considering the background as a constant in the examined range). The dotted lines represent (via the corresponding color) the actual thickness of the shielding for each existing probe prototype.

It is evident that both Probe1 and Probe4 (described in Sec. 3.2) could benefit of a reduction in the shielding of about 1 – 2 mm without any loss in spatial resolution, rather gaining in occupancy. On the other hand, it is clearly highlighted that the lateral shielding has actually no effect on the performance of ProbeSiPm, being the spatial resolution constant for all the examined configurations.

This phenomenon is explained by the traverse size of the sensitive area in this

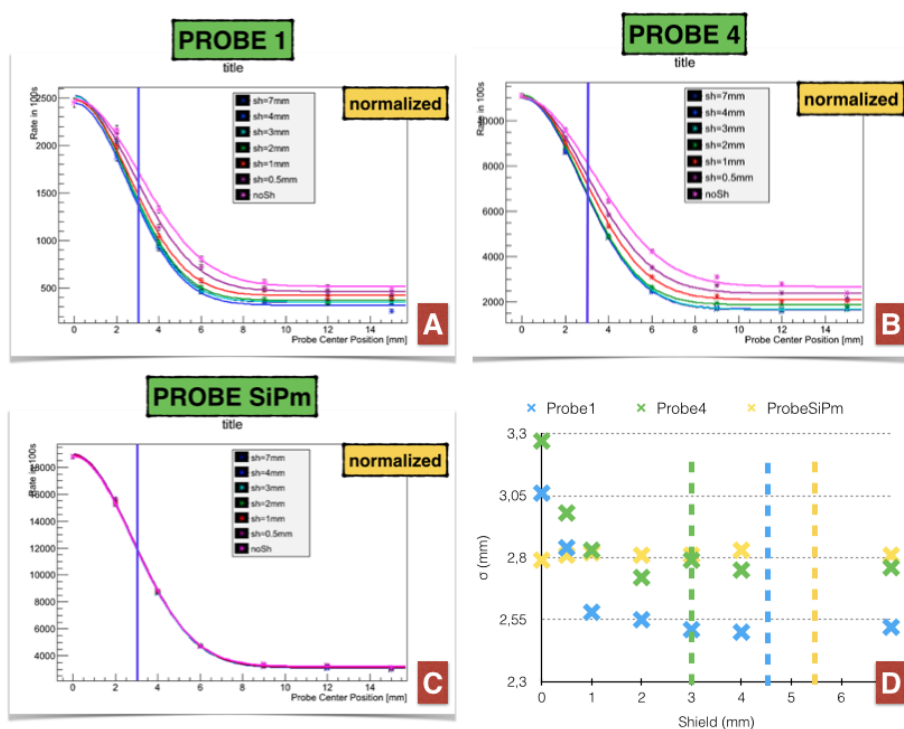


Figure 3.20. (a, b, c) Simulated rate moving the probe over source for various shielding thickness, as described in Sec. 3.3.3. In each plot, the rates are normalized to the no-shielding case, in order to gain readability, and the purple line represents the edge of the “tumor”. (d) Spatial resolution vs shielding thickness for the three prototypes.

probe (10 mm in diameter) that is large compared to the one of the area to detect. For such a reason, the shielding is provided in some sense by the p-terphenyl itself, due to its short attenuation length (Sec. 3.1.1). The light originating from interactions near the borders of the sensitive area has to traverse a long path to reach the PMT, and is thus statistically shrank by attenuation.

It is clear that this is not a wise way of doing, but rather a consequence of the arguments discussed at the end of Sec. 3.3.2.1 regarding the relation between the radii of detector and “residual”.

ProbeSiPm, despite having shown to be poorly efficient in such a setup, is likely to be the most effective one in case of wider target to detect.

To sum up, these studies suggest that despite although there is room for several minor improvements, the first three probe prototypes presented in Sec. 3.2 provide a good diversified basis of tool to study several fields of applications.

Chapter 4

Medical Applications

In Chapter 1 a comprehensive summary of the actual status of tumor surgery was outlined. In Sec. 1.1 the utmost importance of full tumor resection was highlighted, and a review of all the available techniques to this purpose was presented.

In this Chapter, possible applications of the probe which development is treated in this Thesis work are presented. In particular, the focus will be put on two fields: Brain Surgery (Sec. 4.1) and Neuroendocrine Tumors Surgery (Sec. 4.2).

4.1 Brain Surgery

As discussed in Chapter 1, the field that would probably profit most from such an innovative Radio Guided Surgery technique is brain surgery.

In the following Sections, after a brief overview of the Brain structure and the characteristics of cerebral tumors, it will be presented a study devoted to evaluate the applicability in this field of the so far discussed β^- -RGS technique.

4.1.1 Human brain structure and cerebral tumors

The brain is the most complex organ of the entire human body, and together with the spinal cord forms the Central Nervous System (C.N.S.).

It consists of an oval shape mass about $17 \times 14 \times 13$ cm in length, width and height, weighing about 1200 – 1400 g depending on the sex.

The human brain is situated within the braincase, in which it is enveloped by a system of membranes called Meninges, Fig. 4.1.

The one closest to the skull is called *Dura Mater*, and is formed by dense connective tissue; this membrane is strictly connected to the intermediate one, called *Arachnoid*, due to its spider web-like appearance, that does not follow the convolutions of the surface of the brain.

Inside this membrane there is a space filled with *cerebrospinal fluid*, that is the same liquid present in the spinal cord.

The innermost membrane is the *Pia Mater*, which firmly adheres to the surface of the brain and spinal cord, following the brain's minor contours.

The entire brain is divided in two *hemispheres* by a deep longitudinal sulcus, called *Medial Longitudinal Fissure*, from which other fissures originate, the deeper of which divide hemispheres in lobes.

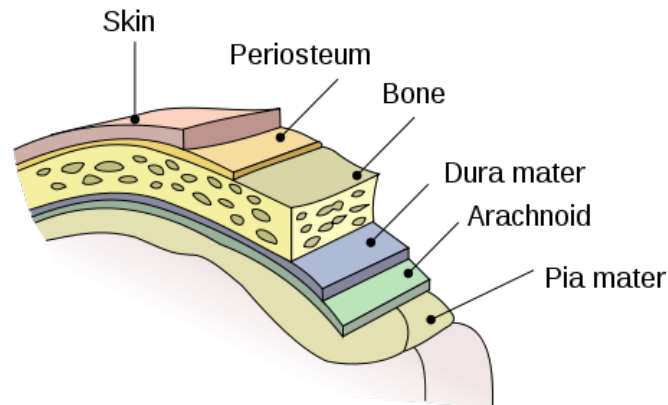


Figure 4.1. The meninges: dura mater, arahnoid mater and pia mater.

The whole brain is made of two kind of substances: the *gray matter*, consisting of neuronal cell bodies, glial cells and capillaries, located in the surface forming the cortex and the *white matter*, located more in depth and composed by the axons of the neuronal cells.

4.1.1.1 Cerebral Tumors and classification

A tumor is an abnormal formation of cells that loose some of their properties and start growing in an uncontrolled way.

One of the damaged mechanism is in fact the one responsible for the growth control, called *apoptosys*, and cancer cells thus duplicate very quickly without limits.

In order to accurately diagnose, follow and treat tumors, a precise classification is needed.

Cerebral tumors can be divided in two groups: *primary* and *metastatic* ones.

Primary tumors are those originating from brain or its membranes, while metastatic, or secondary ones are those originating in other parts of the body that have spread through blood to the brain.

Primary tumors can be both benign or malignant, while secondary ones are always malign.

Benign tumors are usually characterized by slow growth and clearly defined margins with adjacent tissue, and can be cured if completely removed by surgical procedure. Therefore, benign tumors are normally not dangerous.

However, this is not the case of brain. In fact, being this organ confined within the rigid brain case, each anomalous growth implies an increase on other tissues of the brain, with a consequent alteration in functioning.

Moreover, the surgical procedure required to resect the mass is always dangerous for the patient in term of survival and neurological outcome. A typical example of benign cerebral tumor is *Meningioma*.

Malignant tumors are usually characterized by rapid growth, often infiltrating the surrounding healthy tissues, with the consequence of not well defined margins. For this reasons, the complete resection of malign tumors is a difficult task, as

discussed in Sec. 1.1.

The malignancy of a cerebral tumor is measured in *grades* relying on appearance on the microscope, tendency to infiltrate and rapidity to increase. There are 4 grades of malignancy:

1. *Grade 1* tumors are benign, slowly growing and do not infiltrate surrounding tissue; the cells look almost natural under microscope. Rare in adults.
2. *Grade 2* tumors have low malignancy and relative slow growth, can infiltrate nearby tissue and give origin to recurrences, that are often of higher grade; cells look slightly abnormal under microscope.
3. *Grade 3* tumors are malign, formed by abnormal cells actively reproducing and infiltrating. Tendency to come back as higher grade tumors.
4. *Grade 4* tumors are the most malignant, growing fast, spreading into nearby normal parts of the brain, characterized by very abnormal cells actively reproducing and formation of new blood vessels to maintain rapid growth. Areas of dead cells in the center are commonly present (*necrosis*).

Cerebral tumors show great variability in terms of grade of malignancy, location and kind of tissue from which they originate.

Tumors originating from Meninges are called *Meningioma*: with very few exceptions they are benign and slowly growing.

Tumors from cranial nerves are called *Schwannoma*, are benign with less than 1% of cases evolving in malignant forms, slowly growing and rarely give recurrences once surgically removed.

The pituitary gland is the origin of *Pituitary Adenoma*, which is in the majority of the cases benign.

All these tumors, despite being benign, can in principle become malignant, and are likely to give recurrences even after several years after an incomplete surgical resection.

Tumors originating from glial cells or astrocytes, that are non-neuronal cells that maintain homeostasis, form myelin, and provide support and protection for neurons in the brain, are called *Glioma*.

The incidence of several kind of brain tumors is showed in Tab. 4.1.

Cerebral Tumor	Annual incidence
Glioblastoma multiforme	2-3
Anaplastic Astrocytoma	3
Oligodendroma	0.4
Low Grade Glioma	1
Meningioma	0.17

Table 4.1. Annual incidence of cerebral tumors on a sample of 100000 people.

Tumor Type	3-y survival	5-y survival	10-y survival
Benign	86.3%	74.3%	66.7%
Atypical	66.6%	58.3%	33.3%
Anaplastic	33.3%	8.3%	0%

Table 4.2. Outcome of meningiomas [33].

Meningioma

Meningiomas are the most common intracranial tumors originating from the arachnoid membrane, which is the intermediate one, very thin and delicate.

Meningiomas are benign in 92% of cases, with 8% being either atypical or malignant [31], and can be further classified according to W.H.O. [32]:

1. *Benign Meningioma* (grade 1): benign tumor that can eventually recur especially following an incomplete surgical removal. The standard treatment is surgery, and radiotherapy is considered only in case of residual lesions.
2. *Atypical Meningioma* (grade 2): shows high tendency to infiltrate surrounding tissue, nonetheless is often considered not malign. Recurrency rate is 41.6% [33].
3. *Anaplastic Meningioma* (grade 3): the most aggressive and infiltrating, are not curable with the sole surgery intervention. Recurrency rate is 75% [33].

Table 4.2 shows the survival rates at 3, 5 and 10 years for the different kind of tumors.

Meningiomas are more likely to appear in women than men, though when they appear in men, are more likely to be malignant. Meningiomas can appear at any age, but most commonly are noticed in men and women age 50 or older, with meningiomas becoming more likely with age.

Glioma

Gliomas are tumors originating from *glial* cells. This cells are the most common in the brain, constituting about half of its volume, and therefore have an enormous potential abnormal growth.

Common characteristic among these tumors is the intracranial growth that determines a generic state of suffering on the whole brain. Gliomas are commonly located on the cerebral hemispheres, more rarely in brainstem, cerebellum and optic nerve.

Gliomas represent the most frequent primitive tumors in adult population, and are classified according to the cells they originate from and their malignancy grade:

1. *Astrocytoma*:
 - *Low Malignancy Astrocytoma* (grade 1 and 2):
 - *pilocytic astrocytoma*: low malignancy tumor, non infiltrating, slowly growing, but can nonetheless give symptoms due to compression;
 - *diffused astrocytoma*: grade 2 tumor, often infiltrating, relatively slowly growing.

- *High Malignancy Astrocytoma* (grade 3 and 4):
 - *anaplastic astrocytoma*: rapidly growing and infiltrating, recurrences manifests usually within 2 years;
 - *glioblastoma multiforme*: is the most aggressive and malignant one, growing fast and extensively infiltrating nearby tissue. Recurrence appears in 50% of cases within 8-9 months. It is also the most difficult to cure, being little sensitive to both chemotherapy and radiotherapy, and being surgical resection difficult to be obtain (see Sec.1.1). Prognosis is poor for the patient, with a short survival.

2. *Oligodendroglioma*:

- *Oligodendroglioma*: cerebral tumor of grade 2, low malignancy and slow growth. Standard treatment consists of an as complete as possible surgical resection;
- *Anaplastic oligodendroglioma*: grade 3 neoplasm, rapid growth.

3. *Ependymoma*:

- *Ependymoma*: low malignancy slowly growing tumor. Standard treatment is surgery followed by radiotherapy on the tumoral site.
- *Anaplastic Ependymoma*: grade 3 tumor with higher malignancy that can metastasize through the cerebrospinal fluid. Standard treatment involves surgical resection followed by cranial irradiation and eventual spinal irradiation in case of presence of neoplastic cells.

4.1.1.2 Therapy

Benign cerebral tumors are often successfully treated. On the contrary, patients affected by malignant disease of the NSC have usually limited survival; nevertheless, their quality of life can be significantly increased by the collaboration between several physicians and different expertise and approaches.

The principal technique used against these cancers are three: surgery, chemotherapy and radiotherapy.

Surgery

How was pointed out in Sec. 1.1, surgery is the golden standard treatment at least for primary brain tumors, craving at the complete resection of the diseased mass.

Regrettably, this goal is not always achievable due to tumor size, kind or positioning. In that case, surgery aims at a partial resection, in order to relieve symptoms.

Only in rare cases, due to patient's general clinical conditions or for the complex nature of the lesion, surgery is not the preferred option, and nuclear physicians and oncologists plan a treatment tailored to the case.

The surgical procedure consists of a *craniotomy* (Fig. 4.3, top), in which a bone flap is temporarily removed from the skull to access the brain. Depending on the site and size of the considered tumor, the excision of other elements can be necessary (e.g. meninges, Fig. 4.3, bottom).



Figure 4.2. Comparison of primary *Glioma* (left) and *Meningioma* (right) at MRI.

As a consequence, surgery can eventually comport several kind of damages, as motion, senses, sight, language, loss of memory and cognitive deficits both of transitional or permanent nature.

Chemotherapy

Chemotherapy uses one or more anti-cancer drugs that are administered systemically to the patient.

Traditional chemotherapeutic agents act by killing cells that divide rapidly, that, as mentioned before, is one of the peculiar characteristics of tumor cells. However, this feature is common also among several healthy cells, such as bone marrow, digestive tract and hair follicles. This results in the most common side effects of chemotherapy, that are decrease in the production of blood cells (*myelosuppression*), inflammation of the digestive tract and hair loss.

Recently, new anticancer drugs have been developed, such as monoclonal antibodies, that are not indiscriminately cytotoxic, but rather target proteins that are abnormally expressed in cancer cells. However, the feasibility of this last approach is strongly limited by cost reasons, being the production of such targeted antibodies a complex procedure.

In the case of brain tumors the drug can be administered systemically or directly

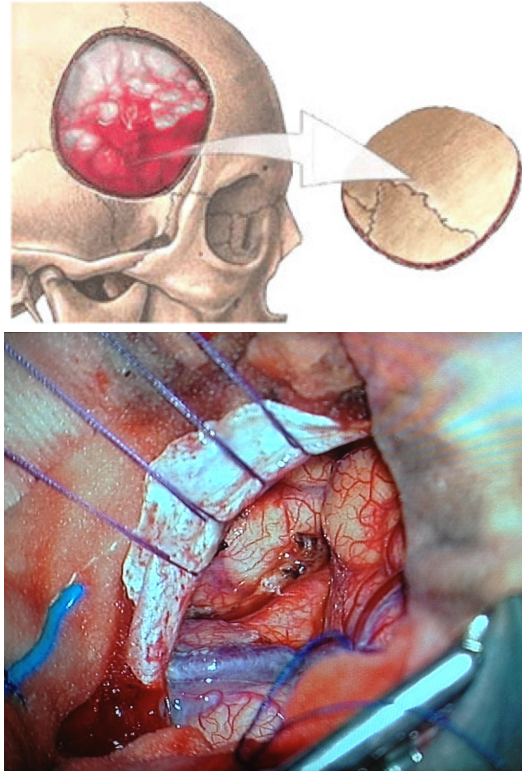


Figure 4.3. Steps of the surgical intervention of a meningioma: *craniotomy*, on the top, and the proper surgical field on the bottom. The white folded layer is the *dura mater*, removed to reach the lesion.

injected between the membranes. However, the main obstacle for chemotherapeutic agents to be effective in the brain is represented by the *Blood-Brain Barrier*, that prevents the great majority of common drugs from reaching in sufficient (therapeutic) quantities the Brain.

This result in a limited number of agents available for chemotherapy of cerebral cancers.

Radiotherapy

Radiotherapy can be used as a stand-alone treatment, or in association with chemotherapy soon after the surgical intervention.

Conventional radiotherapy makes use of *X rays* to kill or damage tumoral cells. However, photons and electrons release an amount of energy that is almost constant with the matter traversed, as showed in Fig. 4.4. This means that to hit the tumor, an amount of dose (and hence of damage) of the same order of magnitude must be given to the healthy surrounding tissues. This is a major drawback for this technique, in particular in an organ such the brain, where each zone has a precise and fundamental role.

To overcome this limitation, *Intensity Modulated Radio Therapy* (IMRT) has been developed, exploiting the superimposition of several radiation beams in order to maximize the conformation of the dose on the tumor (Fig. 4.5).

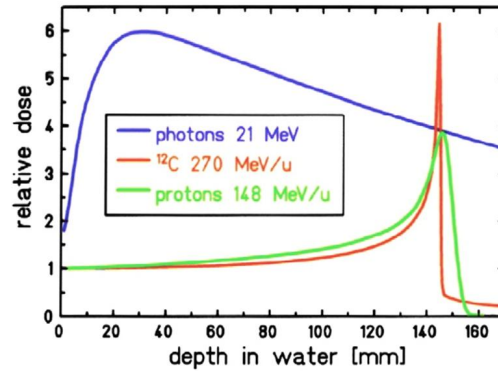


Figure 4.4. Dose released as a function of the depth traversed for photons, protons and Carbon Ions.

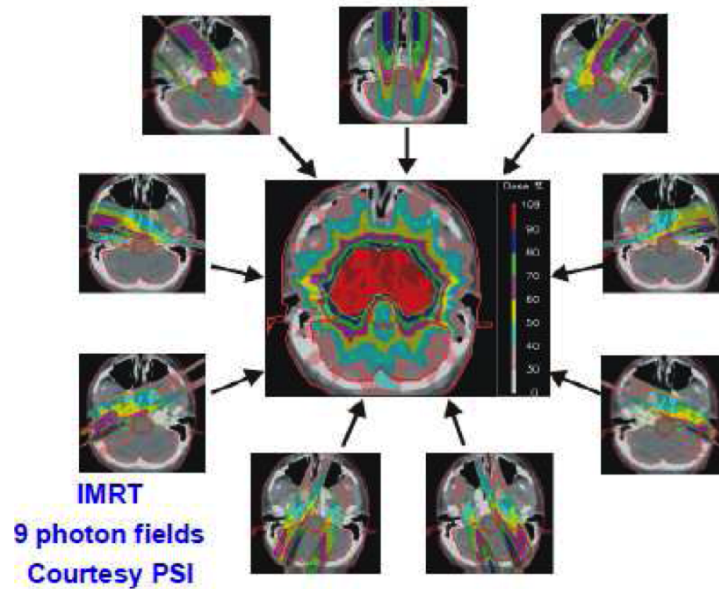


Figure 4.5. Example of dose released in a IMRT treatment with the superimposition of 9 beams.

A further and relatively recent approach to radiotherapy, named *Hadrotherapy*, makes use of charged hadrons, such as protons or Carbon ions, that are characterized by a peculiar dose release profile that concentrates the great majority of their release at the end of their range in the tissue, in a zone named *Bragg Peak* (Fig. 4.4).

This characteristic permits a huge conformability of the treatment to the considered target, and the enhanced ability to destroy cancer cells of hadrons with respect to photons makes this treatment highly effective.

However, cost reasons following the need of particle accelerators for hadrontherapy imply that today IMRT is the standard treatment for the vast majority of tumors.

In case of small cerebral lesions, for example metastasis, a particular technique named *Gamma Knife* can be applied. In this technique a massive dose of radiation coming from a radioactive source is administered in one single fraction to a small volume. The apparatus in which the patient is inserted is shown in Fig. 4.6.

A Gamma Knife typically contains 200 ^{60}Co sources of approximately 1 TBq, each placed in a circular array in a heavily shielded assembly. The device aims gamma radiation through a target point in the patient's brain. The patient wears a specialized helmet that is surgically fixed to the skull, so that the brain tumor remains stationary at the target point of the gamma rays. An ablative dose of radiation is thereby sent through the tumor in one treatment session, while surrounding brain tissues are relatively spared.

The apparatus in which the patient is inserted is shown in Fig. 4.6, left.

The risks of Gamma Knife radio surgery treatment are very low, being the complications mainly related to the condition being treated [34] [35]: limits to its use are given by the size of the lesion to treat.

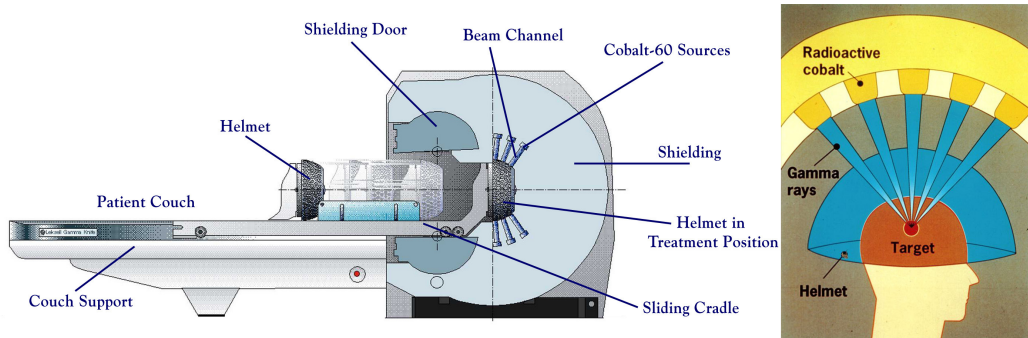


Figure 4.6. Scheme of the apparatus used for the GammaKnife technique.

4.1.2 Radio Guided Surgery applicability on Cerebral Tumors

As discussed several times in this Thesis, the main field of application of the probe under development is brain surgery.

In this Section, after an analysis of the imaging techniques commonly used when dealing with cerebral tumors, a study based on such images will be presented, with the aim to evaluate the applicability of the β^- -RGS technique in this field.

4.1.2.1 Functional imaging in brain tumors

Among the several imaging techniques available today, when dealing with cerebral cancers the golden standard is represented by CT and NMR. These techniques show in fact a very good resolution in detecting brain tumor, and in particular NMR is able to distinguish diseased cells from healthy ones with great clarity (Fig. 4.2).

Positron Emission Tomography (mainly with ^{18}F -FDG) is commonly used when functional information about the tumor is required, for example in lung, stomach and renal cancers.

On the contrary, PET is not commonly suitable for using in cerebral tumors, due to the efficacy of standard techniques and the need of more specific radio tracers with respect to ^{18}F -FDG, that being richly absorbed by the normal brain tissue implies an unfavorable tumor to background ratio.

However, in some selected cases of brain cancer, in addition to CT and/or NMR also PET imaging is used. It is the case for example in which a tumor must be present (following the detection for example of blood markers, or due to the collected symptoms) but is not revealed by standard imaging techniques, or cases in which the lesion is located in particular zones (e.g. near the bone) and are thus difficult to delineate precisely.

In the case of Meningiomas, the most commonly used radio tracer is DOTA-D-Phe1-Tyr3-octreotide (DOTATOC). This molecule is a Somatostatine analogue, as discussed in Sec. 1.3.2.1, and owes its efficacy to the high incidence of somatostatin receptors showed by meningiomas [36].

The radio tracer for PET imaging is hence obtained by bounding an atom of ^{68}Ga to this molecule, and is thus called ^{68}Ga -DOTATOC. Gallium 68 in fact decays β^+ in Zn with an half life of $t_{\frac{1}{2}} = 1.13$ h, which gives the possibility to take the scan about 2 hours after the injection.

It has to be noted that in view of a possible application in Radio Guide Surgery with β^- emission, another isotope must be used in place of ^{68}Ga , as discussed in Sec. 1.3.2.2, for example ^{90}Y . However, it is commonly accepted that the uptake and the pharmacokinetics of a radiopharmaceutical is totally due to the ligand molecule, being reasonably uniform among different radioactive isotopes.

The uptake of this molecule by meningiomas is so favorable in terms of TNR (Tumor to Non Tumor Ratio) that DOTATOC is used also for Peptide Receptor Radio Therapy (Sec. 1.3.2.1) for these tumors, where high specificity is fundamental in order to avoid severe damages to healthy organs.

For these reasons, this radio tracer represents a good candidate in view of a possible application or Radio Guided Surgery with β^- emitters in cerebral tumors.

However, Meningioma surgery is not a field that could profit much of such a technique. In fact, as seen in Sec. 4.1.1.1, this is mainly a benign tumor, that is relatively easy to resect during surgery due to its clear and differentiated margins.

On the contrary, the *killer application* of this technique could be represented by Gliomas, that, as seen in Sec. 4.1.1.1, are the most malignant cerebral tumors, characterized by unclear margins, often infiltrating deeply in the surrounding tissues, resulting in a hardly complete resection, with following high recurrence rate and very poor survival.

Regrettably, gliomas show a much weaker uptake to DOTATOC than meningiomas. PET imaging, despite being sometimes anyhow used due to lack of alternatives, gives images that are much less contrasted and clearly readable compared to the ones of meningiomas, as showed in Fig. 4.7.

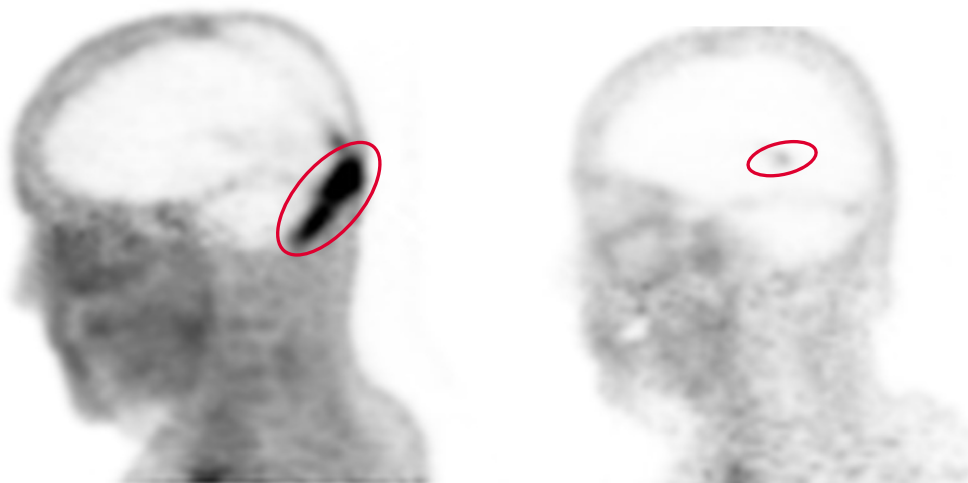


Figure 4.7. Comparison of PET images obtained with ^{68}Ga -DOTATOC in case of Meningioma (left) and Glioma (right). The red ellipse highlights the tumor. The difference in term of visual contrast reflects the one in TNR.

The TNR results to be so poor that PRRT is not a viable therapy for gliomas.

However, thanks to the peculiar and innovative characteristics of β^- Radio Guided Surgery described in Sec. 1.3.2, in particular its specificity and spatial resolution, even a reduced TNR, of the order of 4, can be sufficient to this technique.

4.1.2.2 Uptake Study

To this aim, to precisely evaluate the uptake of DOTATOC by meningiomas and gliomas, a statistic study was then performed on PET images of patient with cerebral tumors, in order to assess the feasibility of β^- -RGS [37].

Patient cohort

The patient cohort was composed by 23 patients from *Istituto Europeo di Oncologia* (IEO), Milan. In particular, the sample included:

- 11 patients affected by meningioma;
- 12 patients affected by glioma.

The characteristics of the formers are showed in Tab. 4.3, together with the number of lesions per patient, its weight, the injected activity and the diagnosis. All the patients therein reported but the first two have been previously treated (either by surgery, radiotherapy, PRRT or gamma knife).

Patient	N° of lesions	W (kg)	A (MBq)	Diagnosis
M01	1	63	220	atypical meningioma (gr II)
M02	1	80	260	spheno-petro-clical meningioma
M03	3	95	305	recurrent atypical meningioma
M04	1	48	200	recurrent meningioma
M05	3	57	130	recurrent meningioma
M06	2	90	145	malignant meningioma
M07	1	74	237	secondary meningioma
M08	3	105	223	cervical meningioma
M09	2	48	145	recurrent meningioma
M10	2	70	240	atypical extracranial meningioma
M11	1	75	220	atypical meningioma (gr II)

Table 4.3. Characteristics of the sample of meningioma patients, showing for each one its number of lesions, weight (W), the injected activity (A) and the diagnosis.

All the 12 considered patients affected by glioma have been previously treated (either by surgery, radiotherapy, PRRT or chemotherapy), and their characteristics are showed in Tab. 4.4

Uptake Evaluation Method

To evaluate the uptake of the tracer in the tissues, using the software AMIDE [38], several ROIs (*Regions Of Interest*) have been drawn on the dicom PET images slice by slice, to cover as much as possible the tumoral zone. Two different approaches were followed in case of meningioma or glioma.

For meningioma, in the event of multiple lesions, each one has been considered separately, and the ROIs were drawn to follow their contour, taking care not to include healthy tissue nearby.

Patient	W (kg)	A (MBq)	Diagnosis
GB01	97	246	glioblastoma
GB02	68	223	glioblastoma multiforme
GB03	80	152	glioblastoma
GB04	93	198	glioblastoma
GB05	90	192	glioblastoma
GB06	60	185	glioblastoma
GB07	63	194	glioblastoma
GB08	70	266	glioblastoma
GB09	85	255	glioblastoma multiforme
GB10	80	224	olygodendroglioma
GB11	70	234	high grade glioma
GB12	15	38	glioma

Table 4.4. Characteristics of the sample of glioma patients, showing for each one its weight (W), the injected activity (A) and the diagnosis.

For glioma, the ROIs have been drawn including the central zone of necrosis often present inside the tumor, because the low TNR makes it difficult to exclude the presence of diseased tissue therein.

An example of ROI for both cases is shown in Fig. 4.8.



Figure 4.8. ROI (red line) drawn on meningioma (left), glioma (center) and healthy tissue (right)

For each ROI built (on N_s slices), the “statistic” panel of AMIDE gives the following values:

- the *mean value* $\mu_i (i = 1, \dots, N_s)$, in Bq/ml of the uptake of the radiopharmaceutical;
- the *standard deviation* $\sigma_i (i = 1, \dots, N_s)$;
- the *number of effective voxels contained in the ROI* $N_i (i = 1, \dots, N_s)$.

Starting from these values, for each patient and for each lesion the error on the mean uptake within the ROIs was obtained as

$$\sigma_i = \frac{\sigma_n}{\sqrt{N_i}}. \quad (4.1)$$

To obtain the value of the specific activity of DOTATOC for the whole lesion the weighted mean was calculated:

$$\mu = \frac{\sum_i \frac{\mu_i}{\sigma_i^2}}{\sum_i \frac{1}{\sigma_i^2}}, \quad (4.2)$$

and the associated error:

$$\sigma_\mu = \frac{1}{\sqrt{\sum_i \frac{1}{\sigma_i^2}}}. \quad (4.3)$$

An example of the specific activity μ_i of a meningioma slice by slice is showed in Fig. 4.9, top. The showed structures are caused by the shape of the tumor in each slice, while the border effect is due to the PET resolution.

Similarly, Fig. 4.9, bottom shows the specific activity of a glioma slice by slice.

Despite being a good parameter to evaluate a single patient's uptake, the activity does not permit to compare the uptakes among different patients, where differences in weight, injected dose and exam times occur. To this aim, the *Standardized Uptake Value* (SUV) must be used. The SUV is a parameter that gives the ratio between the activity of the selected region and the one that would be measured if all the injected dose would have been diffused uniformly for the whole body.

Mathematically, it is obtained by normalizing the measured μ to the injected activity per mass unit, once corrected for the physical decay from the injection time:

$$SUV = \frac{\mu}{\frac{A_0 e^{0.693(-T_{PET}/T_{Ga}^{1/2})}}{P}}, \quad (4.4)$$

where A_0 is the activity injected to the patient, T_{PET} the time interval between the administration of the radiopharmaceutical and the exam, $T_{Ga}^{1/2}$ is the half life of ^{68}Ga (68 min) and P is the weight of the patient.

As far as the healthy tissue is concerned, several ROIs on several slices of the scan were chosen. Since the β^- radiation is local, the ROIs were chosen, by means of the information from the CT, close to the tumor margins, as shown in Fig. 4.8 (right). In this case a weighted average was used to evaluate μ_{NT} , σ_{NT} and the corresponding SUV_{NT} .

The TNR was thus estimated as the ratio between SUV_T and SUV_{NT} :

$$TNR = \frac{SUV_{Tumor}}{SUV_{NonTumor}}. \quad (4.5)$$

Results

Meningioma

All the meningiomas showed good uptake of DOTATOC, despite non uniform among the several slices. This suggests that the radio tracer is absorbed not equally inside the tumor volume, probably because of the effects of the previous therapy, being the great majority of the studied cases recurrent or however already treated lesions, in addition to a normal variation in the molecule uptake.

The mean specific activity μ of all the tumors in patients affected by meningioma in the sample is reported in Fig. 4.10, top.

All the values are contained between a maximal uptake of 13 kBq/mL and a minimum of 1.6 kBq/mL. Only one lesion has an uptake significantly greater than the other, probably as a result of a very wide tumor. Different lesions of the same patient, showed with the same color, show different uptake, probably being some primary and some other secondary tumors.

About 70% of the tumors has a SUV greater than 2 g/mL (Tab. 4.5 and Fig. 4.10, middle): this means that injecting an activity of 3 MBq/kg would produce a specific activity greater than 6 kBq/mL.

The TNR for meningiomas is always greater than 10 (Fig. 4.10, bottom), with one case of huge value due to an anomalous uptake in the healthy tissue.

Paziente	N lesioni	$SUV_{lesione}$ (g/ml)	SUV_{fondo} (g/ml)	Diagnosi
M01	1	2.174	0.069	meningioma atipico (2 grado)
M02	1	1.139	0.093	meningioma sfeno-petro-clivale
M03	3	2.229	0.126	recidiva di meningioma atipico
		3.384	0.126	
		5.228	0.126	
M04	1	6.069	0.162	meningioma recidivante
M05	3	4.489	0.161	meningioma recidivante
		3.549	0.161	
		3.858	0.161	
M06	2	7.421	0.066	meningioma maligno
M06		3.843	0.066	
M07	1	3.362	0.141	meningioma (lesione secondaria)
M08	3	3.755	0.131	meningioma cervicale e recidive
		2.048	0.131	
		1.941	0.131	
M09	2	0.852	0.085	meningioma e recidive
		0.970	0.085	
M10	2	0.973	0.045	meningioma atipico extracranico
		0.834	0.045	
M11	1	0.755	0.137	meningioma atipico (2 grado)

Table 4.5. SUV for both tumor and background in case of meningioma. The malignant meningioma shows the greater SUV.

Glioma

Despite being significantly weaker than in meningiomas, the uptake in gliomas is almost always sufficient to make the tumor visible enough at the PET.

The mean specific activity was found to range from a minimum of 0.2 kBq/mL to a maximum of 1.7 kBq/mL (Fig. 4.11, top).

Fig. 4.11, middle, and Tab. 4.6 show the SUV for gliomas. The found values are

lower than the one for meningiomas, as expected. About 60 % of the lesions show a SUV of about 0.2 g/mL, that means that injecting an activity of 3 MBq/kg would produce a specific activity of about 0.6 kBq/mL.

Paziente	$SUV_{lesione}$ (g/ml)	SUV_{fondo} (g/ml)	Diagnosi
GB01	1.097	0.052	glioblastoma
GB02	0.321	0.041	glioblastoma multiforme
GB03	0.604	0.068	glioblastoma
GB04	1.438	0.133	glioblastoma
GB05	0.251	0.072	glioblastoma
GB06	0.250	0.059	glioblastoma
GB07	0.274	0.062	glioblastoma
GB08	0.121	0.028	glioblastoma
GB09	0.219	0.038	glioblastoma multiforme
GL10	0.101	0.058	oligodendroglioma
GL11	0.284	0.073	glioma di alto grado
GL12	0.283	0.072	glioma pontino

Table 4.6. SUV for both tumor and background in case of glioma.

Also TNR values are smaller than the ones for meningiomas, as showed in Fig. 4.11, bottom: with only one exception TNR is always greater than 4, greater than 8 in one third of the cases.

It has to be noted that all the results regarding gliomas are quite conservative: as described above and in Fig. 4.8, in the ROIs used to study gliomas clearer areas were included due to the impossibility to assess the benign nature of such a zones with such a low TNR. This obviously results in a reduction of the estimated uptake within the lesion, with a consequent less favorable TNR.

Discussion The method described here permitted to study the uptake of DOTA-TOC in meningiomas and gliomas.

Summarizing, in 8 patients out of 11 affected by meningioma, after the administration of about 200 MBq of DOTATOC, the mean specific activity for the tumor, about 1 h after the injection, was found to be greater than 3 kBq/mL for 1 atypical meningioma, 4 meningiomas with recurrences and 1 malignant meningioma.

The mean specific activity is lower than 3 kBq/mL in 2 cases of atypical meningioma and in one patient not subjected to previous therapy. The only considered case of malignant meningioma (that represent, as showed in Sec. 4.1.1.1 about the 8% of the cases showed an uptake greater than the mean one.

In the case of gliomas, the uptake is definitely lower, and for 10 patients out of 12 has a mean value of about 0.4 kBq/mL, with only 2 cases with specific activity greater than 1.5 kBq/mL.

To convert this obtained information into clues regarding the feasibility of the β^- RGS further studies are required, that will be detailed in Chapter 5.

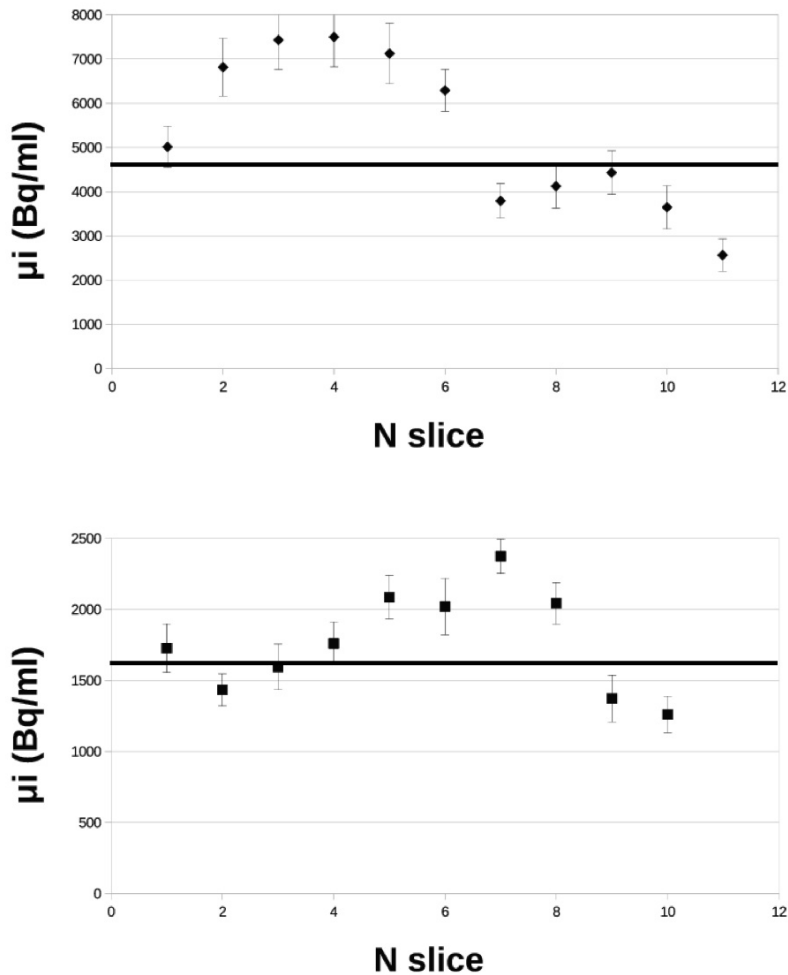


Figure 4.9. Example of DOTATOC uptake in a case of meningioma (M07, lesion 1) (top) and glioma (GB04) (bottom), as a function of the image slice. The line represents the mean value obtained by means of the weighted mean described in 4.2.

Meningioma: Dose = 223 MBq, $\chi^2/DOF = 7.32$, $\mu = 4791$ Bq/mL, $\sigma_\mu = 371.1$ Bq/mL.

Glioma: Dose = 198 MBq, $\chi^2/DOF = 7.3$, $\mu = 1661$ Bq/mL, $\sigma_\mu = 200$ Bq/mL.

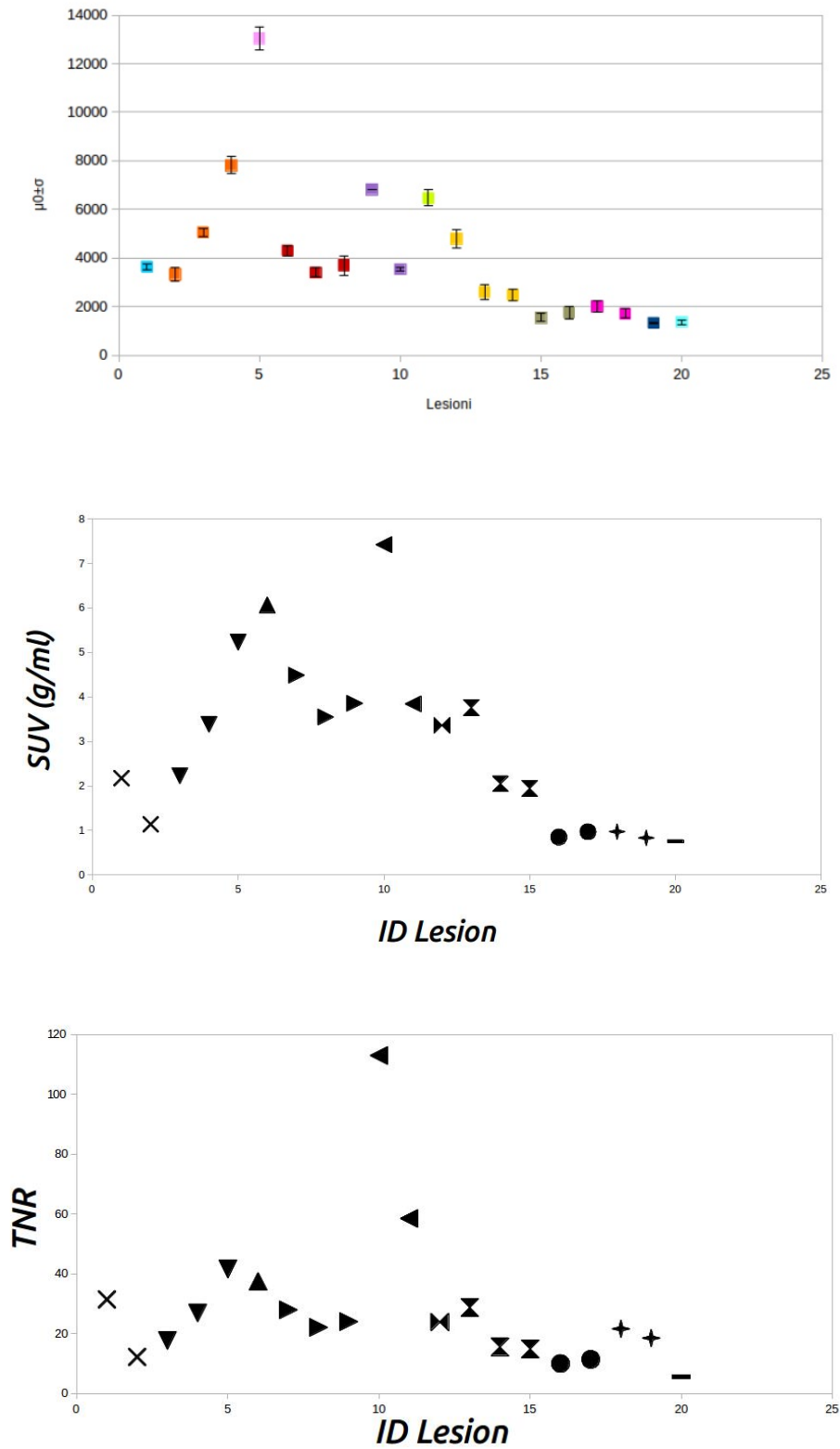


Figure 4.10. Results of the uptake study of the lesions in patients affected by meningioma: specific activity (top), SUV (middle) and TNR (bottom). Points of the same color or shape represent multiple lesions of the same patient. All the lesions but the first two have previously been treated in some way.

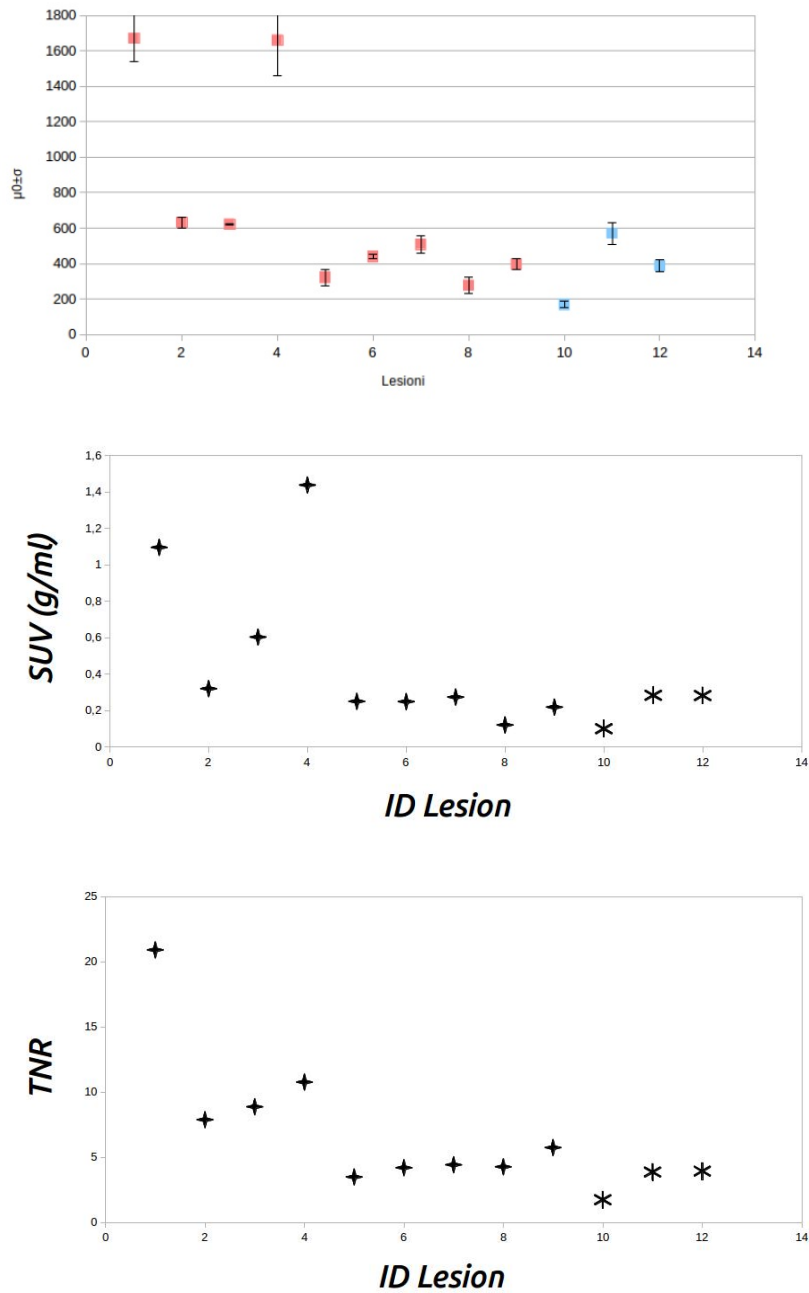


Figure 4.11. Results of the uptake study of the lesions in patients affected by glioma: specific activity (top) expressed in Bq/ml, SUV (middle) and TNR (bottom). All the lesions but the first two have previously been treated in some way.

4.2 Neuroendocrine Tumors surgery

Beside the possible application in the field of brain surgery, there is plenty of other cases in which β^- -RGS could give remarkable aid to the surgeon.

In this Section, Neuroendocrine Tumors (NETs) will be discussed, starting from a brief overview of their characteristics and proceeding with an applicability study of the β^- -RGS technique exploiting SPECT images of patients showing NETs.

4.2.1 Neuroendocrine Tumors: origin and therapy

Neuro Endocrine Tumors are neoplasms that arise from cells of the endocrine and nervous system. Following this definition, that is focused on the histological kind of the originating cells rather than the tumors' district, NET can occur in the entire body (p.e. lung, kidney, brain), even if the most common localization is the intestine.

The important thing is that despite having such different localizations throughout the body, due to their common origin they share numerous features, such as a similar looking, producing the same molecules (e.g. hormones) and showing similar receptors.

Neuroendocrine cells are cells that receive neuronal input (neurotransmitters released by nerve cells or neurosecretory cells) and, as a consequence of this input, release message molecules (hormones) to the blood. In such a way they play a fundamental role in the so called "neuroendocrine integration" between the nervous system and the endocrine system.

These cells are present not only in endocrine glands throughout the body that produce hormones, but also diffused in all body tissues.

In *Epidemiology*, there are two main quantities used to describe the diffusion of a certain disease: *Incidence* and *Prevalence*.

- The *Incidence* rate is the number of new cases per population at risk in a given time period, and thus gives a measure on a statistical basis the risk to develop the disease in a certain period of time.
- The *Prevalence* gives the number of cases present in a population at a given time, in a sort of "integral" of the incidence rate.

Neuroendocrine tumors are rare, having an annual incidence of approximately 2.5 – 5 per 100000 people, of which two thirds are carcinoid tumors and one third other NETs. The prevalence has been estimated as 35 per 100000 [39] [40] [41].

This means that despite being rare, they have a remarkable impact on the public health system. In fact, their relatively slow progression results in a higher prevalence, that means a consistent number of patients affected by them have to be treated constantly.

Moreover, in general NETs are diagnosed at a relatively late stage, with metastatic spread present at the time of diagnosis in the majority of patients. For such a reason, often curative surgery is no longer an option, as well as external radiotherapy, due to the number of disseminated lesions. Moreover, the response rate of chemotherapy is only at the level of 20 – 35% [42], being effective in a minority of patients with poorly differentiated NETs, and completely ineffective in the majority of well- differentiated NETs.

The number of possible treatments is therefore drastically reduced.

In this context, *Peptide Receptor Radionuclide Therapy* (PRRT) using radiolabeled somatostatin (SST) analogs has proven to be an effective therapeutic option for NET patients with metastasized disease, as it allows targeted delivery of therapeutic radionuclides to tumor cells [43].

In this therapy, somatostatine analogues are bound with a radioactive isotope, and their preferential uptake by tumor cells is exploited to reach and damage them by means of the emitted particle, usually an high dose β^- radiation.

The most common somatostatine analogues used for PRRT are DOTATE and DOTATOC, coupled either with ^{90}Y (pure β^- decay, $T_{1/2} = 64.1$ h, $E_{MAX} = 2.3$ MeV) or ^{177}Lu (β^- decay, $T_{1/2} = 6.7$ d, $E_{MAX} = 0.5$ MeV, with a 6% contamination of gamma emission with $E = 113$ keV).

4.2.2 Feasibility study of β^- -RGS in Neuroendocrine Tumors

Following a path similar to the one undergone for cerebral tumors is Sec. 4.1, it is possible to use the wide existing literature regarding ^{90}Y -DOTATOC uptake in Neuroendocrine tumors to evaluate the feasibility of Radio Guided Surgery with β^- emission in this kind of cancers.

However, the existing literature gives plenty of information about the DOTATOC uptake in several organs such as kidney, liver and spleen, but do not focus on the uptake of the tumor itself. This is due to the fact that the *conditio sine qua non* for undergoing PRRT is the expression of the needed receptors by the tumors, condition evaluated by means of a preliminary PET exam with ^{68}Ga -DOTATOC radiopharmaceutical.

Once established that the tumor does express such receptors and thus shows uptake to the molecule, the real problem shifts to the dose given to healthy vital organs. In particular, is the renal toxicity the adverse side effect to keep under control in the view of a balance between costs and benefits for the outcome of the patient.

In fact, in Peptide Receptor Radio Therapy the activity to be injected to the patient is calculated on the basis of the dose absorbed by the kidney, that is thus a fundamental value to compute.

This results in an abundance of studies regarding the uptake in vital organs at several times after the injection.

The missing point to evaluate the feasibility of β^- RGS is the precise and quantitative study of this uptake in the tumor.

In other words, there is clear evidence that NETs sufficiently express receptors for DOTATOC to be candidates to RGS, but we still have no information regarding the exact values of the TNR, neither we know anything about the time evolution of this ratios, to know which would be the best time to perform RGS after injection.

For this reason, I carried out a statistical study on DICOM images of patients affected by Neuroendocrine tumors at *Arcispedale Santa Maria Nuova*, in Reggio Emilia.

4.2.2.1 Patient Cohort

The patient cohort was composed by 16 patients affected by Neuroendocrine Tumors in different localizations, mainly within the abdomen.

These are patients for which surgery is no longer an option, either for the number or localization or for the recurrent nature of the lesions. After their enrollment for PRRT, following the preliminary PET exam, they were injected with a first standard ^{177}Lu -DOTATOC dose (from guidelines, function of the patient's weight). During this first treatment, that requires the patient to be hospitalized for few days due to its radioactivity ($T_{1/2}^{\text{Lu}} = 6.7$ d), a dosimetric study is normally carried out.

Exploiting the γ emission of ^{177}Lu , *Single Photons Emission Computed Tomography* (SPECT) images are acquired after 0.5, 4, 20, 40 and 70 h post injection. These data allows the medical physicists to evaluate the dose absorbed by the various organs, and the optimal dose to be injected in the following treatments is then calculated.

An example of a SPECT/CT image from one of the analyzed patients is shown in Fig. 4.12.



Figure 4.12. Example of a SPECT/CT image of one patient from the cohort, in this case showing physiological uptake in the kidneys and the spleen and an anomalous probably pathological uptake at the top of the liver. The good spatial information is provided by CT (grayscale), while the functional one is given by SPECT (red scale).

4.2.2.2 Analysis Method

For each patient, I used these DICOM images to evaluate the uptake of both normal organs and tumors at each time interval, with the aim to build a profile of this uptake as a function of the time from the injection.

The analysis was carried out by means of XXXX, a software that comes together with the imaging machines by Siemens, and which is able to both process the raw data and analyze them.

For each patient and for each acquisition, all the slices were scanned, and 2 lesions were identified, together with right kidney, spleen, liver and a zone behind the spinal column to use as “surely healthy” reference tissue.

For each of these, a ROI was built using the “isocontour” tool provided by the software. This is a tool that creates a regions containing only the entire pixels which value is in a defined range. In particular, in the case used, the range was defined in percentage with respect to the maximum value in a preselected region: the threshold was fixed to 60% in case of tumors, and was variate between 50 and 60% in case of normal organs.

Being this study devoted to understand the physiological behavior of Neuroendocrine tumors regarding DOTATOC uptake, and not experimental issues regarding the hypothetical use of the probe, a particular approach was followed:

- The ROIs have been built as much homogenous and small as possible. The idea in a certain sense is to imitate a “biopsy”, in which we pick a small region from the inner of the organ or tumor, avoiding problems and uncertainties linked to the borders. On the other hand, the ROI must be large enough for the statistic to be credible, so in general volumes of few cm^3 were used (being the voxel volume $4.7 \times 4.7 \times 4.7 \text{ mm}^3$).
- For the diseased tissue, the zone showing the higher uptake in the lesion area was selected. This was done in order to be sure to be selecting only tumoral tissue, and not for example necrosis areas.
- For the various organs, healthy zones were selected, even in cases in which metastasis were therein present. This was done because we are interested in the behavior of the tumor with respect to the healthy organs, not the metastasis.

An example of the so built ROIs is showed in Fig. 4.13.

For each so drawn ROI, the following values were obtained:

- Mean value;
- ROI volume;
- Standard deviation, which has been divided by the number of considered voxel to obtain the error on the mean value.

All these extracted values were then manually corrected for the physical decay of ^{177}Lu with respect to the time of injection, to permit the comparison between uptake at different times.

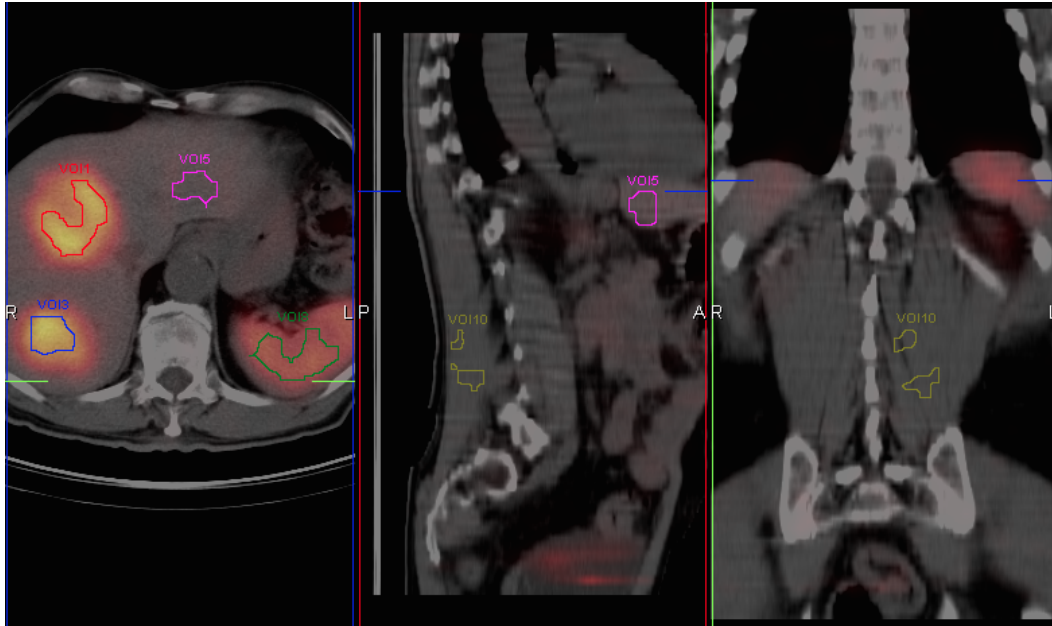


Figure 4.13. Example of ROIs built on a SPECT/CT image using the isocontour tool in the case of a Neuroendocrine tumor in the liver. It is possible to identify the ROIs of the two lesions (red and blue lines), the health liver (violet line), the spleen (green line) and the healthy tissue (yellow line).

It has to be remarked that the value given by SPECT images, and thus obtained from the statistics on the ROI, is not the real activity value of the voxel, as it happens in the case of PET images.

In fact, the information is given in terms of “number of counts” in the detector originating from that voxel. To convert this value in activity concentration (Bq/mL), a dedicated calibration procedure is needed, scanning with the SPECT apparatus several phantoms of defined shape and activity.

This is made necessary mainly by two effects, that are the non linear response of the detector for high activities (when saturation occurs), and the so called “*partial volume effect*”, that takes into account the variation of the read counts due to inclusion of partial voxels of different activities in the considered region.

However, in the present preliminary study, I used directly the number of counts as the comparison parameter. In fact, as explained above, the ROIs were selected in such a fashion to be all of the same order of magnitude in volume. Moreover, using the “isocontour” tool and thus selecting only entire pixels within the ROI the “partial volume effect” can be ignored. Moreover, not considering this effect results in an underestimation of the real uptake, thus resulting in conservative conclusions of the present study.

Lastly, not taking into account the saturation occurring at high activity levels (thus usually in the tumor), we obtain conservative values: we are in fact underestimating the tumor uptake, and thus the TNR.

Nonetheless, a complete analysis would be certainly desirable, and will be carried out in the near future, when this preliminary one will have put the basis for a complete and comprehensive work.

4.2.2.3 Results

Fig. 4.14 shows an example of the obtained results in terms of counts from various organs and lesions in the case of a liver Neuroendocrine Tumor (the same patient showed in Fig. 4.13). The tumor clearly shows an accumulation of the amount of radiopharmaceutical in the first hours after the injection, reaching a maximum at about one day post injection. On the contrary, all the healthy organs show a “clearance” behavior, with the sole partial exception of the spleen, that for its physiological role and nature has a greater retention time.

Fig. 4.15 shows an example of TNRs obtained from the data in Fig. 4.14. A general conclusion that can be drawn from this single case is that the most favorable TNR is found about 20 – 30 h post injection.

The trend showed by the tumor in Fig. 4.14 is basically found to be common among all the patients.

However, the uptake of various organs was found to be quiet different from one patient to another. For example, regarding Kidney, two main behaviors were found, as shown in Fig. 4.16.

This is in good agreement with several studies available in the specific literature (Fig. 4.17, [44]), and is a consequence of the variability in the uptake due to various risk factors and characteristics of the patient (other pathologies, ongoing treatments and so on).

Fig. 4.18 shows the activity as a function of time for all the lesions, livers, spleens and kidneys of the sample.

The Tumor to Non Tumor Ratios obtained from these data are showed in Fig. 4.19, always respecting the previous division in two groups.

4.2.2.4 Discussion

The study presented in this Section showed that all the analyzed Neuroendocrine Tumors shown high uptake of DOTATOC. Moreover, this uptake generally increases in the first hours after the injection, reaching a maximum after about 24 h.

As far as healthy organs are concerned, they too show considerable uptake of the radiopharmaceutical. Their pharmacokinetic, however, was found to be, in agreement with the existing literature, significantly variable among patient.

The so found TNR suggest that the most favorable moment to undergo β^- -RGS is about 24 h post injection. This is in fact the moment in which the TNR is the maximum, allowing to reach the best spatial resolution, or on the other hand to lower the injected activity.

This kind of information has a fundamental role in developing an optimized protocol for Radio Guided Surgery with β^- emitter.

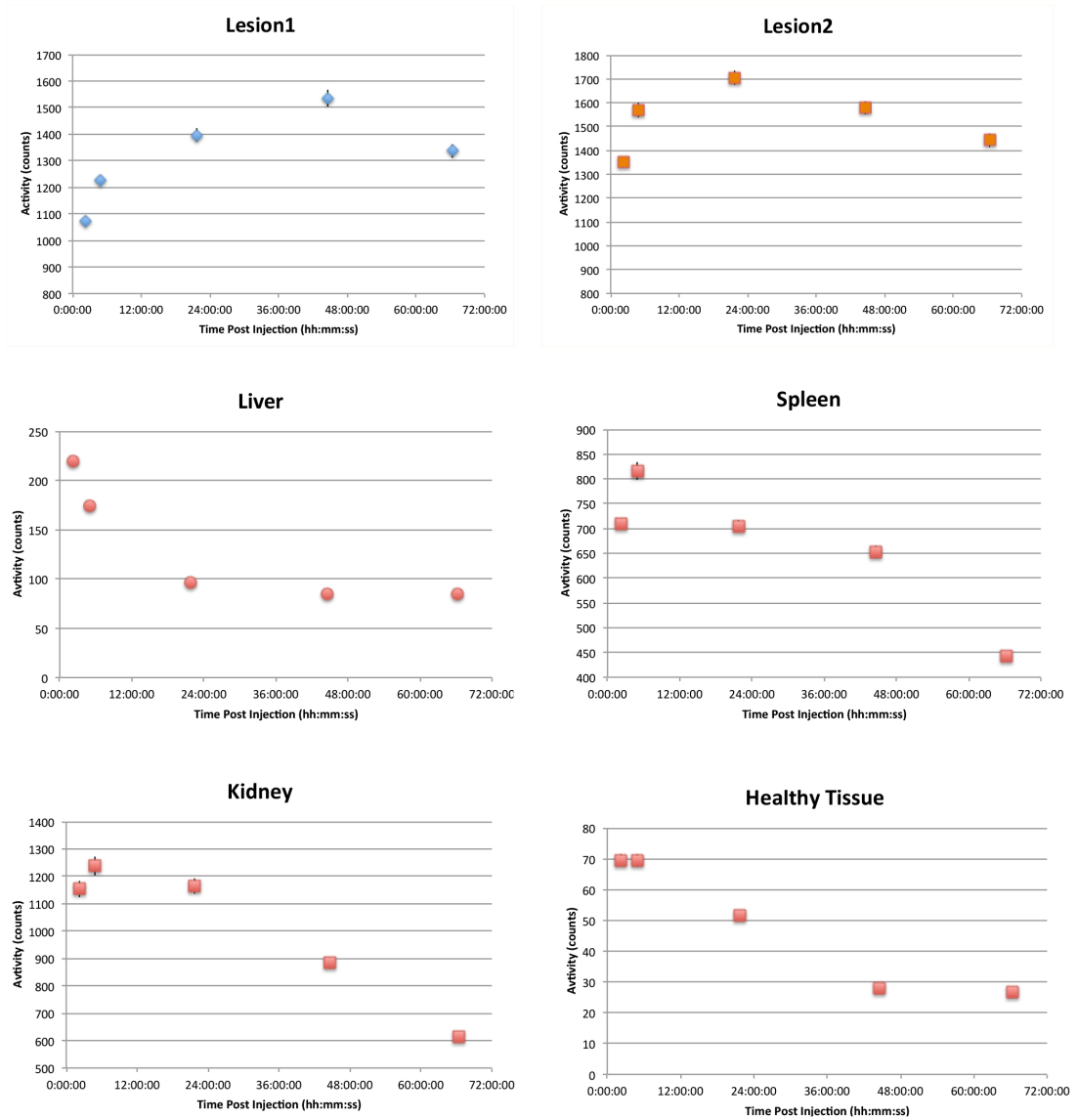


Figure 4.14. Example of results obtained in terms of counts from lesions and organs in a liver Neuroendocrine Tumor (Fig. 4.13). It is evident how tumor and healthy organs show different behavior. In fact, the tumor tend to accumulate the radiopharmaceutical, reaching its maximum in uptake at about 24 h post injection. On the contrary, healthy organs show a “clearance” conduct, with the exception of the spleen, that acts as a “tank” of injected substances.

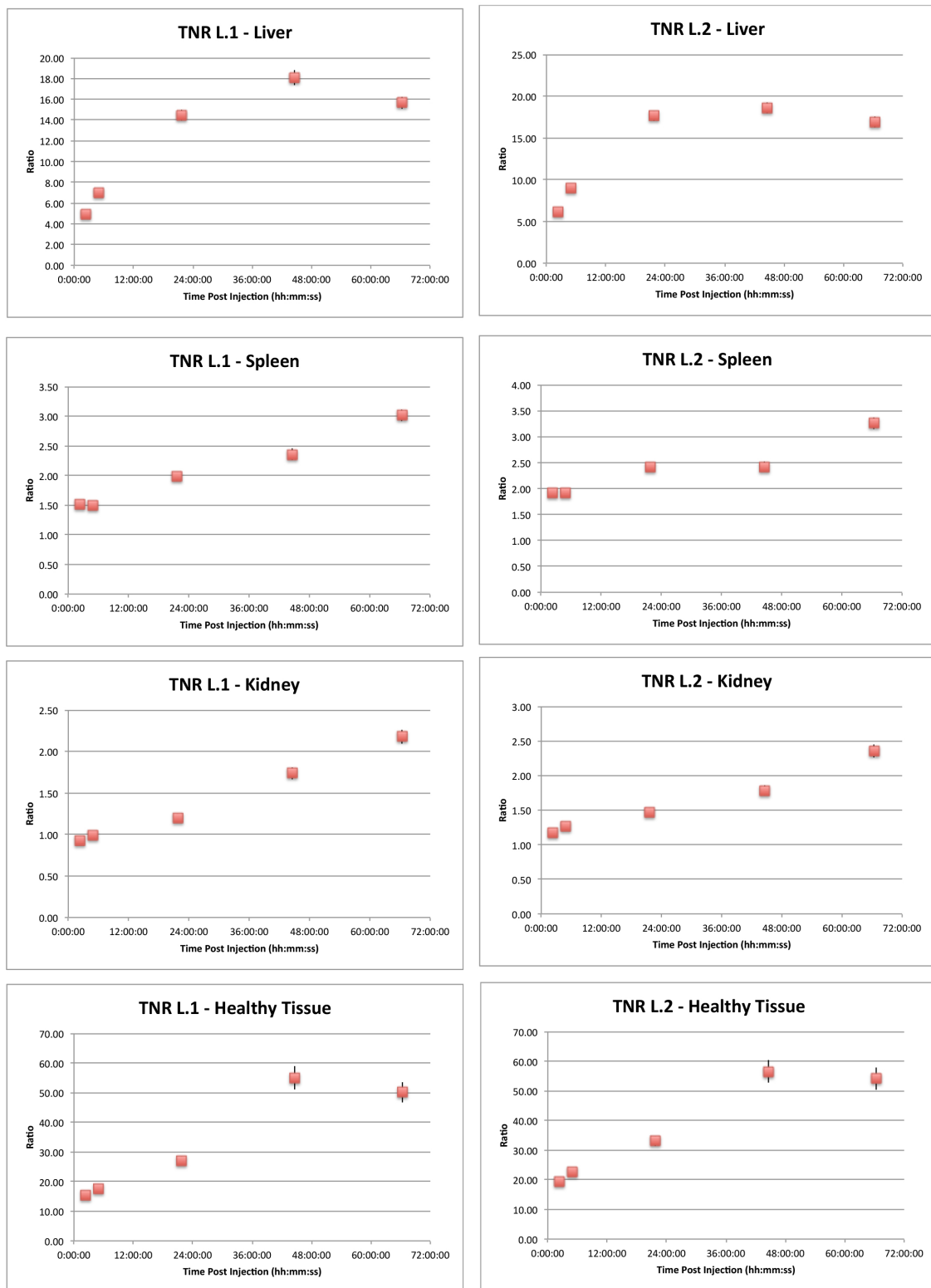


Figure 4.15. Example of TNR calculated from the data in Fig. 4.14, thus in the case of a liver Neuroendocrine Tumor (Fig. 4.13).

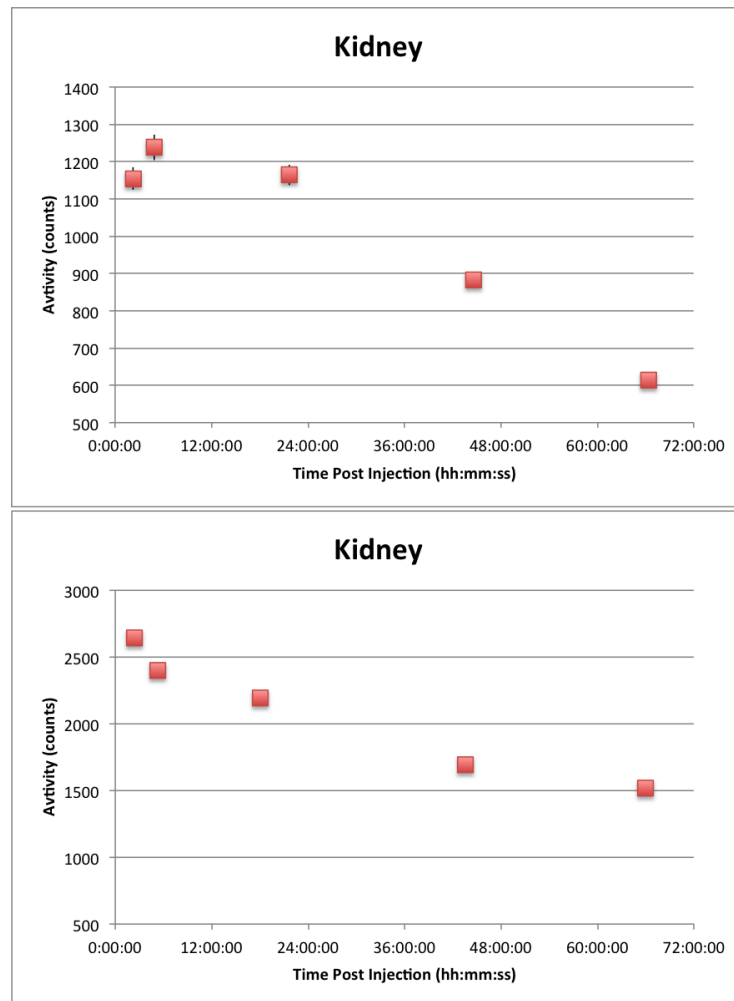


Figure 4.16. Two cases of renal uptake of the radiopharmaceutical representative of the two populations found: on showing clearance (top), and the other showing accumulation (bottom).

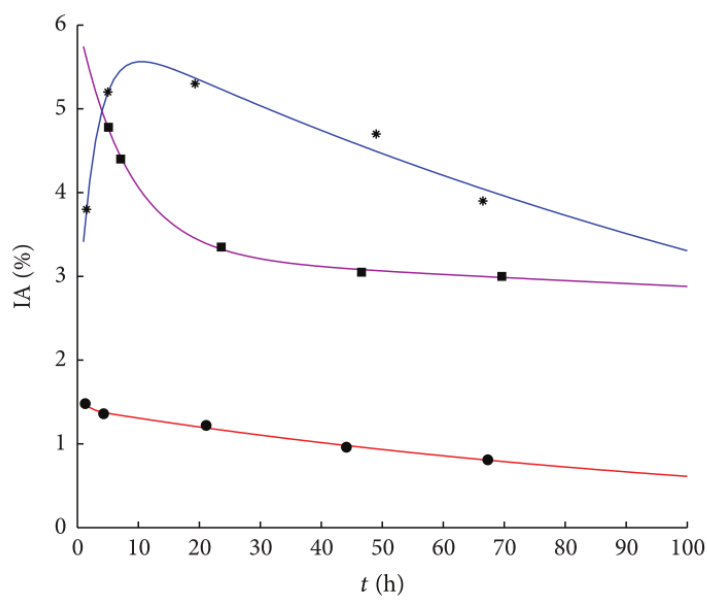


Figure 4.17. Examples of observed pharmacokinetic curves obtained for DOTATOC and DOTATATE: accumulation (blue line) and clearance (red and violet lines, according to the rapidity of the decrease) [44].

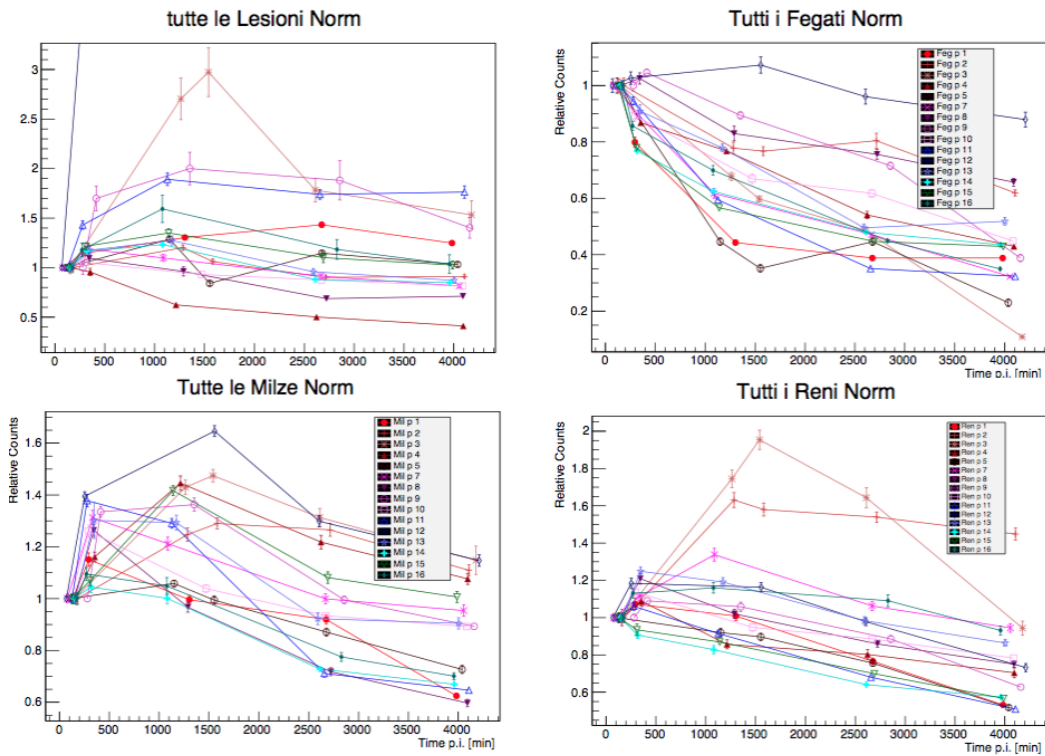


Figure 4.18. Activity (expressed in count number) as a function of the time post injection (expressed in minutes) for Lesion, Kidney, Spleen and Liver for the whole sample of patient. For visual clarity the points have been connected by lines and normalized to share the same starting value, allowing to compare the trends. Each marker shape and line color corresponds to a single patient through all the plots.

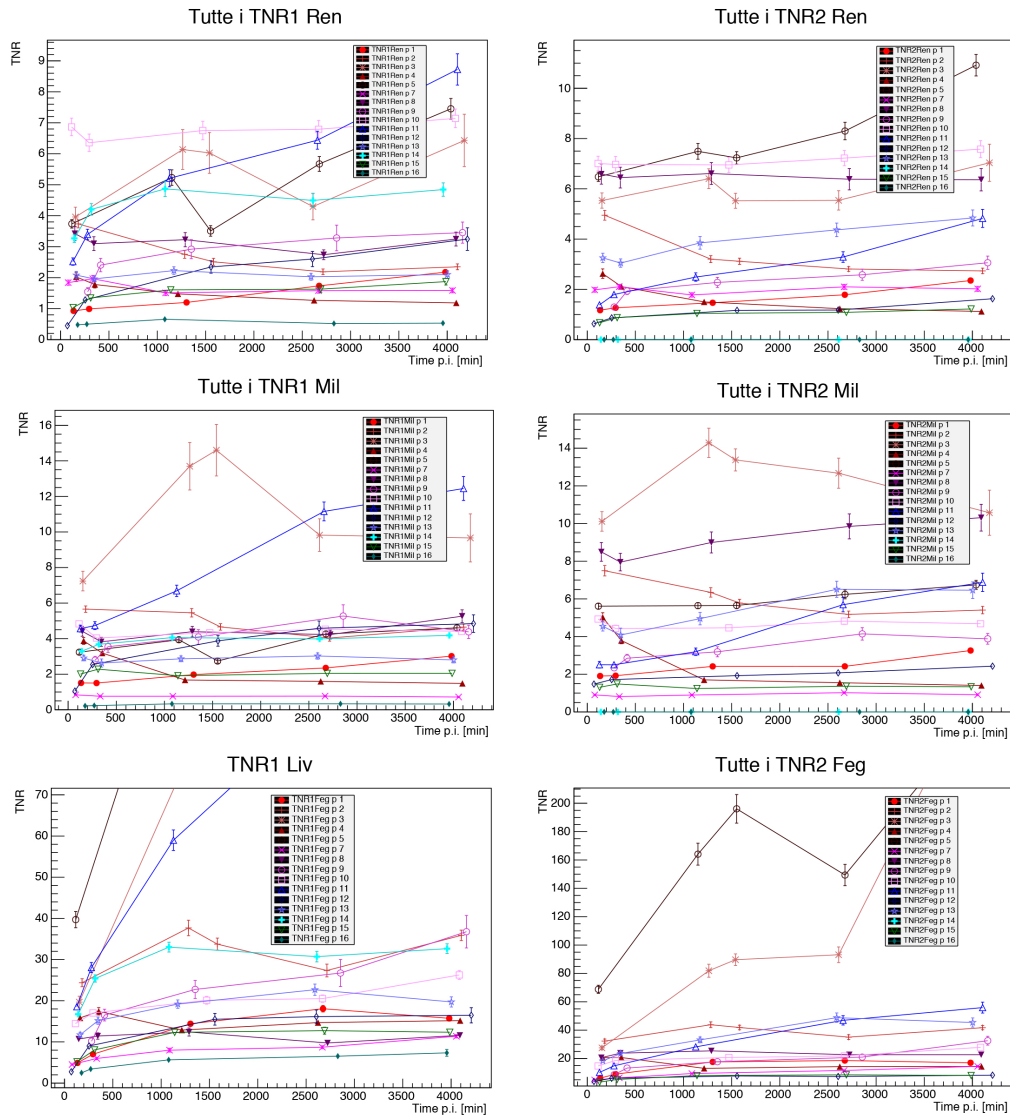


Figure 4.19. TNR for all the patients in the cohort with respect to Kidney, Spleen and Liver as a function of time post injection. Despite substantial variation between the patients, there is clear indication that the ratio reaches its most favorable value at about 24 h (1400 s) after the administration of the radiopharmaceutical.

Chapter 5

Evaluation of Probe Performances

In Chapter 1 the rationale of Radio Guided Surgery technique was presented, focusing on the importance of a complete tumor resection in order to maximize the efficacy of the treatment and thus improve the outcome of the patient. In particular, a novel technique or Radio Guided Surgery has been proposed, exploiting the use of β^- decay in place of the commonly used β^+ and γ decays, pointing out the advantages that characterize this approach, mainly its good spatial resolution and its high background rejection capabilities following the poorly penetrating nature of β^- radiation.

In Chapter 3, the development of a detector devoted to this application, named *probe*, was discussed. In particular, three prototypes of probe were presented (Sec. 3.2), and their optimization was described, taking advantage of both laboratory measurements and MC simulations.

In Chapter 4 the first possible medical applications of β^- -RGS were discussed, particularly focusing on the case of Brain Surgery (meningioma and glioma) and Neuroendocrine Tumors. Statistical studies based on imaging data were presented in both cases to evaluate the applicability of this technique in this field, concluding that both cases present characteristics suggesting the feasibility of this approach.

In this Chapter, further studies will be presented, in order to evaluate the expected performances of the probe in real application cases.

5.1 Developments in FLUKA

As seen in Chap. 2, FLUKA is a general purpose tool for calculations of particle transport and interactions with matter. Despite being born in the field of accelerator shielding, over the various new versions it gained a fundamental role in several applications, including medical physics.

5.1.1 PET import

As described in Sec. 2.2.1, FLUKA is able to import CT scans directly converting the DICOM files in geometrical bodies to be used in the simulation. This is a key feature

in medical applications, and FLUKA is indeed widely diffused within dosimetry studies and treatment planning for radiotherapy and hadrontherapy.

However, by default FLUKA does not support PET scans import. Despite being the files used of the same format as CT (DICOM *.dcm* files, one for each slice of the patient) there is a profound difference between the information stored therein in the two cases. In fact, while in CT scans for each pixel the Hounsfield value is given (see Sec. 2.2.1), in PET images the grey-scale value is related (via two conversion factors) to the radioactivity of the voxel volume, and is measured in Bq/mL.

For this reason, being an “activity map” rather than a physical one, there is no usefulness in importing it as geometry voxels.

However, PET provides information that can be considerably important for some applications.

For example, in the case of Radio Guided Surgery, being able to simulate the exact distribution of activity within the patient allows to test a probe prototype in a completely realistic environment, avoiding to take any hypothesis of uniformity of the concentration of radiopharmaceuticals in a certain zone of interest.

For these reasons, in my Thesis work I developed a work-around to import PET scans in FLUKA making them available as a proper “activity map”.

This is achieved in two consecutive steps.

First, the DICOM importer is used to generate starting from the *.dcm* files a USRBIN (*.bnn*). This is one of the available scoring detectors (see Sec. 2.4), and is basically a sort of three-dimensional histogram, in which at each spatial bin is assigned a value. This value is usually the energy deposited, a particle fluence, the equivalent dose and so on. In such a way, the PET scan is converted into a mesh in a standard FLUKA format.

The second step makes use of a *user routine* (see Sec. 2.3), which is a Fortran program that reads this USRBIN file interpreting it as a “probability map” according to which primary particles’ positions are generated. The other particles’ characteristics (kind, energy..) are then provided via the BEAM card. It is for example possible in this way, by selecting the apposite radioactive nuclide as particle, to obtain within the simulation the same exact situation of a patient injected with a radiopharmaceutical.

The result of this import process is showed in Fig.5.1.

Despite appearing a quite straightforward approach, there are some caveat to take into account.

First, the isotopes used for PET exams are different from the ones of interest in case of RGS (see Sec. 1.3.2). This implies that all this process relies on the assumption (normally accepted by nuclear physicians [45]) that the uptake of a certain radiopharmaceutical depends only on the carrier molecule, and not on the radioactive isotope. It is then reasonable to use PET images acquired with ^{68}Ga -DOTATOC to know the distribution of an eventual injection of ^{90}Y -DOTATOC. Moreover, the above described method used in FLUKA, using an “activity map”, makes it easy to change the emitted particle.

Secondly, in the PET DICOM files the activity is assumed to be uniform within the voxel, due to the scanning apparatus sensitivity. This means that the effective resolution is limited to the voxel one, usually of the order of $3 \times 3 \times 3 \text{ mm}^3$. Hence,

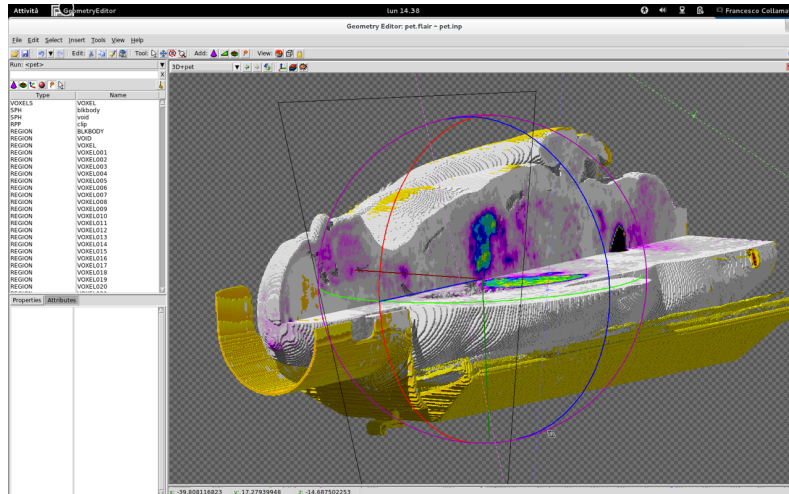


Figure 5.1. Result of the importation of PET (^{18}F -FDG) dicom files in FLUKA, superimposed with the aforesaid CT scan. To highlight internal structures the patient's volume has been clipped by a dummy volume. Here are clearly showed both healthy organs and tumor uptake, in this case meningioma visible on the head.

when superimposing PET and CT in FLUKA this difference in spatial resolution must be considered.

Lastly, as mentioned above, PET information is given in Bq/mL , that means that the total activity is divided by the considered volume. For this reason, to obtain the total number of decays in a second in a certain voxel it is necessary to multiply the value given from the PET (and hence imported into the .bnn file) for the voxel volume. On the contrary, the routine that generates particles from the activity maps reads the voxel value as a probability with no volume considered: it is thus necessary a downstream normalization.

For this purpose, I used the routine to calculate the sum of each voxel specific activity (usually of the order of $10^9 \text{ Bq}/\text{mL}$). By multiplying this number for the voxel volume ($\sim 0.024 \text{ mL}$) the total activity is obtained. This value ($\sim 10\text{MBq}$) represents the number of radioactive decays occurring in each second in the whole patient body.

Therefore, using it as number of primary particles to be generated makes the simulation compatible with an acquisition time of 1 s.

5.1.1.1 Dosimetry simulation

Among the possible applications of importing within FLUKA PET scan images, one of the most important is the evaluation of the dose given to the medical personnel during a RGS procedure.

In fact, despite the existence of wide literature about the exposition of medical staff to radioactive sources during several kind of procedures common today in nuclear medicine, there is a quiet wide variation among the estimated values. Moreover, this literature is strongly focused on low energy photons applications, such as ^{99}Tc , that, as widely discussed in this Thesis, present a deeply different behavior in term of penetration and dose release in human tissue.

Actually, there is practically no literature about the exposition of medical personnel after the patient injection of pure β^- emitters, being this kind of radiopharmaceutical used today only for radio metabolic treatments, in which the physician does not need to spend a significant time near the patient.

For these reasons, a contribution from the MC is valuable in order to give an upper limit to the radio exposition of the staff involved in the RGS technique here proposed, in particular with respect to standard γ -RGS.

To this aim, both CT and PET scans from a patient affected by hepatic Neuro Endocrine Tumor were imported into FLUKA by means of the procedure described in 5.1.1. To overcome computational problems in FLUKA, correlated with the huge number of different voxels of a whole body CT scan, the simulation was split in three, each one simulating a part of the patient body. PET and CT scans were precisely superimposed in order to avoid primary particles coming from outside the patient.

Beside the patient body, two phantoms were created to simulate the surgeon's torso and hand. In particular, the torso was modeled with a water cylinder of 30 cm diameter and 60 cm height placed at about 50 cm from the patient. The hand was modeled with a water parallelepiped ($10 \times 10 \times 2 \text{ cm}^3$) placed about 5 cm above the patient body. To simulate the presence of the glove, which plays a fundamental role in case of β^- emission, a layer of 1 mm of plastic was placed outside the hand phantom. The setup of the simulation is visible in Fig. 5.2.

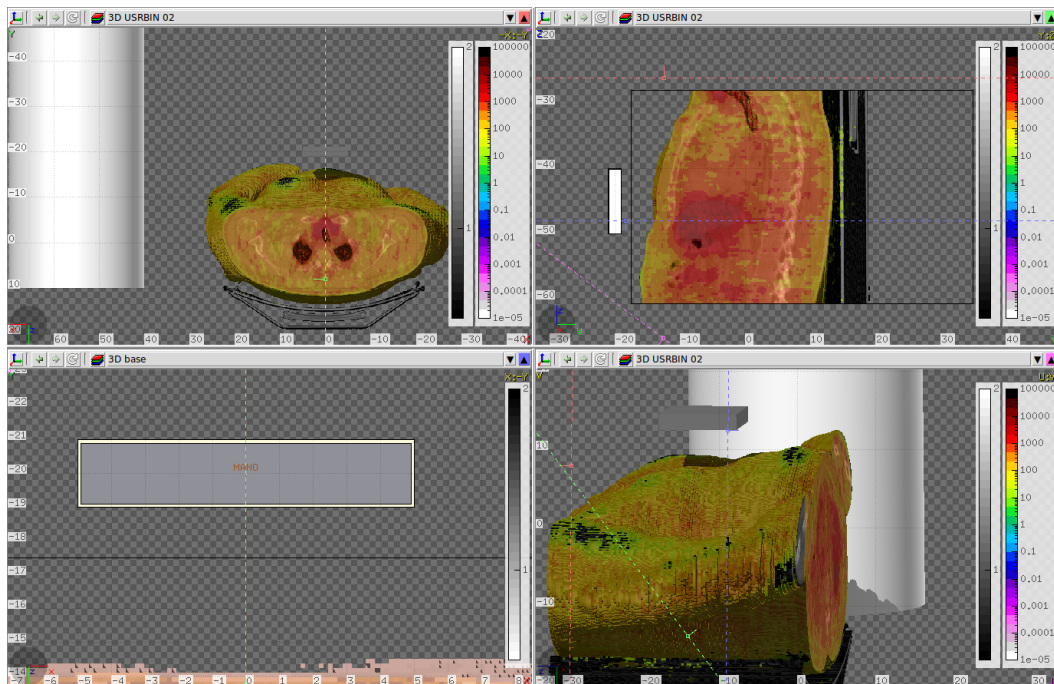


Figure 5.2. Setup of the simulation used to evaluate the radio exposition of the surgeon during a β^- -RGS procedure, as described in Sec. 5.1.1.1. Both CT and PET scans of a patient are imported; the white cylinder represents the surgeon's torso, while the parallelepiped represent his hand.

The PET data were used as an activity map for primary particles, normalizing the number of generated particles as described in Sec. 5.1.1 to simulate a 1 s exposition. Both ^{90}Y and ^{99}Tc were simulated. in order to compare these two approaches. For each configuration, the Equivalent Dose (DOSE-EQ) was scored in the torso and hand regions. The results are show in Tab. 5.1.

	^{99}Tc	^{90}Y
Hand	13.8 $\mu\text{Sv/h}$	0.35 $\mu\text{Sv/h}$
Torso	1.39 $\mu\text{Sv/h}$	0.04 $\mu\text{Sv/h}$

Table 5.1. Equivalent dose to the surgeon’s hand and torso during a β^- -RGS procedure with respect to a γ -RGS [37].

The equivalent dose given to both surgeon’s torso and hand are found to be significantly lower in the case of β^- -RGS than in γ -RGS, because of the greatly reduced range of electrons with respect to photons. Such a low value of radio exposition would result in practically no effect on the surgeon, not even from a legal point of view, avoiding the physician to be classified as radio protected worker. The thus obtained values for ^{99}Tc are in reasonable agreement with the present literature [8].

In the end, it has to be remarked that such an evaluation of the radio exposition provides an order of magnitude rather than a precise value, due to the possible variability among patient and imaging data, the distance of the surgeon and so on.

However, this values are good enough to demonstrate one of the key feature of the RGS technique proposed in this Thesis, i.e. the great reduction in the dose given to the medical personnel, that would result in a much simple procedure to be performed even from a technical and legal point of view.

5.1.2 Scoring routines

As mentioned in 2.4, FLUKA offers several estimators to evaluate certain quantities as deposited energy, energy spectrum, particle fluence and so on. However, for more advanced requirements and analysis custom user routines are more advisable.

For this reason, in my Thesis work I used a tool to convert FLUKA outputs in Root files. This is a set of Fortran routines that act on a step by step basis during the simulation, storing the information in Root files according to specifically build classes. This crossing between languages (Fortran77 and C++) is managed by means of intercommunicating functions and classes within the routines.

The thus obtained Root file consist of a TTree that allows many analysis, from energy spectrum in the detector to correlation between initial particle momentum and track length therein, and so on. The typical file structure is showed in fig 5.3.

This approach was the most used within this Thesis work. However, due to the huge amount of information stored, it implies greater simulation times, and the produced files are often quite large (of the order of several GB). Hence, other simpler scoring techniques were also used in some cases.

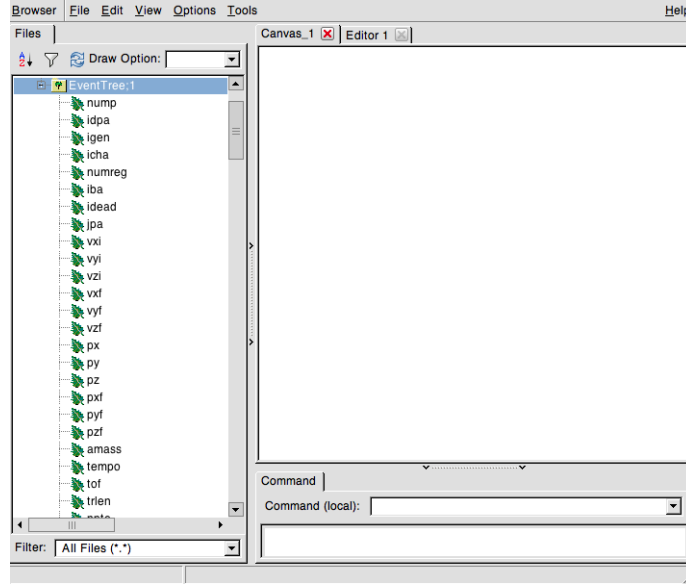


Figure 5.3. Typical structure of the file obtained via the scoring routines described in 5.1.2.

5.2 Expected signal rates in Brain Surgery applications

In Sec. 4.1.2 the applicability of β^- -RGS in the field of Brain Surgery was discussed. In particular, in Sec. 4.1.2.2 a statistic study was presented to evaluate the uptake of cerebral tumor to DOTATOC, that is the best candidate at the moment for β^- -RGS.

The DICOM files from PET scans of patients affected by either meningioma or glioma were used to calculate the Standardized Uptake Value of both Tumor and Non Tumor areas (Tab. 4.5 and 4.6).

From these values, the corresponding TNRs (Tumor Non Tumor Ratios) were extracted, and are reported again in Fig. 5.4 for convenience.

As already argued, these values are theoretically good enough to perform β^- -RGS. However, to obtain an estimate of the expected signal from the probe in the real application case a full simulation of the setup is needed.

From the obtained Standardized Uptake Values for tumor and non tumor tissue, and assuming that the radio-tracer is administered $\Delta t_{surg} = 12$ h before the intervention, it is possible to estimate the expected specific activity in tumor (μ^{ref}) and non-tumor (μ_{NT}^{ref}) at the time of the surgery for each patient:

$$\mu_{(NT)}^{ref} = SUV_{(NT)} A_{ref} e^{-0.693 \Delta t_{surg} / T_Y^{1/2}}, \quad (5.1)$$

where $T_Y^{1/2}$ is the ^{90}Y half-life and $A_{ref} = 3$ MBq/kg is a reference administered activity per unit mass, chosen as the one injected for a typical PET scan.

5.2.1 Simulation of the setup

In order to convert these data in proper signal rates, FLUKA was used to simulate the response of the probe to such activities.

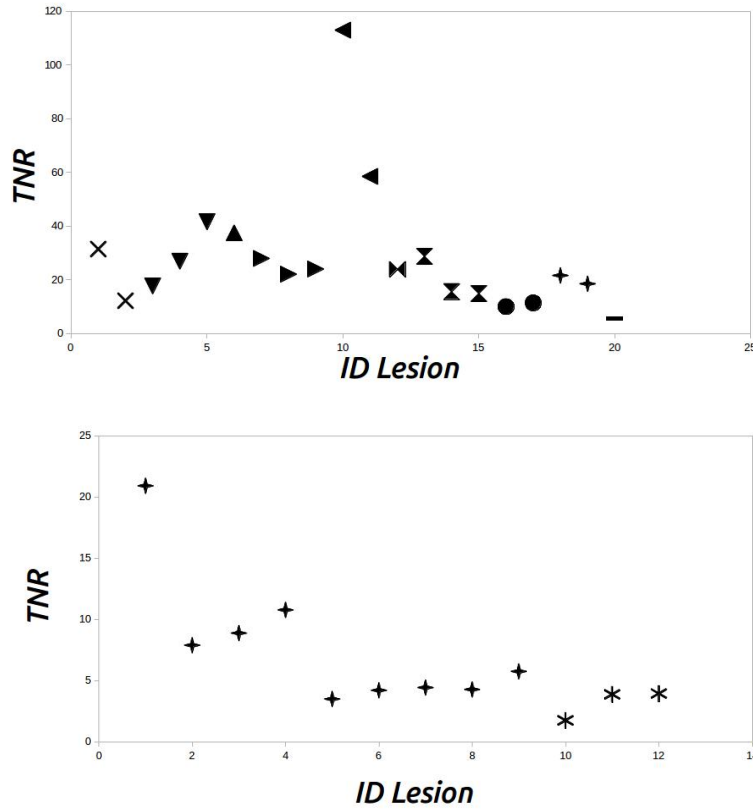


Figure 5.4. TNRs obtained for meningioma (top) and glioma (bottom) from the study presented in Sec. 4.1.2.2.

In this simulation, the background was represented by an extended region with a specific activity μ_{NT}^{ref} of ^{90}Y , while the tumor residual used as benchmark is a cylinder with a radius of 3 mm and an height of 3.5 mm for a total volume of 0.1 mL (Fig. 5.5). These are indeed the dimension of a typical residual that has to be identified by the probe. The tumor region is assumed to have a specific activity μ^{ref} of ^{90}Y .

By using the conversion factor evaluated in Sec. 3.2.2 to convert the hardware threshold use to discriminate the signals into the corresponding value in the simulation output, the signal rates $\nu_{(NT)}$ were obtained.

From the measured detector rates we can estimate the time needed by the probe to identify a tumor residual of 0.1 ml with a given probability of false positives (FP) or false negatives (FN). For a fixed acquisition time of the probe (t_{probe}) the FP and FN are defined as:

$$FP = 1 - \sum_{N=0}^{N_{thr}-1} \mathcal{P}_{\nu_{NT}t_{probe}}(N) \quad (5.2)$$

$$FN = \sum_{N=0}^{N_{thr}-1} \mathcal{P}_{\nu t_{probe}}(N). \quad (5.3)$$

where $\mathcal{P}_\mu(N)$ indicates the Poisson probability to have N if the mean is μ and N_{thr} is the threshold in counts that we expect to set on the probe signal.

The minimum time that a surgeon needs to spend on a sample to evaluate whether it is healthy or not, t_{probe}^{min} , is determined by finding the minimal value of t_{probe} for which there exists a value of N_{thr} such that $FN < 5\%$ and $FP < 1\%$.

RGS can be practical only if, when administering the reference activity (3 MBq/kg), the time t_{probe}^{min} is not significantly longer than 1 s, a reasonable time lapse in the surgical environment. Otherwise, an increase of activity would be needed. On the contrary, if t_{probe}^{min} is shorter than 1 s there are margins to reduce the administered activity. We therefore also calculated which is the minimum activity that needs to be administered (A_{min}) 12 hours before surgery in order to achieve $FN < 5\%$ and $FP < 1\%$ in $t_{probe}^{min} = 1$ s.

It is to be noted that the scaling between activities is performed neglecting the biological wash-out of the organs. Nevertheless, wash-out is faster on the healthy tissues than in the tumor, where the tracer is bound. Tumors in fact show typically a constant or increasing phase in the first day after administration and a wash-out after 24 h, as commonly reported in literature [21], and as resulted from the already discussed study carried out on Neuroendocrine Tumors (Sec. 4.2.2) as well.

Since the surgery, compared to PET scan, takes place after a longer time has elapsed, the TNR was most likely underestimated and the conclusions of this discussion are conservative.

5.2.2 Results

The results thus obtained when considering the probe prototype named *ProbeSiPm* (Sec. 3.2) are shown separately for Meningioma and Glioma in Tab. 5.2 and 5.3 respectively. The tables report for each patient and lesion the signal and NT rates expected on the probe, the time t_{probe}^{min} needed to identify a 0.1 ml residual if an activity $A_{ref} = 3$ MBq/kg is administered and the minimum activity, scaled to the time of the surgery, that needs to be administered to have $t_{probe}^{min} = 1$ s.

For *Meningiomas*, the measurements indicate that the technique would be effective also administering less than 3 MBq/kg, in a significant fraction of the cases even less than 0.5 MBq/kg.

On the other hand, as regards *Gliomas*, the obtained values shows that by administering 3 MBq/kg the probe requires about 5 – 6 s to discriminate between lesion and healthy tissue. Thus, in order to effectively apply this technique to Gliomas, that, as discussed in Sec. 4.1.1.1, could be the “killer application” of β^- -RGS, longer measurements times will be needed, since the required activities to reach the requested sensitivity in 1 s ($A(1\text{ s})$ in the table) are too large.

Moreover, it must be said that all the glioma patient considered in this study had already been treated with radio-therapy and chemo-therapy, and this can have altered the receptors, typically decreasing their expression.

In any case, it has lastly to be noted that in order to reduce the measurement time, there are still margins to improve the sensitivity of the probe: in particular, more sensitive devices can be exploited in the scintillation light collection and crystals

Patient ID	$N_{les.}$	W (kg)	A_{adm} (MBq)	ν (Hz)	ν_{NT} (Hz)	t_{probe}^{min} (s)	A_{1s}^{min} (MBq/kg)	Diagnosis	Previous Treatment
M01	1	63	220	32.2	1.9	0.2	0.7	atypical	S
M02	1	80	160	17.6	2.6	0.6	1.9	atypical	S/RT/PRRT
M03	3	95	305	33.7	3.5	0.3	0.9	likely atypical	S/RT
				50.3	3.5	0.3	0.5		
				76.8	3.5	0.1	0.3		
M04	1	48	200	89.4	4.5	0.1	0.2	atypical	S/RT/CT
M05	3	57	130	66.7	4.4	0.2	0.3	relapse	S/RT/CT/PRRT
				53.2	4.4	0.2	0.5		
				57.6	4.4	0.2	0.4		
M06	2	90	145	107.6	1.8	0.1	0.1	unknown	PRRT
				56.1	1.8	0.2	0.4		
M07	1	74	237	50.2	3.9	0.2	0.5	anaplastic	S/RT
M08	3	105	223	55.7	3.6	0.2	0.5	atypical	S/RT
				31.2	3.6	0.2	0.9		
				29.6	3.6	0.4	0.9		
M09	2	48	145	13.4	2.4	0.9	2.7	atypical	S/RT
				15.1	2.4	0.7	2.5		
M10	1	70	240	14.6	1.2	0.6	1.8	atypical	S/RT
				12.6	1.2	0.8	1.9		
M11	1	75	220	12.7	3.8	1.6	5.0	atypical	unknown

Table 5.2. Number of lesions (N_{les}), weight (W), administered activity in the PET with Ga (A_{adm}), signal and non-tumor rate expected on the probe (ν and ν_{NT} respectively), the time t_{probe}^{min} needed to identify a 0.1 ml residual and the minimum activity that needs to be administered to have $t_{probe}^{min} = 1$ s (A_{1s}^{min}), and diagnosis for the meningioma patients considered. ν , ν_{NT} , t_{probe}^{min} , and A_{1s}^{min} are computed assuming that 12 hours elapse between the administration of ^{90}Y and the surgery, while, when estimating the first three quantities, it is assumed that the reference activity $A_{ref} = 3$ MBq/kg is administered. The last column indicates whether the patient has already undergone surgery (S), radiotherapy (RT), chemotherapy (CT) or PRRT.

with a larger light yield can be considered, at the expense of a more challenging engineering of the whole apparatus.

Patient ID	W (kg)	A_{adm} (MBq)	ν (Hz)	ν_{NT} (Hz)	t_{probe}^{min} (s)	A_{1s}^{min} (MBq/kg)	Diagnosis	Previous Treatment
G01	97	246	16.5	1.4	0.5	1.5	HGG	S/RT/CT/PRRT
G02	68	223	5.2	1.1	2.6	8.5	HGG	RT/CT/B
G03	80	152	9.6	1.9	1.4	4.3	HGG	S/RT/CT
G04	93	198	22.4	3.7	0.6	1.8	HGG	S/RT/CT/PRRT
G05	90	192	4.6	2.0	7.4	23.6	HGG	S/RT/CT/PRRT
G06	60	185	4.4	1.6	5.8	20.0	HGG	S/RT/CT
G07	63	194	4.8	1.7	5.1	17.6	HGG	S/RT/CT
G08	70	266	2.1	0.8	-	40.0	HGG	RT/CT
G09	85	255	3.7	1.1	5.3	17.6	HGG	S/RT/CT
G10	80	224	2.2	1.6	-	-	oligodendroglioma	S/RT/CT/I
G11	70	234	5.1	2.0	5.5	18.8	HGG	RT/CT
G12	15	38	5.0	2.0	5.9	18.8	pontine glioma	RT/CT/PRRT

Table 5.3. Weight (W), administered activity in the PET with Ga (A_{adm}), signal and non-tumor rate expected on the probe (ν and ν_{NT} respectively), the time t_{probe}^{min} needed to identify a 0.1 ml residual and the minimum activity that needs to be administered to have $t_{probe}^{min} = 1$ s (A_{1s}^{min}), and diagnosis for the HGG patients considered. ν , ν_{NT} , t_{probe}^{min} , and A_{1s}^{min} are computed assuming that between the administration of ^{90}Y and the surgery 12 hours elapse, while, when estimating the first three quantities, it is assumed that the reference activity $A_{ref} = 3$ MBq/kg is administered. The HGG is always treated as a single lesion. The last column indicates whether the patient has already undergone surgery (S), radiotherapy (RT), chemotherapy (CT), Bevacizumab (B), Immunotherapy (I) or PRRT.

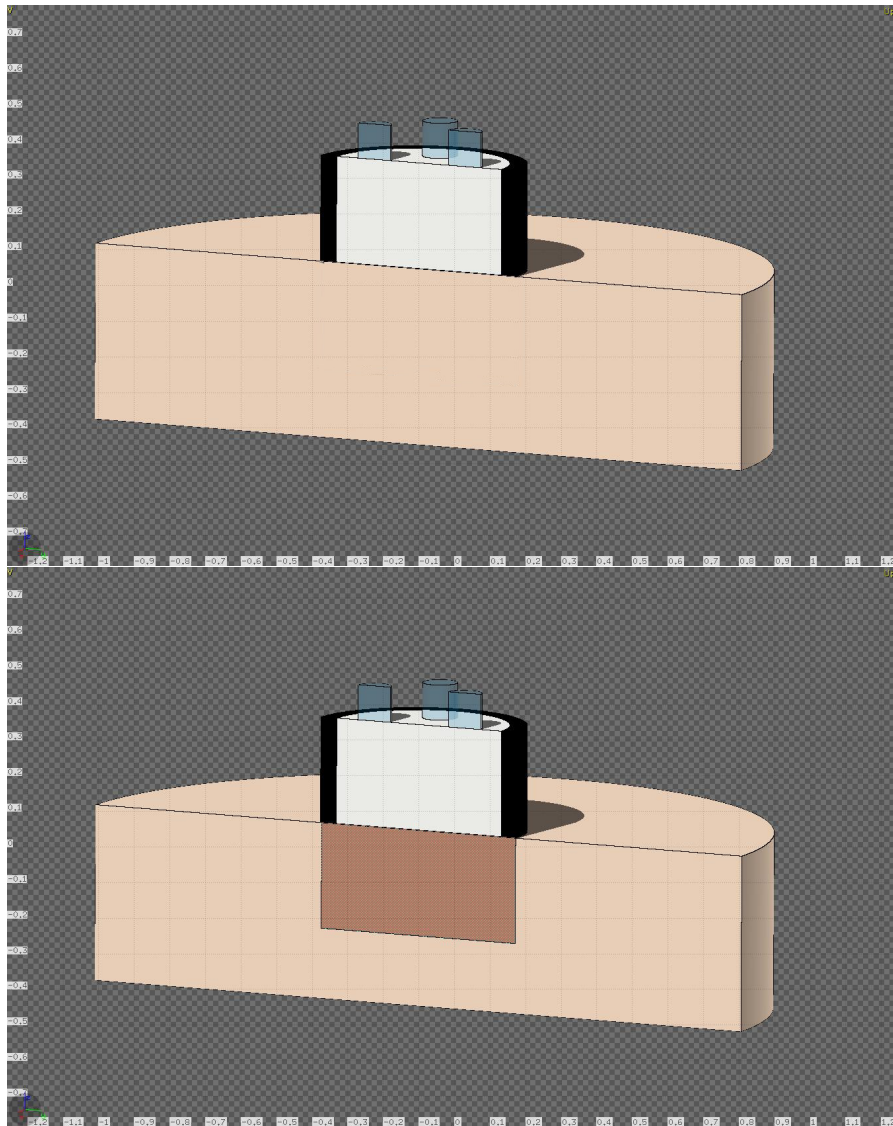


Figure 5.5. Representation of background (top) and residual (bottom) volumes to which the probe was exposed in the FLUKA simulation used to convert the specific activity obtained by the statistic study carried out on cerebral tumors (Sec. 4.1.2.2) into proper signal rate, as explained in the text.

Conclusions

In this Thesis I discussed a novel approach to Radio Guided Surgery, exploiting the characteristics of the β^- emission in place of β^+ or γ , that are the ones currently used. This technique is aimed at giving the surgeon a tool to reach a more accurate and complete resection of the tumoral mass, resulting in a better outcome for the patients. The novel approach here discussed showed good capabilities to overcome the limitations shown by current techniques.

Regarding the molecule to use as radiopharmaceutical, ^{90}Y -DOTATOC was chosen as first candidate, from a tradeoff between the ideal characteristics such a molecule should have and the availability and diffusion of this particular compound.

As far as the choice of the active material to use for the detector of the β^- emission is concerned, *para-terphenyl* was chosen after a complete characterization of its properties, mainly due to its large light production (of the order of few tens of photoelectrons per MeV), that allows for the detection of even small signals, and its low Z , that results in poor sensitivity to photon contamination.

I described the first prototypes of the probe, together with their optimization in term of detector size, shielding and electronic readout, carried out exploiting both laboratory measurements and Monte Carlo simulations performed with the FLUKA code.

The possible medical applications of β^- -RGS were then discussed, focusing in particular on brain and Neuroendocrine tumors surgery. Two devoted statistical studies on data from patients affected by these kind of cancers were presented, indicating that both in case of cerebral (*meningioma* and *glioma*) and Neuroendocrine tumors there is room for an effective application of this technique.

In particular, Meningioma are likely to be the first field of test, due to the high receptivity to DOTATOC resulting in a high TNR (*Tumor Non Tumor Ratio*, always greater than 10), and thus in a low activity needed to be injected into the patient. The application to gliomas however would require higher operational times due to the weaker signal (TNR of about 8), and would profit of an higher activity administered, or a higher sensitivity probe.

Neuroendocrine tumors have turned out to be good candidates for β^- -RGS too, in particular if an optimal amount of time, estimated to be ~ 20 h, elapses between the injection of the radiopharmaceutical and the surgery.

Moreover, I presented a development in the FLUKA Monte Carlo code allowing to import within the simulation DICOM data from Positron Emission Tomography scans, in order to use it as activity distribution of the decaying isotope, thus realistically reconstructing the operation field. Using this tool, I evaluated the radio exposition of the surgeon performing a RGS procedure, finding it to be orders of magnitude lower in the case of β^- -RGS than in case of γ -RGS. The ability to import

PET scans within FLUKA will be a valuable tool in the future for the evaluation of the performances of the probe in any real clinical application scenario.

Ringraziamenti

Non so bene perchè, ma ho sempre pensato che sarei finito a scrivere questa tesi un po' come aveva fatto Marge Simpson con il suo romanzo, e cioè iniziando dai ringraziamenti! E invece per farlo ho atteso fino all'ultimo, fino ad un passo dal traguardo. Forse perchè davvero vista da qua la strada fatta sembra finalmente tanta, e la fatica di condensare in una pagina chi mi ha aiutato a farla sembra improba.

Ma siccome so di numerosissime persone che attendono con ansia questi miei ringraziamenti, e che non mi perdonerebbero mai una tale mancanza, vedrò di fare del mio meglio (certo, potrei anche pensare di farne una versione *fake* appositamente per Martina...)!

Se è vero che il dottorato rappresenta l'“ultimo grado” della formazione universitaria, allora quella di oggi è l'ultima tappa di un viaggio partito oramai molti anni fa.

Ringrazio innanzitutto il Prof. Faccini, per avermi oramai da tempo immemore adottato didatticamente e scientificamente come $n+1$ -esimo figlio (con n che va da 1 a 3). Ricordo ancora una delle mie primissime visite al suo ufficio, quando esclamai di sorpresa al vedere che premendo la freccia in su nel prompt lui teneva in memoria i comandi dati in precedenza.. mi chiedo spesso come abbia fatto a non cacciarmi seduta stante dalla sua vita accademica!

Qualche giorno fa invece, sicuramente in preda ad allucinazioni da post-lezione, l'ho sentito chiaramente dire a proposito di un mio programma: “no, è più elegante come lo hai scritto tu di come l'ho scritto io”..

Tornando seri, mi chiedo spesso cosa sarebbe stato della mia vita scientifica (e non solo) se in un giorno qualunque Zio Cino non mi avesse indirizzato a lui (che io non avevo mai incontrato come docente) per ragionare di dissertazione.. Poco importa infondo, perchè non posso che essere grato e felice che fra tutte le infinite traiettorie il pallinometro abbia scelto questa.

Ringrazio poi il Prof. Patera, Alessio e tutta la truppa di SBAI(M), che da Catania in giù mi hanno insegnato che chi pensa che la fisica sia da tristi noiosi e sfigati allora forse è il caso che cambi esperimento.

Ringrazio di cuore Silvio (con Elena e Andrea, quasi un trio da format televisivo!), perchè mi ha insegnato che la fisica in realtà è molto più simile al garage di casa mia di quanto immaginassi, e che se vuoi salvare il mondo aiutando i super mega chirurghi col SUV e l'*erre* moscia devi partire dal tornio e dallo scotch.

Ringrazio la baita. Sì, proprio intesa come capanno pseudo-aubisivo in eternità d'annata. Perché se è vero che esistono luoghi "oggettivamente belli", ne esistono altrettanti "soggettivamente stupendi". A quelle quattro pareti di dubbio gusto e salubrità resterà per sempre il merito di essere stata la tana, l'appiglio, il *centro di massa* delle vite di tanti di noi. Un "porto di mare", davvero, ma nel senso più bello che c'è, del luogo che comunque sa trovarti un posto, fra una scimmietta camerunense, un Dio egizio e una bottiglia di aceto balsamico. Come non pensare ora a tutte le domande (di fisica, politica, economia, grammatica) fatte "al vento" e puntualmente risposte da qualcuno?

Ringrazio allora Filippo, per essere stato il *mio imperatore*, ed avermi ricordato proprio all'ultimo che "segui sempre i tuoi sogni" forse va bene per la vita nei film, mentre quella vera ti chiama ogni giorno a saperli mediare, anzi direi coinvolgere (tramite diabolici integrali tra l'altro) con quello che ti accade ogni giorno e con le strade che ti si distendono d'avanti.

Ringrazio Laura, perché è sempre stata e sempre sarà la mia "massima esperta mondiale" di un sacco di cose.

Ringrazio Marco, per essere un fratello-FLUKISTA e per averci trasmesso la sana usanza della birretta al Luppolo come punto nodale delle nostre vite.

Ringrazio Nicola, perché fra grosse divergenze (politiche) e passionali amori (informatici) comuni e con il suo diventare intercalare oramai quotidiano per tutti noi (Nicò!) è diventato in certo modo la spina dorsale della baita stessa.

Ringrazio Pablo (o Pedro che dir si voglia), perché raramente mi è capitato di innamorarmi così follemente e in così poco tempo di qualcuno!

Ringrazio Gabriele, vero e sincero compagno di viaggio in questi tre anni, dalla mensa, al "momento link stupidi su FB post pranzo", alle discussioni sui dinosauri e gli squali, ai viaggi in scooter sulla Colombo, alle nostre lunghe passeggiate felici e ridenti per le vie di Balduina (senza mai invitare Martina ovviamente!), alle crostate, alla pizza.. Dio, che voglia di pizza ora... no davvero, andiamo a prendere la pizza!? Ringrazio Emanuele, perché nonostante l'impegnativa rate di "spotto!?", "Nigò" e "me so innamorato", incredibilmente quando non c'è lascia un senso di vuoto incolmabile.

Ringrazio Ilaria, perché i primi compagni di viaggio non ti lasciano mai, anche se e li vedi un po' meno. Ogni volta che passo da Viale dell'università ripenso a quella volta agli albori di un gennaio di mille anni fa, dopo il primo proto-meeting explorer, che lo abbiamo percorso insieme scambiandoci dubbi ed entusiasmi su quello strano gruppo di persone...

Ringrazio Martina, perché fra tutti gli universi possibili e i modi in cui come quasi "conterranei" avremmo potuto conoscerci (che ne so, io Ingegnere in Ancona e te ragazza alla pari di Zia Ginetta!?) alla fine l'universo ne ha scelto uno decisamente originale, scoppiettante, bello.

Che dire.. anche se fa male, "forse era giusto così"... che "la Baita" così come l'abbiamo conosciuta finisse con noi. Dopo averci accolti, cresciuti e coccolati, ora ci lancia un po' in giro per il mondo. Io, però, non ho alcun dubbio che in tutti noi tutto quello che è stato resterà per sempre chiaro e visibile.

Per dire.. credete davvero di riuscire tanto facilmente a smettere di dire "proporere" o "Nigò"!?

Ringrazio poi la mia famiglia, che nella fatica di seguire i miei studi fra corsi dai nomi strambi e argomenti “lontani” (e sì che ho fatto di tutto per non allontanarmi troppo dalla medicina manco io!!) non ha mai smesso di essere con costanza e discrezione al mio fianco.

Non posso però proprio non finire ringraziando la persona che da più tempo mi accompagna in questo viaggio. Forse da quel giorno in cui da liceali prendemmo il treno e ci tuffammo in una Roma sconosciuta sotto un diluvio epico per le vie della Sapienza con un senso di infinita piccolezza di fronte ad un mondo così nuovo.

O forse da prima.

Perchè se devo cercare un inizio a questa mia avventura nella fisica, beh, non posso che individuarlo in quei *4 e mezzo* ripetuti sui compiti sui vettori al primo anno di liceo, nella mia disperazione più totale, nel mio brancolare nel buio.

Fino all’arrivo di una luce, una luce che di ripetuti prendeva i 10. Gli sms di incoraggiamento pre interrogazioni, i pomeriggi in gruppo a fare esercizi sul piano inclinato (che ovviamente erano in buona parte anche una scusa!), poi sull’elettromagnetismo, la gravitazione e gli anni che passano.

L’immensa soddisfazione quella volta che in un diabolico compito sulla relatività io presi il doppio di lei! (io 4, lei 2).

L’epico risultato delle olimpiadi di fisica all’ultimo anno di liceo, ricordo il foglio come fosse ieri: Primo classificato: Roberta Gagliardini, punti 58.5; secondo classificato: Francesco Collamati, punti 58.0.

Avrei tante di quelle cose da scrivere su questi nostri anni romani, che hanno preso quei due ragazzini spauriti e ci hanno portato fin qui, ma poi sti ringraziamenti mi vengono più lunghi del capitolo finale, e non mi sembra il caso!

.. e poi, tanto, avremo tutta la vita per ricordarli insieme..

Bibliography

- [1] D. Orringer, D. Lau, S. Khatri, G. J. Zamora-Berridi, K. Zhang, C. Wu, N. Chaudhary, and O. Sagher, “Extent of resection in patients with glioblastoma: limiting factors, perception of resectability, and effect on survival,” *Journal of Neurosurgery*, vol. 117, no. 5, pp. 851–859, 2012, <http://dx.doi.org/10.3171/2012.8.JNS12234>. PMID: 22978537.
- [2] M. Lacroix, D. Abi-Said, D. R. Fourney, Z. L. Gokaslan, W. Shi, F. De-Monte, F. F. Lang, I. E. McCutcheon, S. J. Hassenbusch, E. Holland, K. Hess, C. Michael, D. Miller, and R. Sawaya, “A multivariate analysis of 416 patients with glioblastoma multiforme: prognosis, extent of resection, and survival,” *Journal of Neurosurgery*, vol. 95, no. 2, pp. 190–198, 2001, <http://dx.doi.org/10.3171/jns.2001.95.2.0190>. PMID: 11780887.
- [3] P. Black, “Management of malignant glioma: role of surgery in relation to multimodality therapy,” *Journal of Neurovirology*, pp. 227–236, 1998.
- [4] N. L. Dorward, O. Alberti, B. Velani, F. A. Gerritsen, W. F. J. Harkness, N. D. Kitchen, and D. G. T. Thomas, “Postimaging brain distortion: magnitude, correlates, and impact on neuronavigation,” *Journal of Neurosurgery*, vol. 88, no. 4, pp. 656–662, 1998, <http://dx.doi.org/10.3171/jns.1998.88.4.0656>. PMID: 9525711.
- [5] e. A. Chicoine MR, Lim CC, “Implementation and preliminary clinical experience with the use of ceiling mounted mobile high field intraoperative magnetic resonance imaging between two operating rooms.,” *Acta Neurochir Suppl.*, pp. 109:97–102, 2011.
- [6] G. M. van Dam, G. Themelis, L. M. A. Crane, N. J. Harlaar, R. G. Pleijhuis, W. Kelder, A. Sarantopoulos, J. S. de Jong, H. J. G. Arts, A. G. J. van der Zee, J. Bart, P. S. Low, and V. Ntziachristos, “Intraoperative tumor-specific fluorescence imaging in ovarian cancer by folate receptor-[alpha] targeting: first in-human results,” *Nat Med*, vol. 17, pp. 1315–1319, Oct. 2011.
- [7] G. Widhalm, “Intra-operative visualization of brain tumors with 5-aminolevulinic acid-induced fluorescence.,” *Clinical neuropathology*, vol. 33, no. 4, pp. 260–278, 2013.
- [8] S. Mariani, Giuliano, *Radioguided Surgery, a Comprehensive Team Approach*. Springer Science and Business Media :, 2010.

- [9] S. van Esser, M. Hobbelenk, P. Peeters, E. Buskens, I. van der Ploeg, W. Mali, I. Rinkes, and R. van Hillegersberg, "The efficacy of 'radio guided occult lesion localization' (roll) versus 'wire-guided localization' (wgl) in breast conserving surgery for non-palpable breast cancer: A randomized clinical trial - roll study," *BMC Surgery*, vol. 8, no. 1, p. 9, 2008.
- [10] Z. S. Paganelli G, Luini A, "Radioguided surgery of occult breast lesions," *Eur J Cancer*, no. 34, pp. 204–205, 1998.
- [11] A. G. a. V. Bitencourt, E. N. P. Lima, P. N. V. Pinto, E. B. L. Martins, and R. Chojniak, "New applications of radioguided surgery in oncology," *Clinics*, vol. 64, pp. 397–402, May 2009.
- [12] S. Adams, R. P. Baum, a. Hertel, H. J. Wenisch, E. Staib-Sebler, G. Herrmann, a. Encke, and G. Hör, "Intraoperative gamma probe detection of neuroendocrine tumors.," *Journal of nuclear medicine : official publication, Society of Nuclear Medicine*, vol. 39, pp. 1155–60, July 1998.
- [13] H. Chen, E. Mack, and J. R. Starling, "Radioguided parathyroidectomy is equally effective for both adenomatous and hyperplastic glands.," *Annals of surgery*, vol. 238, pp. 332–7; discussion 337–8, Sept. 2003.
- [14] R. K. Halkar and J. N. Aarsvold, "Intraoperative probes.," *Journal of nuclear medicine technology*, vol. 27, pp. 188–93; quiz 195–6, Sept. 1999.
- [15] F. D. et al., "Intraoperative beta probe: a device for detecting tissue labeled with positron or electron emitting isotopes during surgery," *Med. Phys.*, no. 21, pp. 153–157, 1994.
- [16] S. Yamamoto, K. Matsumoto, S. Sakamoto, K. Tarutani, K. Minato, and M. Senda, "An intra-operative positron probe with background rejection capability for fdg-guided surgery," *Annals of nuclear medicine*, vol. 19, no. 1, pp. 23–28, 2005.
- [17] S. Bonzom, L. Ménard, S. Pitre, M. A. Duval, R. Siebert, S. Palfi, L. Pinot, F. Lefebvre, and Y. Charon, "An Intraoperative Beta Probe Dedicated to Glioma Surgery : Design and Feasibility Study," *IEEE Transactions on Nuclear Science*, vol. 54, no. 30, pp. 30–41, 2007.
- [18] F. Bogalhas, Y. Charon, M.-a. Duval, F. Lefebvre, S. Palfi, L. Pinot, R. Siebert, and L. Ménard, "Development of a positron probe for localization and excision of brain tumours during surgery.," *Physics in medicine and biology*, vol. 54, pp. 4439–53, July 2009.
- [19] R. Selverstone B, SweetWH, "Theclinical useof radioactive phosphorus in the surgeryof brain tumors," *Ann. Surg.*, no. 130, pp. 643–651, 1949.
- [20] V. Ambrosini, M. Fani, S. Fanti, F. Forrer, and H. R. Maecke, "Radiopeptide imaging and therapy in Europe.," *Journal of nuclear medicine : official publication, Society of Nuclear Medicine*, vol. 52 Suppl 2, pp. 42S–55S, Dec. 2011.

- [21] M. Cremonesi, M. Ferrari, S. Zoboli, M. Chinol, M. G. Stabin, F. Orsi, H. R. Maecke, E. Jermann, C. Robertson, M. Fiorenza, G. Tosi, and G. Paganelli, "Biokinetics and dosimetry in patients administered with (111)in-dota-tyr(3)-octreotide: implications for internal radiotherapy with (90)y-dotatoc.," *European Journal of nuclear medicine*, vol. 26, no. 8, 1999.
- [22] *The beginning of the Monte Carlo method*. Los Alamos: Los Alamos Science, Special Issue, 1987.
- [23] G. B. et al., "The fluka code: Description and benchmarking," *Proceedings of the Hadronic Shower Simulation Workshop 2006, Fermilab 6–8 September 2006*, pp. 31–49, 2007.
- [24] V. Vlachoudis, *FLAIR: A Powerful But User Friendly Graphical Interface For FLUKA*. Saratoga Springs, New York: Proc. Int. Conf. on Mathematics, Computational Methods and Reactor Physics, 2009.
- [25] D. Y. e. a. Akimov, *Development of VUV wavelength shifter for the use with a visible light photodetector in noble gas filled detectors.*, vol. 695. 2012.
- [26] D. Y. e. a. Akimov, *Detection of scintillation light in liquid xenon by multipixel avalanche Geiger photodiode and wavelength shifter.*, vol. 5. 2010.
- [27] M. Angelone, G. Battistoni, F. Bellini, V. Bocci, F. Collamati, E. D. Lucia, R. Faccini, F. Ferroni, S. Fiore, M. Marafini, D. Materazzo, I. Mattei, S. Morganti, V. Patera, L. Piersanti, M. Pillon, L. Recchia, A. Russomando, A. Sarti, A. Sciubba, E. S. Camillocci, and C. Voena, "Properties of para -terphenyl as a detector for α , β and γ radiation .,"
- [28] K. Amako *et al.*, "Comparison of the Geant4 electromagnetic physics models against the NIST reference data," *IEEE T. Nucl. Sci.*, vol. 52, p. 910, 2005.
- [29] J. Birks, *The Theory and Practice of Scintillation Counting*. Oxford: Pergamon Press, 1964.
- [30] K. Amako *et al.*, "Comparison of the Geant4 electromagnetic physics models against the NIST reference data," *IEEE T. Nucl. Sci.*, vol. 52, p. 910, 2005.
- [31] J. H. Lee, *Meningiomas: Diagnosis, Treatment, and Outcome*. Springer Science and Business Media :, 2011.
- [32] G. Wrobel, P. Roerig, F. Kokocinski, K. Neben, M. Hahn, G. Reifenberger, and P. Lichter, "Microarray-based gene expression profiling of benign, atypical and anaplastic meningiomas identifies novel genes associated with meningioma progression," *International Journal of Cancer*, vol. 114, no. 2, pp. 249–256, 2005.
- [33] V. K. K. V. K. P. Sakellariou, "Surgical outcome of treating grades ii and iii meningiomas: A report of 32 cases," *Neuroscience Journal*, vol. 2013, pp. 249–256, 2013.

- [34] L. S. Chin, B. E. Lazio, T. Biggins, and P. Amin, "Acute complications following gamma knife radiosurgery are rare," *Surgical Neurology*, vol. 53, no. 5, pp. 498–502, 2000.
- [35] S. L. Stafford, B. E. Pollock, R. L. Foote, M. J. Link, D. A. Gorman, P. J. Schomberg, and J. A. Leavitt, "Meningioma radiosurgery: Tumor control, outcomes, and complications among 190 consecutive patients," *Neurosurgery*, vol. 49, no. 5, p. 1029, 2001.
- [36] J. Reubi and Al, "High incidence of somatostatin receptors in human meningiomas: Biochemical characterization," *The Journal of Clinical Endocrinology and Metabolism*, vol. 63, no. 2, pp. 433–438, 1986. PMID: 3013920.
- [37] F. Collamati, A. Pepe, F. Bellini, V. Bocci, M. Cre, E. D. Lucia, P. M. Frallicciardi, C. M. Grana, M. Marafini, A. Russomando, A. Sarti, A. Sciubba, M. Senzacqua, E. S. Camillocci, C. Voena, R. Faccini, D. Fisica, S. Universita, I. Sezione, and L. Nazionali, "Towards a radio-guided surgery with beta- decays: Uptake of a somatostatin analogue (dotatoc) in meningioma and high grade glioma.," vol. 0, no. 0, pp. 1–17, 2014.
- [38] A. Loening, "Amide: A medical image data analysis tool," vol. v 1.0.4, 2000–2012.
- [39] K. Hemminki and X. Li, "Incidence trends and risk factors of carcinoid tumors," *Cancer*, vol. 92, no. 8, pp. 2204–2210, 2001.
- [40] I. M. Modlin, K. D. Lye, and M. Kidd, "A 5-decade analysis of 13,715 carcinoid tumors," *Cancer*, vol. 97, no. 4, pp. 934–959, 2003.
- [41] J. C. Yao, M. Hassan, A. Phan, C. Dagohey, C. Leary, J. E. Mares, E. K. Abdalla, J. B. Fleming, J.-N. Vauthey, A. Rashid, and D. B. Evans, "One hundred years after "carcinoid": Epidemiology of and prognostic factors for neuroendocrine tumors in 35,825 cases in the united states," *Journal of Clinical Oncology*, vol. 26, no. 18, pp. 3063–3072, 2008, <http://jco.ascopubs.org/content/26/18/3063.full.pdf+html>.
- [42] B. Eriksson, B. Annibale, E. Bajetta, E. Mitry, M. Pavel, M. Platania, R. Salazar, and U. Ploekinger, "Enets consensus guidelines for the standards of care in neuroendocrine tumors : Chemotherapy in patients with neuroendocrine tumors," *Neuroendocrinology*, vol. 90, no. 2, pp. 214–219, 2009.
- [43] S. M. Bison, M. W. Konijnenberg, M. Melis, S. E. Pool, M. R. Bernsen, J. J. M. Teunissen, D. J. Kwekkeboom, and M. de Jong, "Peptide receptor radionuclide therapy using radiolabeled somatostatin analogs: focus on future developments.," *Clinical and translational imaging : reviews in nuclear medicine and molecular imaging*, vol. 2, pp. 55–66, Jan. 2014.
- [44] F. Guerriero, M. E. Ferrari, F. Botta, F. Fioroni, E. Grassi, a. Versari, a. Sarnelli, M. Pacilio, E. Amato, L. Strigari, L. Bodei, G. Paganelli, M. Iori, G. Pedroli, and M. Cremonesi, "Kidney dosimetry in ^{177}Lu and ^{90}Y peptide receptor radionuclide therapy: influence of image timing, time-activity integration method,

and risk factors,” *BioMed research international*, vol. 2013, p. 935351, Jan. 2013.

- [45] S. Walrand, F.-X. Hanin, S. Pauwels, and F. Jamar, “Tumour control probability derived from dose distribution in homogeneous and heterogeneous models: assuming similar pharmacokinetics, ^{125}I is superior to ^{90}Y and ^{177}Lu in peptide receptor radiotherapy,” *Physics in Medicine and Biology*, vol. 57, no. 13, p. 4263, 2012.